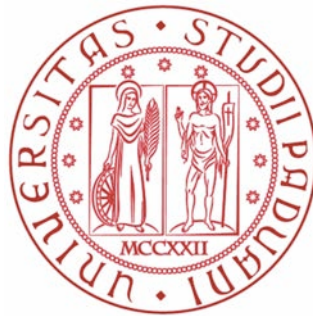

UNIVERSITY OF PADUA

Degree course in
ICT for Internet and Multimedia

Irradiation of thin film materials
for space applications
Modelling and Experimental



Supervisor:
Prof.ssa *Maria Guglielmina
Pelizzo*

Co-supervisor:
Prof. *Alain Jody Corso*

Candidate:
Giovanni Luca Santi

8 July 2019

COLOPHON

This document was typeset using the typographical look-and-feel `classicthesis` developed by André Miede. The style was inspired by Robert Bringhurst's seminal book on typography "*The Elements of Typographic Style*". `classicthesis` is available for both \LaTeX and \LyX :

<https://bitbucket.org/amiede/classicthesis/>

*A Nico e Rosetta,
a Luciana e Mario,
alla mia cara Alessia*

ABSTRACT

Optical coated elements are mainly optimized for their optical characteristics, such as transparency or reflectivity in a desired spectral region. However, for the space missions of the very next future, it will be fundamental to ensure the sustainability of these optical elements at the harsh conditions of the relevant space environment, preventing the occurrence of any critical optical degradation of their performance.

We present a study on optical coating degradation according to the ESA project *Radiation testing of optical coating in space*, lead by the National Research Council of Italy, Institute for Photonics and Nanotechnology. A mathematical model is developed to predict the coatings behaviour prior and after irradiation of different particles. A large number of samples including single and bi-layers are optically characterized in transmittance or (absolute) reflectance with a double grating spectrometer Cary 5000 and a Cary 630 FTIR spectrometer.

ACKNOWLEDGMENTS

Un sentito ringraziamento a tutti coloro che in questi anni mi sono stati vicini, aiutandomi ed incoraggiandomi in questo percorso di studi. Un Grazie particolare alla mia famiglia, che non ha mai smesso di sostenermi anche nei momenti piú critici.

Un grazie alla Prof.sa Maria Guglielmina Pelizzo per il sostegno e gli utili consigli ottenuti durante il periodo di tesi presso il laboratorio LUXOR di Padova. A tal proposito, sottolineo l'aiuto offertomi dal mio co-relatore, il Prof. Alain J. Corso, e dal mio collega di laboratorio nonché ricercatore CNR Enrico Tessarolo, il cui appoggio é stato determinante nel riuscire ad conseguire i risultati ottenuti. Un grazie anche ad Alessia, la mia dolce metà, senza la quale non sarei mai diventato la persona che sono ora.

Infine, un Grazie sincero a tutti i miei amici, a partire dai mitici *riccardí*, sperando che possano trattenersi quando dovró affrontare per la seconda volta la pena padovana comunemente nota come *papiro*.

Padova, luglio 2019

Santi Giovanni Luca

CONTENTS

1	INTRODUCTION	1
	The Electromagnetic Model	3
2	THE ELECTROMAGNETIC MODEL	5
2.1	Maxwell's equations	5
2.2	Constitutive relations	7
2.3	Boundary conditions	9
2.4	Helmholtz equation	11
2.5	Plane wave solution	12
2.6	Polarization	14
2.6.1	Linear polarization	15
2.6.2	Circular polarization	15
2.6.3	Elliptical polarization	16
2.7	The Poynting vector	17
	Optical Thin Films Theory	19
3	OPTICAL THIN FILMS THEORY	21
3.1	The simple boundary: lossless case	21
3.1.1	s-polarized incident wave	22
3.1.2	p-polarized incident wave	24
3.1.3	The tilted optical admittance	26
3.2	The simple boundary: lossy case	27
3.2.1	p-polarized light	29
3.2.2	s-polarized light	29
3.3	Thin film on a substrate	30
3.4	Assembly of thin films on a substrate	32
3.5	Reflectance, transmittance and absorbance	34
3.6	Potential Transmittance	36
	Modelling	39
4	MODELLING	41
4.1	Damage Model	42
4.1.1	Example 1: No degradation	42
4.1.2	Example 2: Drop in efficiency	42
4.1.3	Example 3: Delamination	43
4.2	Predictive Model	44
4.2.1	Optical properties of materials	45
4.2.2	Matrix model for R and T calculation	45
4.2.3	Implanted particles profile	46
4.2.4	Matrix model modification for R and T calculation (irradiated coating)	47
4.3	Software Architecture	48
4.3.1	Class objects description	48

4.4	Software User Manual	51
	Experimental	55
5	EXPERIMENTAL	57
5.1	Spectrometers	57
5.1.1	Cary 5000	57
5.1.2	Cary 630 FTIR	60
5.2	Optical Coatings	61
5.3	Samples Characterization	62
5.4	Simulation and Fitting	78
6	CONCLUSIONS	87
	Appendix	89
A	GENERAL PLANE WAVE SOLUTION	91

LIST OF FIGURES

Figure 1	Closed surface S for equation (32).	9
Figure 2	Closed contour C for equation (2).	10
Figure 3	Propagation of an electromagnetic wave	13
Figure 4	RHCP (left) and LHCP (right) plane wave propagation.	16
Figure 5	Reflection and Transmission at an interface for an impinging s-polarized plane wave.	22
Figure 6	Reflection and Transmission at an interface for an impinging p-polarized plane wave.	25
Figure 7	Wavevector decomposition at an interface for an impinging plane wave.	27
Figure 8	Thin film on a substrate.	31
Figure 9	1 keV (left) and 40 keV (right) protons distribution inside 300 nm gold layer	42
Figure 10	No degradation (left) and drop in efficiency (right) examples [12].	43
Figure 11	Degradation example. Irradiation with 50 keV He+ on Al/SiO ₂ (Optical Microscope image, top) and with 1 keV protons on Mo/Si (Transmission Electron Microscope image, bottom). The images to the right shows the effects observed after irradiation.	44
Figure 12	Logical workflow of the Predictive Model.	45
Figure 13	Distribution of He+ ions implanted in gold (density of 19.3 [g/cm ³]) as simulated by TRIM [12].	47
Figure 14	Sketch of the irradiated films area discretized in layers with the superimposition of the fractional volume distributions adopted for the reflectance computation [12].	48
Figure 15	Predictive Model Software Architecture.	49
Figure 16	Predictive Model Software App.	51
Figure 17	Cary 5000 spectrometer.	58
Figure 18	Schematic representation of Cary 5000 spectrometer.	58
Figure 19	The VW SRA by agilent (left) and a schematic representation of a (blazed) diffraction grating used in reflection.	59
Figure 20	Cary 630 FTIR spectrometer.	60
Figure 21	Schematic representation of a FTIR spectrometer.	60
Figure 22	Reflectance of S1W Au samples.	62
Figure 23	Reflectance of S1W Au samples.	62

Figure 24	Reflectance of S1G Au samples.	63
Figure 25	Reflectance of S1G Au samples.	63
Figure 26	Reflectance of S2W Al samples.	64
Figure 27	Reflectance of S2G Al samples.	64
Figure 28	Transmittance of S3GUV SiO ₂ samples.	65
Figure 29	Different types of S3GUV SiO ₂ samples response.	65
Figure 30	Reflectance of S3W SiO ₂ samples.	66
Figure 31	Transmittance of S4G TiO ₂ samples.	67
Figure 32	Reflectance of S4W TiO ₂ samples.	67
Figure 33	Transmittance of S5G ZrO ₂ samples.	68
Figure 34	Reflectance of S5W ZrO ₂ samples.	68
Figure 35	Reflectance of S6W Al/SiO ₂ samples.	69
Figure 36	Reflectance of S7W Ag/SiO ₂ samples.	69
Figure 37	Transmittance of S8G SiO ₂ /TiO ₂ samples.	70
Figure 38	Reflectance of S8W SiO ₂ /TiO ₂ samples.	70
Figure 39	Transmittance of S9G SiO ₂ /ZrO ₂ samples.	71
Figure 40	Reflectance of S9W SiO ₂ /ZrO ₂ samples.	71
Figure 41	Reflectance of S10G Au/MgF ₂ samples.	72
Figure 42	Reflectance of S10G Au/MgF ₂ samples.	72
Figure 43	Reflectance of S10W Au/MgF ₂ samples.	73
Figure 44	Reflectance of S10W Au/MgF ₂ samples.	73
Figure 45	Reflectance of S11W Pt samples.	74
Figure 46	Reflectance of W samples.	74
Figure 47	Transmittance of G samples.	75
Figure 48	Transmittance of GUV samples.	75
Figure 49	Different types of GUV samples response.	76
Figure 50	Transmittance of G1 samples.	76
Figure 51	Transmittance of G2 samples.	77
Figure 52	Transmittance of G3 samples.	77
Figure 53	Simulation with nominal thickness (blue curve) and measured reflectance (red curve) of S1W Au samples.	79
Figure 54	Simulation with nominal thickness (blue curve) and measured reflectance (red curve) of S1G Au samples.	79
Figure 55	Simulation with nominal thickness (blue curve) and measured reflectance (red curve) of S2W Al samples.	80
Figure 56	Simulation with nominal thickness (blue curve) and measured reflectance (red curve) of S2G Al samples.	80
Figure 57	Simulation with nominal thickness (blue curve), estimated thickness (green curve) and measured reflectance (red curve) of S3GUV SiO ₂ samples.	81

Figure 58	Simulation with nominal thickness (blue curve), estimated thickness (green curve) and measured reflectance (red curve) of S4G TiO ₂ samples. . .	81
Figure 59	Simulation with nominal thickness (blue curve), estimated thickness (green curve) and measured reflectance (red curve) of S5G ZrO ₂ samples. . .	82
Figure 60	Simulation with nominal thickness (blue curve), estimated thickness (green curve) and measured reflectance (red curve) of S6W Al/SiO ₂ samples. . .	82
Figure 61	Simulation with nominal thickness (blue curve) and measured reflectance (red curve) of S7W Ag/SiO ₂ samples.	83
Figure 62	Simulation with nominal thickness (blue curve), estimated thickness (green curve) and measured reflectance (red curve) of S9G SiO ₂ /TiO ₂ samples.	83
Figure 63	Simulation with nominal thickness (blue curve), estimated thickness (green curve) and measured reflectance (red curve) of S8G SiO ₂ /ZrO ₂ samples.	84
Figure 64	Simulation with nominal thickness (blue curve), estimated thickness (green curve) and measured reflectance (red curve) of S10W Au/MgF ₂ samples.	84
Figure 65	Simulation with nominal thickness (blue curve), estimated thickness (green curve) and measured reflectance (red curve) of S11W Pt samples. . .	85

INTRODUCTION

In recent years, space agencies have carried out qualification activities finalized to validate novel optical components for space applications. Future space missions will operate in very hostile environments in terms of particles irradiation and thermal excursion, such as those close to the Sun or to the Jupiter magnetosphere ([1]-[3]). For this reason, it will be fundamental to develop robust optical elements capable to operate in harsh conditions and to prevent the occurrence of any critical optical degradation of their performance. It is known, indeed, that optical performance of the components strongly affects the data outcomes, and their degradation can lead to a misinterpretation of the scientific data due to an uncontrolled change of the instrument response; in a more dramatic scenario, the failure of a component can affect the operational capacity of the whole instrument.

According to the state of the art, the studies on the effect of ions irradiation on coatings ([4]-[7]) and glasses ([8]-[9]) are limited to specific ions species, values of energy and doses, and they generally have the character of a qualification of a specific component in its space operational environment. In addition to this very few results have been published on scientific journals.

The European Space Agency (ESA) has funded the project *Radiation testing of optical coating in space*, lead by the National Research Council of Italy, Institute for Photonics and Nanotechnology, to systematically study the optical components performance degradation due to exposure to protons, alpha particles and electrons. Within this project, several samples including glasses, single-, bi- and multi-layer coatings were properly designed by CNR-IFN Padova and fabricated by Leonardo company. The samples are tested prior and after a huge campaign of irradiation with different particles species and parameters. The project results will then be useful in the development of the JUICE instrumentation.

This thesis is organized as follows:

- The **first chapter** presents the rationale of the project and the global aspects.
- The **second chapter** introduces the concept of *light*, how it propagates and how it interacts with matter.
- The **third chapter** provides a mathematical model to describe how light interacts with optical thin films.

- The **fourth chapter** describes the optical degradation of coatings due to ions implantation and provides a predictive model software.
- The **fifth chapter** presents all the experimental results.
- The **sixth chapter** summarizes the thesis results, future researches and general perspectives.

THE ELECTROMAGNETIC MODEL

Contents

2.1	Maxwell's equations	5
2.2	Constitutive relations	7
2.3	Boundary conditions	9
2.4	Helmholtz equation	11
2.5	Plane wave solution	12
2.6	Polarization	14
2.6.1	Linear polarization	15
2.6.2	Circular polarization	15
2.6.3	Elliptical polarization	16
2.7	The Poynting vector	17

2.1 MAXWELL'S EQUATIONS

We have a complete model that describes the propagation of light through Maxwell's equations [10]. The general form of time-dependent or *integral* form can be written as:

$$\nabla \cdot \bar{\mathcal{D}} = \rho \quad (1)$$

$$\nabla \cdot \bar{\mathcal{B}} = 0 \quad (2)$$

$$\nabla \times \bar{\mathcal{E}} = -\frac{\partial \bar{\mathcal{B}}}{\partial t} \quad (3)$$

$$\nabla \times \bar{\mathcal{H}} = \frac{\partial \bar{\mathcal{D}}}{\partial t} + \bar{\mathcal{J}} \quad (4)$$

where $\bar{\mathcal{E}}$ [V/m] and $\bar{\mathcal{H}}$ [A/m] are the electric and magnetic fields, $\bar{\mathcal{D}}$ [Coul/m²] and $\bar{\mathcal{B}}$ [Wb/m²] are the electric and magnetic flux densities, and ρ and $\bar{\mathcal{J}}$ are the electric charge and electric current densities respectively. The sources of the electromagnetic field are the current $\bar{\mathcal{J}}$ and the electric charge density ρ . In free space, the following simple relations hold between the electric and magnetic field intensities and flux densities:

$$\bar{\mathcal{B}} = \mu_0 \bar{\mathcal{H}} \quad (5)$$

$$\bar{\mathcal{D}} = \epsilon_0 \bar{\mathcal{E}} \quad (6)$$

where $\mu_0 = 4\pi \times 10^{-7}$ [henry/m] is the *permeability* of free space and $\epsilon_0 = 8.854 \times 10^{-12}$ [farad/m] is the *permittivity* of free space.

Equations (1)-(4) are not independent one each other. For instance, if we take the divergence of (3), we have:

$$\nabla \cdot \nabla \times \bar{\mathcal{E}} \equiv 0 = -\frac{\partial}{\partial t}(\nabla \cdot \bar{\mathcal{B}}) \quad (7)$$

which leads to $\nabla \cdot \bar{\mathcal{B}} = 0$, that is, (2). The *continuity condition* can be similarly derived by taking the divergence of (4), giving:

$$\nabla \cdot \bar{\mathcal{J}} + \frac{\partial \rho}{\partial t} = 0 \quad (8)$$

This equation states that charge is conserved, or that current is continuous, since $\nabla \cdot \bar{\mathcal{J}}$ represents the outflow of current at a given point and $\frac{\partial \rho}{\partial t}$ the charge variation with time at the same point.

The above differential equations can be converted to *integral form* through the use of various vector integral theorems. Applying the divergence theorem to (1) and (2) yields:

$$\oint_S \bar{\mathcal{D}} \cdot d\bar{s} = \int_V \rho \, dv = Q \quad (9)$$

$$\oint_S \bar{\mathcal{B}} \cdot d\bar{s} = 0 \quad (10)$$

where Q represents the total charge contained in the closed volume V (enclosed by a closed surface S). In addition, applying Stoke's theorem to (3) and (4) gives:

$$\oint_C \bar{\mathcal{E}} \cdot d\bar{l} = -\frac{\partial}{\partial t} \int_S \bar{\mathcal{B}} \cdot d\bar{s} \quad (11)$$

$$\oint_C \bar{\mathcal{H}} \cdot d\bar{l} = \frac{\partial}{\partial t} \int_S \bar{\mathcal{D}} \cdot d\bar{s} + \int_S \bar{\mathcal{J}} \cdot d\bar{s} = \frac{\partial}{\partial t} \int_S \bar{\mathcal{D}} \cdot d\bar{s} + \mathcal{J} \quad (12)$$

where C represents a closed contour around the surface S and $\mathcal{J} = \int_S \bar{\mathcal{J}} \cdot d\bar{s}$ is the total electric current flow through the surface S .

The above equations are valid for arbitrary time dependence. However, when dealing with electromagnetic theory, the involved fields typically have the form of sinusoidal or harmonic functions. In this case the phasor notation is very convenient, and all field quantities can be assumed to be complex vectors with an implied $e^{i\omega t}$ time dependence. Maxwell's equation in phasor forms can be written as:

$$\nabla \cdot \bar{\mathcal{D}} = \rho \quad (13)$$

$$\nabla \cdot \bar{\mathcal{B}} = 0 \quad (14)$$

$$\nabla \times \bar{\mathcal{E}} = -i\omega \bar{\mathcal{B}} \quad (15)$$

$$\nabla \times \bar{\mathcal{H}} = i\omega \bar{\mathcal{D}} + \bar{\mathcal{J}} \quad (16)$$

The Fourier transform can be used to convert a solution to Maxwell's equations for an arbitrary frequency ω into a solution for arbitrary time dependence.

2.2 CONSTITUTIVE RELATIONS

In the preceding section it was assumed that the electric and magnetic fields were in free-space but, in practice, material bodies are often present. When electromagnetic fields exist in media, the field vectors are related to each other by the *constitutive relations*.

For a dielectric material, an applied electric field \bar{E} causes the polarization of the constituent atoms and molecules to create electric dipole moments that augment the total displacement flux \bar{D} . This additional polarization vector is named *electric polarization* \bar{P}_e , with:

$$\bar{D} = \epsilon_0 \bar{E} + \bar{P}_e \quad (17)$$

In a *linear medium* the electric polarization is linearly related to the applied electric field such that:

$$\bar{P}_e = \epsilon_0 \chi_e \bar{E} \quad (18)$$

where χ_e is named *electric susceptibility* and can be a complex quantity. This gives:

$$\bar{D} = \epsilon_0 \bar{E} + \epsilon_0 \chi_e \bar{E} = \epsilon_0 (1 + \chi_e) \bar{E} = \epsilon \bar{E} \quad (19)$$

where

$$\epsilon = \epsilon_0 (1 + \chi_e) = \epsilon' - i\epsilon'' \quad (20)$$

is the (complex) permittivity of the medium. The imaginary part ϵ'' accounts for losses due to damping of the vibrating dipole moments. In this case we implicitly assumed that \bar{P}_e was a vector parallel to \bar{E} , but this only holds for *isotropic materials*. In the most general case of an anisotropic medium, ϵ takes the form of a tensor of rank two and it can be written in matrix form as:

$$\begin{bmatrix} D_x \\ D_y \\ D_z \end{bmatrix} = \begin{bmatrix} \epsilon_{xx} & \epsilon_{xy} & \epsilon_{xz} \\ \epsilon_{yx} & \epsilon_{yy} & \epsilon_{yz} \\ \epsilon_{zx} & \epsilon_{zy} & \epsilon_{zz} \end{bmatrix} = \begin{bmatrix} E_x \\ E_y \\ E_z \end{bmatrix} \quad (21)$$

For a linear isotropic material, the matrix of (21) reduces to a diagonal matrix with elements ϵ .

The same reasoning can be applied for the magnetic field, in particular:

$$\bar{\mathbf{B}} = \mu_0(1 + \chi_m)\bar{\mathbf{H}} = \mu\bar{\mathbf{H}} \quad (22)$$

where

$$\mu = \mu_0(1 + \chi_m) = \mu' - i\mu'' \quad (23)$$

is the (complex) permeability of the medium. In the most general case of anisotropic materials, then:

$$\begin{bmatrix} B_x \\ B_y \\ B_z \end{bmatrix} = \begin{bmatrix} \mu_{xx} & \mu_{xy} & \mu_{xz} \\ \mu_{yx} & \mu_{yy} & \mu_{yz} \\ \mu_{zx} & \mu_{zy} & \mu_{zz} \end{bmatrix} = \begin{bmatrix} H_x \\ H_y \\ H_z \end{bmatrix} \quad (24)$$

If linear media are assumed, then Maxwell's equations can be rewritten as:

$$\nabla \cdot \bar{\mathbf{D}} = \rho \quad (25)$$

$$\nabla \cdot \bar{\mathbf{B}} = 0 \quad (26)$$

$$\nabla \times \bar{\mathbf{E}} = -i\omega\mu\bar{\mathbf{H}} \quad (27)$$

$$\nabla \times \bar{\mathbf{H}} = i\omega\epsilon\bar{\mathbf{E}} + \bar{\mathbf{J}} \quad (28)$$

and the constitutive relations are

$$\bar{\mathbf{D}} = \epsilon\bar{\mathbf{E}} \quad (29)$$

$$\bar{\mathbf{B}} = \mu\bar{\mathbf{H}} \quad (30)$$

$$\bar{\mathbf{J}} = \sigma\bar{\mathbf{E}} \quad (31)$$

where σ is the conductivity of the considered material.

Maxwell's equations (25)-(28) in differential form require known boundary values for a complete and unique solution.

2.3 BOUNDARY CONDITIONS

Maxwell's equations in integral form can be used to deduce conditions involving the normal and tangential fields at a plane interface between two media.

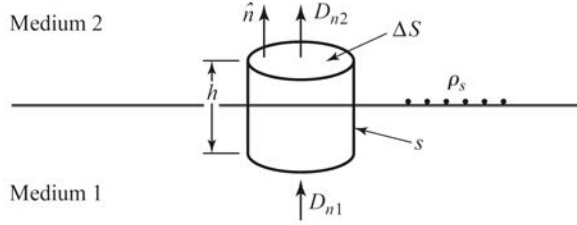


Figure 1: Closed surface S for equation (32).

We can consider a Gaussian pillbox that intersects the interface between two media (Figure [1]). As the cylinder is made smaller and smaller the surface integrals containing the transverse field components vanish and the total contribution of \vec{D} results:

$$\oint_S \vec{D} \cdot d\vec{s} = \oint_V \rho \, dv \quad (32)$$

In particular, in the limit $h \rightarrow 0$, the contribution of D_{tan} through the lateral surface goes to zero, giving:

$$D_{n2} - D_{n1} = \rho_s \quad (33)$$

or equivalently

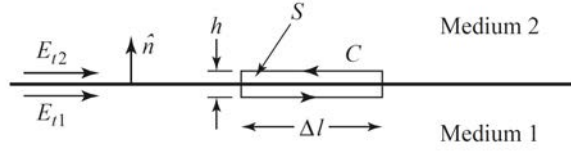
$$\hat{n} \cdot (\vec{D}_2 - \vec{D}_1) = \rho_s \quad (34)$$

where ρ_s is the surface charge density on the interface. A similar result is obtained for the magnetic flux density \vec{B} with the difference that there is no free magnetic charge, respectively:

$$\hat{n} \cdot \vec{B}_2 = \hat{n} \cdot \vec{B}_1 \quad (35)$$

For the tangential components of the electric field we can use the Stokes theorem in connection to the closed contour C shown in Figure [2] and compute:

$$\oint_C \vec{E} \cdot d\vec{l} = -i\omega \oint_S \vec{S} \cdot d\vec{s} \quad (36)$$

Figure 2: Closed contour C for equation (2).

In the limit $h \rightarrow 0$, the surface integral of $\bar{\mathbf{B}}$ vanishes (because $S = h\Delta l$ vanishes), giving:

$$E_{t1} - E_{t2} = 0 \quad (37)$$

or equivalently

$$(\bar{\mathbf{E}}_2 - \bar{\mathbf{E}}_1) \times \hat{\mathbf{n}} = 0 \quad (38)$$

Similarly, for the magnetic fields we find:

$$\hat{\mathbf{n}} \times (\bar{\mathbf{H}}_2 - \bar{\mathbf{H}}_1) = \bar{\mathbf{J}}_s \quad (39)$$

where $\bar{\mathbf{J}}_s$ is an electric surface current density that exist at the interface. Equations (34), (35), (38) and (39) are the most general expressions for the boundary conditions at an arbitrary interface of materials and/or surface currents.

In case of a source-free material, these rewrites as:

$$\hat{\mathbf{n}} \cdot \bar{\mathbf{D}}_2 = \hat{\mathbf{n}} \cdot \bar{\mathbf{D}}_1 \quad (40)$$

$$\hat{\mathbf{n}} \cdot \bar{\mathbf{B}}_2 = \hat{\mathbf{n}} \cdot \bar{\mathbf{B}}_1 \quad (41)$$

$$\bar{\mathbf{E}}_2 \times \hat{\mathbf{n}} = \bar{\mathbf{E}}_1 \times \hat{\mathbf{n}} \quad (42)$$

$$\hat{\mathbf{n}} \times \bar{\mathbf{H}}_2 = \hat{\mathbf{n}} \times \bar{\mathbf{H}}_1 \quad (43)$$

In other words, at the interface between source-free materials, the tangential components of $\bar{\mathbf{E}}$ and $\bar{\mathbf{H}}$ and the normal components of $\bar{\mathbf{D}}$ and $\bar{\mathbf{B}}$ are continuous across it.

2.4 HELMHOLTZ EQUATION

In a source-free, isotropic and homogeneous region, Maxwell's equations in phasor form can be written as:

$$\nabla \cdot \bar{\mathbf{D}} = 0 \quad (44)$$

$$\nabla \cdot \bar{\mathbf{B}} = 0 \quad (45)$$

$$\nabla \times \bar{\mathbf{E}} = -i\omega\mu\bar{\mathbf{H}} \quad (46)$$

$$\nabla \times \bar{\mathbf{H}} = i\omega\varepsilon\bar{\mathbf{E}} \quad (47)$$

These can be solved either for $\bar{\mathbf{E}}$ or $\bar{\mathbf{H}}$. For example, taking the curl of (46) and using (47) we obtain:

$$\nabla \times \nabla \times \bar{\mathbf{E}} = -i\omega\mu (\nabla \times \bar{\mathbf{H}}) = \omega^2\mu\varepsilon\bar{\mathbf{E}} \quad (48)$$

This result can be simplified through the use of vector identity $\nabla \times \nabla \times \bar{\mathbf{A}} = \nabla(\nabla \cdot \bar{\mathbf{A}}) - \nabla^2\bar{\mathbf{A}}$. Then we obtain:

$$\nabla^2\bar{\mathbf{E}} + \omega^2\mu\varepsilon\bar{\mathbf{E}} = 0 \quad (49)$$

because of (29) and (44). Equation (49) is the (*homogeneous*) *Helmholtz equation* for $\bar{\mathbf{E}}$. Since it will be widely used in what follows, we define the *wavenumber* (or *propagation constant*, or *phase constant*) as the quantity:

$$k = \omega\sqrt{\mu\varepsilon} = \frac{2\pi}{\lambda_0}n = \frac{2\pi\nu_0}{c}n \quad (50)$$

where λ_0 (ν_0) is the wavelength (frequency) in vacuum, and n is the refractive index of the medium.

An identical equation for $\bar{\mathbf{H}}$ can be derived, respectively:

$$\nabla^2\bar{\mathbf{H}} + k^2\bar{\mathbf{H}} = 0 \quad (51)$$

2.5 PLANE WAVE SOLUTION

It is convenient to study a particular family of waves named *plane waves* because they are a mathematical base of the solutions of Maxwell's equations. Using the method of separation of variables (see appendix A), the solution for the electric field component is:

$$\begin{aligned}\bar{\mathbf{E}} &= \bar{\mathbf{E}}_0^+ e^{-i(k_x x + k_y y + k_z z)} + \bar{\mathbf{E}}_0^- e^{i(k_x x + k_y y + k_z z)} \\ &= \bar{\mathbf{E}}_0^+ e^{-i\bar{\mathbf{k}} \cdot \bar{\mathbf{r}}} + \bar{\mathbf{E}}_0^- e^{i\bar{\mathbf{k}} \cdot \bar{\mathbf{r}}}\end{aligned}\quad (52)$$

where we have defined a *wavenumber vector* as:

$$\bar{\mathbf{k}} = k_x \hat{\mathbf{x}} + k_y \hat{\mathbf{y}} + k_z \hat{\mathbf{z}} = k \hat{\mathbf{s}} \quad (53)$$

where k is the wavenumber and $\hat{\mathbf{s}}$ is a unit vector in the direction of propagation defined by:

$$\hat{\mathbf{s}} = \alpha \hat{\mathbf{x}} + \beta \hat{\mathbf{y}} + \gamma \hat{\mathbf{z}} \quad (54)$$

Equation (52) states that the mathematical solution of (49) includes the contribution of a *forward* and a *backward* propagating fields, respectively $\bar{\mathbf{E}}_0^-$ and $\bar{\mathbf{E}}_0^+$. In the following analysis, however, we only consider the first component for simplicity of notation. The expression of the magnetic field is retrieved from (46), respectively:

$$\bar{\mathbf{H}} = \frac{i}{\omega \mu} \nabla \times \bar{\mathbf{E}} = y(\hat{\mathbf{s}} \times \bar{\mathbf{E}}) \quad (55)$$

where we used $\nabla = -i\bar{\mathbf{k}} = -ik\hat{\mathbf{s}}$ and where $y = \frac{k}{\omega \mu}$ is the optical admittance. Notice that, from (44), we obtain:

$$\nabla \cdot \bar{\mathbf{E}} = \nabla \cdot (\bar{\mathbf{E}}_0 e^{-i\bar{\mathbf{k}} \cdot \bar{\mathbf{r}}}) = \bar{\mathbf{E}}_0 \cdot \nabla e^{-i\bar{\mathbf{k}} \cdot \bar{\mathbf{r}}} = 0 \quad (56)$$

that is:

$$\bar{\mathbf{k}} \cdot \bar{\mathbf{E}}_0 = 0 \quad (57)$$

This result suggests that the electric field amplitude vector $\bar{\mathbf{E}}_0$ must be perpendicular to the direction of propagation $\hat{\mathbf{s}}$. Moreover, from (55), we find that the magnetic field vector $\bar{\mathbf{H}}$ lies in a plane normal to $\bar{\mathbf{k}}$ and that it is perpendicular to $\bar{\mathbf{E}}$.

The time domain expression for the electric field can be found as:

$$\begin{aligned}\bar{\mathcal{E}}(\bar{\mathbf{r}}, t) &= \Re\{\bar{\mathbf{E}} e^{i\omega t}\} \\ &= \Re\{\bar{\mathbf{E}}_0 e^{-i\bar{\mathbf{k}} \cdot \bar{\mathbf{r}}} e^{i\omega t}\} \\ &= \bar{\mathbf{E}}_0 \cos(\omega t - \bar{\mathbf{k}} \cdot \bar{\mathbf{r}})\end{aligned}\quad (58)$$

This term represents a wave travelling in the direction of \bar{k} because to maintain a fixed point on the wave ($\omega t - \bar{k} \cdot \bar{r} = \text{const}$) one must move in the \bar{k} direction as time increases. Given the amplitude \bar{E}_0 (typically constant), $\bar{E}(\bar{r}, t)$ is a cosinusoidal function that propagates with *phase velocity*:

$$v_p = \frac{\omega}{k} \quad (59)$$

This behaviour is pictured in Figure [3].

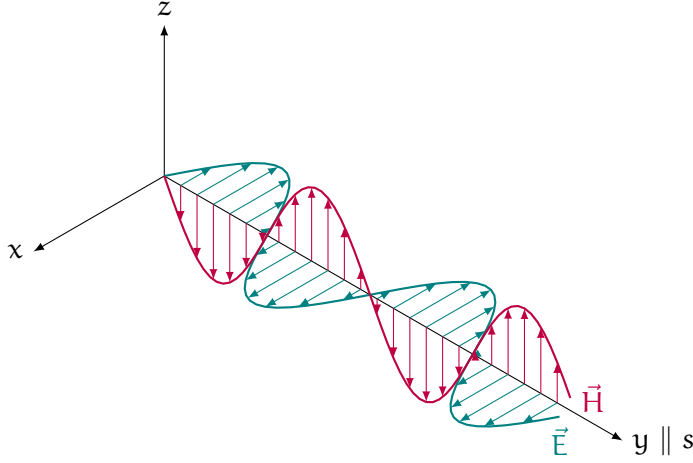


Figure 3: Propagation of an electromagnetic wave

In all previous calculation we have considered an (ideal) lossless medium, for which ϵ and μ are real numbers and so it is for k . This is actually an approximation since there exist no material in nature that exhibits no absorption. To account for this phenomenon, we have to solve the general form of Maxwell's equations:

$$\nabla \times \bar{E} = -i\omega\mu\bar{H} \quad (60)$$

$$\nabla \times \bar{H} = i\omega\epsilon\bar{E} + \sigma\bar{E} \quad (61)$$

or the corresponding *Helmholtz* equation:

$$\nabla^2 \bar{E} + \omega^2 \mu \epsilon \left(1 - i \frac{\sigma}{\omega \epsilon}\right) \bar{E} = 0 \quad (62)$$

Note that the structure is the same as (49), with the difference that the wavenumber is now complex:

$$K^2 = \omega^2 \mu \epsilon - i\omega \mu \sigma \quad (63)$$

For equation (59) to be verified it is necessary that:

$$v_p^2 = \frac{\omega^2}{\omega^2 \mu \epsilon \left(1 - i \frac{\sigma}{\omega \epsilon}\right)} \quad (64)$$

Using the identity $c^2 = \frac{1}{\mu_0 \epsilon_0}$ and rearranging (64) we obtain:

$$N^2 = \epsilon_r \mu_r - i \frac{\mu_r \sigma}{\omega \epsilon_0} \quad (65)$$

where we have defined the dimensionless parameter $N = \frac{c}{v}$ and used the relative permittivity ϵ_r and permeability μ_r of the considered material. This result implies that N is of the form:

$$N = \frac{c}{v} = n - i\beta \quad (66)$$

The term N is the *complex refractive index* and β is named *extinction coefficient*.

With this results, equation (58) becomes:

$$\begin{aligned} \bar{\mathcal{E}}(\bar{r}, t) &= \Re\{\bar{E}_0 e^{-i(\bar{k}' - i\bar{k}'') \cdot \bar{r}} e^{i\omega t}\} \\ &= \bar{E}_0 e^{-\bar{k}'' \cdot \bar{r}} \cos(\omega t - \bar{k}' \cdot \bar{r}) \end{aligned} \quad (67)$$

We see that in the equation (67) the term $e^{-\bar{k}'' \cdot \bar{r}}$ takes into account the material absorption, which appears in the form of an exponential decay, while the term $\cos(-\bar{k}' \cdot \bar{r} + \omega t)$ describes the wave propagation in the medium.

In conclusion, we can define the most general expression of *wavelength* and *phase velocity* for a plane wave in a lossy medium, respectively, as:

$$v_p = \frac{\omega}{|\mathbf{K}|} \quad (68)$$

$$\lambda = \frac{2\pi}{|\mathbf{K}|} \quad (69)$$

2.6 POLARIZATION

The polarization of a plane wave refers to the orientation of the electric field vector, which can either be fixed or time-varying. In the most simple case this is pointing in a fixed direction and the plane wave is said to be *linearly polarized*.

Consider now the superposition of an \hat{x} and \hat{y} linearly polarized plane waves propagating in free-space in the z direction and with amplitudes E_1 and E_2 respectively. The total electric field can be expressed as:

$$\bar{E} = (E_1 \hat{x} + E_2 \hat{y}) e^{-ik_0 z} \quad (70)$$

Three possible scenarios are described.

2.6.1 Linear polarization

If $E_1 \neq 0$ and $E_2 = 0$ then the resulting plane wave is linearly polarized in the \hat{x} direction. Similarly, if $E_1 = 0$ and $E_2 \neq 0$ it is linearly polarized in the \hat{y} direction. If both amplitudes E_1 and E_2 are different from zero (and real), we obtain a plane wave linearly polarized at the general angle formed with the x -axis.:

$$\phi = \tan^{-1} \frac{E_2}{E_1} \quad (71)$$

2.6.2 Circular polarization

If $E_1 = iE_2 = E_0$, with E_0 real, we obtain:

$$\bar{E} = E_0(\hat{x} - i\hat{y})e^{-ik_0z} \quad (72)$$

The time domain expression of this field is:

$$\begin{aligned} \bar{E}(z, t) &= E_0 [\hat{x} \cos(\omega t - k_0z) + \hat{y} \cos(\omega t - k_0z - \pi/2)] \\ &= E_0 [\hat{x} \cos(\omega t - k_0z) + \hat{y} \sin(\omega t - k_0z)] \end{aligned} \quad (73)$$

This expression shows that the electric field vector varies in time along the z -axis. For example, at $z = 0$, (73) reduces to:

$$\bar{E}(0, t) = E_0 [\hat{x} \cos(\omega t) + \hat{y} \sin(\omega t)] \quad (74)$$

Given ω , when t increases, \bar{E} rotates counterclockwise from the x -axis with modulus:

$$\rho = \sqrt{E_0^2(\cos^2(\omega t) + \sin^2(\omega t))} = E_0 \quad (75)$$

and forming an angle which increases linearly with time:

$$\phi = \tan^{-1} \frac{\sin(\omega t)}{\cos(\omega t)} = \omega t \quad (76)$$

This type of plane wave is referred to as a *right hand circularly polarized* (RHCP) wave. Similarly, when $E_1 = -iE_2 = E_0$, the resulting electric field vector rotates clockwise and the wave is *left hand circularly polarized* (LHCP).

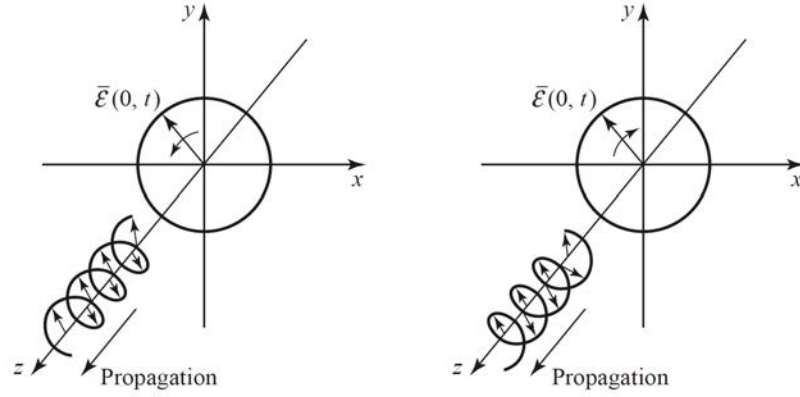


Figure 4: RHCP (left) and LHCP (right) plane wave propagation.

2.6.3 Elliptical polarization

The remaining case requires both amplitudes to be nonzero and different one each other, respectively E_1 and $E_2 e^{i\varphi}$. The term φ refers to the difference in phase between the two components. The resulting electric field vector is:

$$\bar{E} = (E_1 \hat{x} + E_2 e^{i\varphi} \hat{y}) e^{-ik_0 z} \quad (77)$$

and the corresponding time-dependent expression at $z = 0$ is:

$$\bar{E}(0, t) = \hat{x} E_1 \cos(\omega t) + \hat{y} E_2 \cos(\omega t + \varphi) \quad (78)$$

In this case, the modulus and phase of $\bar{E}(0, t)$ cannot be expressed in closed form. However, it can be shown that the tip of the electric field vector rotates in the xy -plane describing an ellipse with equation:

$$\frac{E_x^2}{E_1^2} + \frac{E_y^2}{E_2^2} - 2 \cos \varphi \frac{E_x E_y}{E_1 E_2} = \sin^2 \varphi \quad (79)$$

where we used the notation $E_x = E_1 \cos(\omega t)$ and $E_y = E_2 \cos(\omega t + \varphi)$. Note that the rotation can be either clockwise or counterclockwise depending on φ . This type of plane wave is the more general, and from this the other cases of linear and circular polarizations can be derived as particular solutions.

2.7 THE POYNTING VECTOR

An important feature of electromagnetic radiation is that it can store electric and magnetic energy and carry power that may be transmitted or dissipated as loss. The *Poynting's theorem* provides a power balance equation, and its derivation is here proposed.

If we have an electric source current \bar{J}_s and a conduction current $\sigma\bar{E}$, as defined in (31), then the total electric current density is $\bar{J} = \bar{J}_s + \sigma\bar{E}$. Multiplying (27) by \bar{H}^* and multiplying the conjugate of (28) by \bar{E} yields:

$$\begin{aligned}\bar{H}^* \cdot (\nabla \times \bar{E}) &= -i\omega\mu|\bar{H}|^2 \\ \bar{E} \cdot (\nabla \times \bar{H}^*) &= \bar{E} \cdot \bar{J}_s^* + \sigma|\bar{E}|^2 - i\omega\varepsilon^*|\bar{E}|^2\end{aligned}$$

Using the vector identity $\nabla \cdot (\bar{A} \times \bar{B}) = (\nabla \times \bar{A}) \cdot \bar{B} - (\nabla \times \bar{B}) \cdot \bar{A}$ we find:

$$\begin{aligned}\nabla \cdot (\bar{E} \times \bar{H}^*) &= \bar{H}^* \cdot (\nabla \times \bar{E}) - \bar{E} \cdot (\nabla \times \bar{H}^*) \\ &= -\sigma|\bar{E}|^2 + i\omega(\varepsilon^*|\bar{E}|^2 - \mu|\bar{H}|^2) - \bar{E} \cdot \bar{J}_s^*\end{aligned}$$

We can now integrate over a volume V and apply the divergence theorem:

$$\begin{aligned}\int_V \nabla \cdot (\bar{E} \times \bar{H}^*) dv &= \oint_S \bar{E} \times \bar{H}^* \cdot d\bar{s} \\ &= -\sigma \int_V |\bar{E}|^2 dv + i\omega \int_V (\varepsilon^*|\bar{E}|^2 - \mu|\bar{H}|^2) dv - \int_V \bar{E} \cdot \bar{J}_s^* dv\end{aligned}$$

where S is an arbitrary closed surface enclosing the volume V . Allowing $\varepsilon = \varepsilon' - i\varepsilon''$ and $\mu = \mu' - i\mu''$ to be complex quantities to account for losses, we can rewrite the previous equation as:

$$\begin{aligned}-\frac{1}{2} \int_V \bar{E} \cdot \bar{J}_s^* dv &= \frac{1}{2} \oint_S \bar{E} \times \bar{H}^* \cdot d\bar{s} + \frac{\sigma}{2} \int_V |\bar{E}|^2 dv \\ &\quad + \frac{\omega}{2} \int_V (\varepsilon''|\bar{E}|^2 + \mu''|\bar{H}|^2) dv + i\frac{\omega}{2} \int_V (\mu'|\bar{H}|^2 - \varepsilon'|\bar{E}|^2) dv\end{aligned}\tag{80}$$

This result is known as *Poynting's theorem*, after the physicist J. H. Poynting (1852-1914). The integral on the left-hand side represents the complex power P_s delivered by the source \bar{J}_s inside S . The first integral on the right-hand side represents complex power P_0 flow out of the closed surface S . If we define a quantity \bar{S} , called the *Poynting vector*, as:

$$\bar{S} = \bar{E} \times \bar{H}^*\tag{81}$$

then this power can be expressed as:

$$P_0 = \frac{1}{2} \oint_S \bar{\mathbf{E}} \times \bar{\mathbf{H}}^* \cdot d\bar{\mathbf{s}} = \frac{1}{2} \oint_S \bar{\mathbf{S}} \cdot d\bar{\mathbf{s}} \quad (82)$$

The second and third integrals are real quantities representing the time-average power P_l dissipated in the volume V due to conductivity, dielectric, and magnetic losses. Finally, the last integral can be seen to be related to the stored electric and magnetic energies, and it can be shown to be equal to $2i\omega(W_m - W_e)$ where W_e and W_m are the time-average stored electric and magnetic energies in a volume V . In other words, this complex power balance equation states that the power delivered by the sources (P_s) is equal to the sum of the power transmitted through the surface (P_0), the power lost to heat in the volume (P_l), and 2ω times the net reactive energy stored in the volume. Mathematically, this expresses as:

$$P_s = P_0 + P_l + 2i\omega(W_m - W_e) \quad (83)$$

The mean value of the Poynting vector is defined as the *irradiance*. For a plane wave propagating in a homogeneous, isotropic and lossy medium, the Poynting vector has the same direction of the wavevector $\bar{\mathbf{k}}$. In addition, from equation (55), we have a precise relation between the electric and magnetic fields. The irradiance can then be computed as:

$$\bar{\mathbf{I}}(\bar{\mathbf{r}}) = \Re[\bar{\mathbf{S}}] = \frac{1}{2} \Re[\bar{\mathbf{E}} \times \bar{\mathbf{H}}^*] = \frac{1}{2} \Re[y^*] |\bar{\mathbf{E}}|^2 e^{-2k'' \cdot \bar{\mathbf{r}}} \hat{\mathbf{s}} \quad (84)$$

The lossless case is retrieved by (84) by imposing $k'' = 0$ and y to be real, respectively:

$$\bar{\mathbf{I}} = \frac{1}{2} y |\bar{\mathbf{E}}|^2 \hat{\mathbf{s}} \quad (85)$$

Since we will often deal with the amplitude values rather than the vector expression of irradiance, we introduce the following notation:

$$I = \frac{1}{2} y |\bar{\mathbf{E}}|^2 = \frac{1}{2} n y_0 |\bar{\mathbf{E}}|^2 \quad (86)$$

where y_0 is the optical admittance of vacuum.

OPTICAL THIN FILMS THEORY

Contents

3.1	The simple boundary: lossless case	21
3.1.1	s-polarized incident wave	22
3.1.2	p-polarized incident wave	24
3.1.3	The tilted optical admittance	26
3.2	The simple boundary: lossy case	27
3.2.1	p-polarized light	29
3.2.2	s-polarized light	29
3.3	Thin film on a substrate	30
3.4	Assembly of thin films on a substrate	32
3.5	Reflectance, transmittance and absorbance	34
3.6	Potential Transmittance	36

3.1 THE SIMPLE BOUNDARY: LOSSLESS CASE

We now move the first step toward a more *optical* perspective [11]. In optics, thin films typically consist of a number of boundaries between various homogeneous media. The knowledge of the processes that govern the interaction between the electromagnetic radiation and these boundaries is fundamental to correctly manage the optical properties of the whole structures. In this regards, a single boundary is the simplest case.

We firstly consider the lossless case. For any general direction of the vector amplitude of the incident wave (E_i) we quickly find that the application of the boundary conditions leads into complicated expressions for the vector amplitudes of reflected and transmitted waves. This problem can be overcome by defining two independent configurations in which the electric field vector is either aligned or transverse in the plane of incidence. In the first case we refer to the wave as p-polarized (or TM), while in the second one the wave is said to be s-polarized (or TE).

Any incident wave of arbitrary polarization can therefore be split into two components having these simple orientations. The transmitted and reflected components can be calculated for each orientation separately and then combined to obtain the resultant.

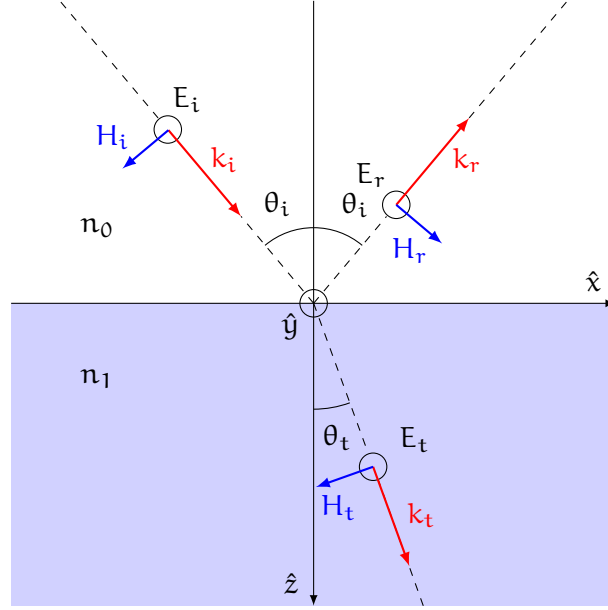
3.1.1 *s*-polarized incident wave

Figure 5: Reflection and Transmission at an interface for an impinging *s*-polarized plane wave.

The case of study is pictured in Figure [5]. The electric and magnetic fields of the three principal components are:

$$\begin{aligned}
 \bar{E}_i(x, z) &= \hat{y} E_i e^{-i k_i (\sin \theta_i \cdot \hat{x} + \cos \theta_i \cdot \hat{z})} \\
 \bar{E}_r(x, z) &= \hat{y} E_r e^{-i k_r (\sin \theta_i \cdot \hat{x} - \cos \theta_i \cdot \hat{z})} \\
 \bar{E}_t(x, z) &= \hat{y} E_t e^{-i k_t (\sin \theta_t \cdot \hat{x} + \cos \theta_t \cdot \hat{z})}
 \end{aligned} \tag{87}$$

and

$$\begin{aligned}
 \bar{H}_i(x, z) &= y_0 E_i [\sin \theta_i \cdot \hat{z} - \cos \theta_i \cdot \hat{x}] e^{-i k_i (\sin \theta_i \cdot \hat{x} + \cos \theta_i \cdot \hat{z})} \\
 \bar{H}_r(x, z) &= y_0 E_r [\sin \theta_i \cdot \hat{z} + \cos \theta_i \cdot \hat{x}] e^{-i k_r (\sin \theta_i \cdot \hat{x} - \cos \theta_i \cdot \hat{z})} \\
 \bar{H}_t(x, z) &= y_1 E_t [\sin \theta_t \cdot \hat{z} - \cos \theta_t \cdot \hat{x}] e^{-i k_t (\sin \theta_t \cdot \hat{x} + \cos \theta_t \cdot \hat{z})}
 \end{aligned} \tag{88}$$

From section 2.3 we know that the tangential components of \bar{E} and \bar{H} must be continuous across the boundary. However, given the reference system of Figure [5], it seems worthwhile to operate with amplitude components rather than vectors. Since the *Snell's law* is implicitly verified, indeed, we only need to consider the vector amplitudes.

We can now impose the parallel components of \bar{E} and \bar{H} to be continuous across the interface:

1. Parallel component of the electric fields:

$$E_i + E_r = E_t \tag{89}$$

2. Parallel component of the magnetic fields:

$$y_0 \cos \theta_i E_i - y_0 \cos \theta_i E_r = y_1 \cos \theta_t E_t \quad (90)$$

We can eliminate E_t to give:

$$y_0 \cos \theta_i (E_i + E_r) = y_1 \cos \theta_t (E_i + E_r) \quad (91)$$

from which:

$$\frac{E_r}{E_i} = \frac{y_0 \cos \theta_i - y_1 \cos \theta_t}{y_0 \cos \theta_i + y_1 \cos \theta_t} \quad (92)$$

Similarly, eliminating E_r :

$$y_0 \cos \theta_0 (2E_i - E_t) = y_1 \cos \theta_1 E_t \quad (93)$$

from which:

$$\frac{E_t}{E_i} = \frac{2y_0 \cos \theta_i}{y_0 \cos \theta_i + y_1 \cos \theta_t} \quad (94)$$

Equations (92) and (94) are the *reflection* and *transmission* coefficients for s-polarized light, respectively:

$$\rho_s = \frac{E_r}{E_i} = \frac{y_0 \cos \theta_i - y_1 \cos \theta_t}{y_0 \cos \theta_i + y_1 \cos \theta_t} = \frac{n_0 \cos \theta_i - n_1 \cos \theta_t}{n_0 \cos \theta_i + n_1 \cos \theta_t} \quad (95)$$

$$\tau_s = \frac{E_t}{E_i} = \frac{2y_0 \cos \theta_i}{y_0 \cos \theta_i + y_1 \cos \theta_t} = \frac{2n_0 \cos \theta_i}{n_0 \cos \theta_i + n_1 \cos \theta_t} \quad (96)$$

We now examine the energy balance at the boundary. The parallel components of the irradiances of the three principal waves are:

$$I_i = \frac{1}{2} \Re[E_i H_i^*] = \frac{1}{2} \Re[E_i (y_0 E_i \cos \theta_i)^*] = \frac{1}{2} y_0 \cos \theta_i |E_i|^2 \quad (97)$$

$$I_r = \frac{1}{2} \Re[E_r H_r^*] = \frac{1}{2} y_0 \cos \theta_i \rho_s^2 |E_i|^2 = \rho_s^2 I_i \quad (98)$$

$$I_t = \frac{1}{2} \Re[E_t H_t^*] = \frac{1}{2} y_1 \cos \theta_t \tau_s^2 |E_i|^2 = \frac{y_1 \cos \theta_t}{y_0 \cos \theta_i} \tau_s^2 I_i \quad (99)$$

where we used the just computed reflection and transmission coefficients for which $E_r = \rho_s E_i$ and $E_t = \tau_s E_i$. We define the *reflectance* R as the ratio of the reflected and incident irradiances and the *transmittance* T as the ratio of the transmitted and incident irradiances, respectively:

$$R_s = \frac{I_r}{I_i} = \rho_s^2 = \left(\frac{y_0 \cos \theta_i - y_1 \cos \theta_t}{y_0 \cos \theta_i + y_1 \cos \theta_t} \right)^2 \quad (100)$$

$$T_s = \frac{I_t}{I_i} = \frac{y_1 \cos \theta_t}{y_0 \cos \theta_i} \tau_s^2 = \frac{4y_0 \cos \theta_i y_1 \cos \theta_t}{(y_0 \cos \theta_i + y_1 \cos \theta_t)^2} \quad (101)$$

or equivalently:

$$R_s = \left(\frac{n_0 \cos \theta_i - n_1 \cos \theta_t}{n_0 \cos \theta_i + n_1 \cos \theta_t} \right)^2 \quad (102)$$

$$T_s = \frac{4n_0 \cos \theta_i n_1 \cos \theta_t}{(n_0 \cos \theta_i + n_1 \cos \theta_t)^2} \quad (103)$$

Since the boundary is of zero thickness, it can only transfer energy from one medium to the other without supplying or extracting energy from the various waves. Because of that the Poynting vector will be continuous across the boundary:

$$\begin{aligned} \frac{1}{2} \Re[(E_i + E_r)(y_0 \cos \theta_i E_i - y_0 \cos \theta_i E_r)^*] &= \frac{1}{2} \Re[E_t(y_1 \cos \theta_t E_t)] \\ \frac{1}{2} y_0 \cos \theta_i |E_i|^2 (1 - \rho_s^2) &= \frac{1}{2} y_0 \cos \theta_i |E_i|^2 \tau_s^2 \\ I_i (1 - R_s) &= I_t T \end{aligned}$$

from which we find that the total energy flow is conserved.

$$R + T = 1 \quad (104)$$

3.1.2 *p-polarized incident wave*

A similar procedure can be applied in the case of a p-polarized plane wave. The boundary conditions are:

1. Parallel component of the electric fields:

$$E_i \cos \theta_0 + E_r \cos \theta_0 = E_t \cos \theta_t \quad (105)$$

2. Parallel component of the magnetic fields:

$$y_0 E_i + y_0 E_r = y_1 E_t \quad (106)$$

We can eliminate E_t to give:

$$y_0(E_i - E_t) = y_1 \frac{\cos \theta_i}{\cos \theta_t} (E_i + E_t) \quad (107)$$

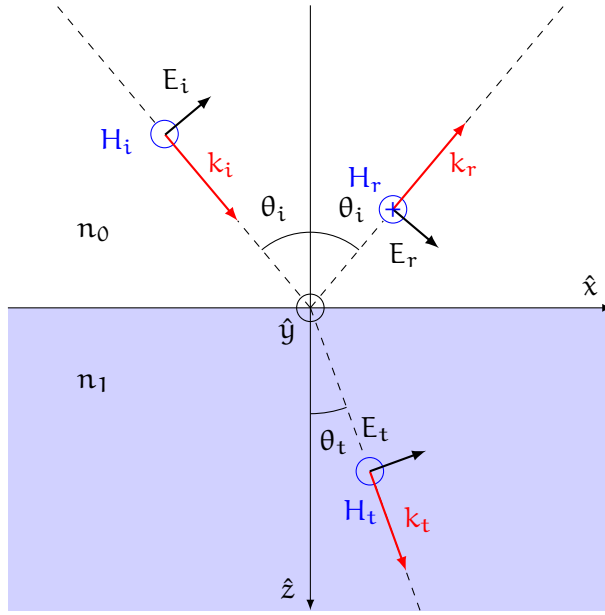


Figure 6: Reflection and Transmission at an interface for an impinging p-polarized plane wave.

from which:

$$\frac{E_r}{E_i} = \frac{y_0 \cos \theta_t - y_1 \cos \theta_i}{y_0 \cos \theta_t + y_1 \cos \theta_i} \quad (108)$$

Similarly, eliminating E_r :

$$\cos \theta_i \left(2E_i - \frac{y_1}{y_0} E_t \right) = E_t \cos \theta_t \quad (109)$$

from which:

$$\frac{E_t}{E_i} = \frac{2y_0 \cos \theta_i}{y_0 \cos \theta_t + y_1 \cos \theta_i} \quad (110)$$

Equations (108) and (110) are the *reflection* and *transmission* coefficients for p-polarized light, respectively:

$$\rho_p = \frac{E_r}{E_i} = \frac{y_0 \cos \theta_t - y_1 \cos \theta_i}{y_0 \cos \theta_t + y_1 \cos \theta_i} \quad (111)$$

$$\tau_p = \frac{E_t}{E_i} = \frac{2y_0 \cos \theta_i}{y_0 \cos \theta_t + y_1 \cos \theta_i} \quad (112)$$

Reflectance and transmittance for p-polarized incident light are then computed as in (100) and (101):

$$\begin{aligned} R_p &= \frac{I_r}{I_i} = \rho_p^2 = \left(\frac{y_0 \cos \theta_t - y_1 \cos \theta_i}{y_0 \cos \theta_t + y_1 \cos \theta_i} \right)^2 = \\ &= \left(\frac{n_0 \cos \theta_t - n_1 \cos \theta_i}{n_0 \cos \theta_t + n_1 \cos \theta_i} \right)^2 \end{aligned} \quad (113)$$

$$\begin{aligned} T_p &= \frac{I_t}{I_i} = \frac{y_1 \cos \theta_t}{y_0 \cos \theta_i} \tau_p^2 = \frac{4y_0 \cos \theta_i y_1 \cos \theta_t}{(y_0 \cos \theta_t + y_1 \cos \theta_i)^2} = \\ &= \frac{4n_0 \cos \theta_i n_1 \cos \theta_t}{(n_0 \cos \theta_t + n_1 \cos \theta_i)^2} \end{aligned} \quad (114)$$

Note that also in this case the $R + T + 1$ rule is preserved.

3.1.3 The tilted optical admittance

In what follows we introduce a notation that will simplify the mathematical analysis of thin films. From equation (55) we have a relationship that links the vectors \vec{H} and $(\hat{s} \times \vec{E})$ by the optical admittance y , respectively $\vec{H} = y(\hat{s} \times \vec{E})$. However, we find it convenient to deal with E and H , i.e., the components of the electric and magnetic field vectors that are parallel to the boundary. We can therefore introduce a "tilted" optical admittance which connects E and H as:

$$\eta = \frac{H}{E} \quad (115)$$

At normal incidence, $\eta = y = ny_0$ (do not confuse general expression for the optical admittance of vacuum y_0 with the optical admittance in a medium with refractive index n_0 , which is still y_0). At oblique incidence we find:

$$\eta_s = \frac{y}{\cos \theta} = \frac{ny_0}{\cos \theta} \quad (116)$$

$$\eta_p = y \cos \theta = ny_0 \cos \theta \quad (117)$$

where θ and y are those appropriate to the particular medium. With this notation, for both cases, we have a single expression for each parameter that does not depend on the polarization but only on the materials characteristics, respectively:

$$\begin{aligned} \rho &= \frac{\eta_0 - \eta_1}{\eta_0 + \eta_1} & R &= \left(\frac{\eta_0 - \eta_1}{\eta_0 + \eta_1} \right)^2 \\ \tau &= \frac{2\eta_0}{\eta_0 + \eta_1} & T &= \frac{4\eta_0\eta_1}{(\eta_0 + \eta_1)^2} \end{aligned} \quad (118)$$

These expressions can be used to compute the variation of reflectance of simple boundaries between extended lossless media.

3.2 THE SIMPLE BOUNDARY: LOSSY CASE

We now proceed our analysis in a more general lossy scenario. It can be shown that the equations for the reflection and transmission coefficients are formally the same as those we already computed for the lossless case, the only difference given by the use of complex refractive indexes, namely $N_0 = n_0 - i\beta_0$ and $N_1 = n_1 - i\beta_1$. In order to compute irradiance and transmittance, however, we have to redefine the coupling between the incident and reflected fields that occurs in absorbing media, and from this compute the energy transport according to the Poynting's theorem.

In what follows we will assume the incident medium to be sufficiently free of absorption. This is reasonable for any experiment to be carried out since this is typically not heavily absorbing, but does not mean that absorbing media in thin-film stacks would not be considered at all. With this being said, we start by considering the phase factors of the three principal waves in the scheme of Figure [7]:

$$\begin{aligned} \exp\{-i(\bar{k}_i \cdot \bar{r})\} &= \exp\{-ik_i(\sin \theta_i x + \cos \theta_i z)\} \\ \exp\{-i(\bar{k}_r \cdot \bar{r})\} &= \exp\{-ik_r(\sin \theta_i x - \cos \theta_i z)\} \\ \exp\{-i(\bar{k}_t \cdot \bar{r})\} &= \exp\{-ik_t(\alpha x + \gamma z)\} \end{aligned} \quad (119)$$

where α and γ are the only unknown and follows by how we have defined \bar{k} (equations (53) and (54)).

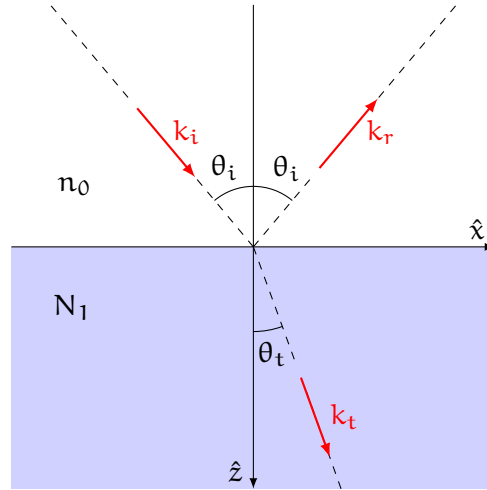


Figure 7: Wavevector decomposition at an interface for an impinging plane wave.

The phase factors must be equal for all x at the boundary $z = 0$, that is:

$$k_t \alpha = \frac{2\pi N_1}{\lambda} \alpha = k_i \sin \theta_i = \frac{2\pi n_0}{\lambda} \sin \theta_i$$

which gives:

$$\alpha = \frac{n_0 \sin \theta_i}{N_1} = \frac{n_0 \sin \theta_i}{n_1 - i\beta_1} \quad (120)$$

Then, since $\alpha^2 + \gamma^2 = 1$, we can write:

$$\begin{aligned} \gamma &= (1 - \alpha^2)^{\frac{1}{2}} = \left[1 - \left(\frac{n_0 \sin \theta_i}{n_1 - i\beta_1} \right)^2 \right]^{\frac{1}{2}} \\ &= \frac{(n_1^2 - \beta_1^2 - i2n_1\beta_1 - n_0 \sin \theta_i)^{\frac{1}{2}}}{n_1 - i\beta_1} \end{aligned} \quad (121)$$

The quantity within the square root is either in the third ($n_1^2 - \beta_1^2 - n_0 \sin \theta_i < 0$) or in the fourth quadrant ($n_1^2 - \beta_1^2 - n_0 \sin \theta_i > 0$) since the $-2n_1\beta_1$ is strictly negative. In both cases the square roots are in the fourth quadrant, and the solution is of the form $(a - ib)$. The expression for γ becomes:

$$\gamma = \frac{a - ib}{n_1 - i\beta_1} \quad (122)$$

If we substitute this value in the phase factor of the transmitted wave we find:

$$\begin{aligned} \exp\{-i(\vec{k}_t \cdot \vec{r})\} &= \exp\{-ik_t(\alpha x + \gamma z)\} \\ &= \exp\left\{-i \frac{2\pi(n_1 - i\beta_1)}{\lambda} \left(\frac{n_0 \sin \theta_i}{n_1 - i\beta_1} x + \frac{a - ib}{n_1 - i\beta_1} z \right)\right\} \\ &= \exp\left\{-\frac{2\pi}{\lambda} bz\right\} \exp\left\{-i \left[(\dots) + \frac{2\pi}{\lambda} az \right]\right\} \end{aligned} \quad (123)$$

This result suggests that the wave is attenuated in the z direction while the propagation direction is determined by direction cosines that can be extracted from:

$$\frac{2\pi n_0 \sin \theta_i}{\lambda} x + \frac{2\pi a}{\lambda} z \quad (124)$$

Such a wave is known as *inhomogeneous*.

At this point we have to calculate the tilted admittance connected to such a wave.

3.2.1 *p-polarized light*

For a p-polarized wave the \vec{H} vector is parallel to the boundary in the x -direction and so $\vec{H} = H_y \hat{y}$. The component of \vec{E} parallel to the boundary will then be in the x -direction, respectively $E_x \hat{x}$. Starting from equation (16) and using (29),(31) and (65) we can write:

$$\begin{aligned}\nabla \times \vec{H} &= i\omega\epsilon\vec{E} + \sigma\vec{E} \\ &= (i\omega\epsilon + \sigma)\vec{E} \\ &= i\frac{\omega N^2}{c^2\mu}\vec{E}\end{aligned}$$

The tangential component of $\nabla \times \vec{H}$ is in the x -direction such that

$$\begin{aligned}-i\frac{2\pi N}{\lambda}\gamma(\hat{z} \times \hat{y}) &= i\frac{\omega N^2}{c^2\mu}E_x \hat{x} \\ i\frac{2\pi N}{\lambda}\gamma \hat{x}H_y &= i\frac{\omega N^2}{c^2\mu}E_x \hat{x}\end{aligned}$$

where we used the property $-(\hat{z} \times \hat{y}) = \hat{x}$. The tilted admittance for p-polarized light is then:

$$\eta_p = \frac{H_y}{E_x} = \frac{\omega N \lambda}{2\pi c^2 \mu \gamma} = \frac{y}{\gamma} \quad (125)$$

3.2.2 *s-polarized light*

For a s-polarized wave we can start from equation (15) and follow a similar analysis, knowing that \vec{E} is now along the y -axis. The tilted admittance in this case results:

$$\eta_s = \frac{H_x}{E_y} = y\gamma \quad (126)$$

We should note at this stage that, provided we include the possibility of complex angles, the formulation of the absorption-free case applies equally well to absorbing media in the case:

$$\begin{aligned}\alpha &= \sin \theta_t \\ \gamma &= \cos \theta_t\end{aligned}$$

Because of that γ can be identified with $\cos \theta$. Consequently, equations (125) and (126) rewrites as:

$$\eta_p = \frac{y}{\cos \theta} \quad (127)$$

$$\eta_s = y \cos \theta \quad (128)$$

The calculation of reflectance and transmittance follows the same pattern as before, in particular:

$$\begin{aligned} R &= \left(\frac{\eta_0 - \eta_1}{\eta_0 + \eta_1} \right) \left(\frac{\eta_0 - \eta_1}{\eta_0 + \eta_1} \right)^* \\ T &= \frac{4\eta_0 \Re[\eta_1]}{(\eta_0 + \eta_1)(\eta_0 + \eta_1)^*} \end{aligned} \quad (129)$$

These two equations can be used to evaluate reflectance and transmittance at an interface in case of a transparent incident medium (η_0 real). Notice that the absorption-free case follows by assuming also the second medium to be transparent.

3.3 THIN FILM ON A SUBSTRATE

A simple extension of the above analysis occurs in the case of a thin, plane, parallel film of material covering the surface of a substrate. We say that the film is thin when interference effects can be detected in the reflected or transmitted light. The same film can appear thin or thick depending entirely on the illumination conditions. The thick case can be shown to be identical with the thin case integrated over a sufficiently wide wavelength range or a sufficiently large range of angles of incidence. Normally, we find that the films on the substrates can be treated as thin while the substrates supporting the films can be considered thick.

Consider a layer of thickness d "sandwiched" between two (homogeneous) layers of different refractive indexes as pictured in Fig. [8]. The presence of two (or more) interfaces means that a number of waves will be produced by successive reflections and the properties of the film will be determined by the superposition of these waves. We denote the waves in the direction of incidence by the symbol $+$ (positive-going) and those in the opposite direction by $-$ (negative-going). This turns out to be very useful as the waves in the film can then be summed into one resultant positive-going wave and one resultant negative-going wave.

To apply the boundary conditions, we consider the tangential components of the fields. By neglecting the common phase factors, the resultants at the last interface, b , are:

$$\begin{aligned} E_b &= E_{1b}^+ + E_{1b}^- \\ H_b &= H_{1b}^+ + H_{1b}^- = \eta_1 E_{1b}^+ - \eta_1 E_{1b}^- \end{aligned}$$

With few simple calculations these rewrites as:

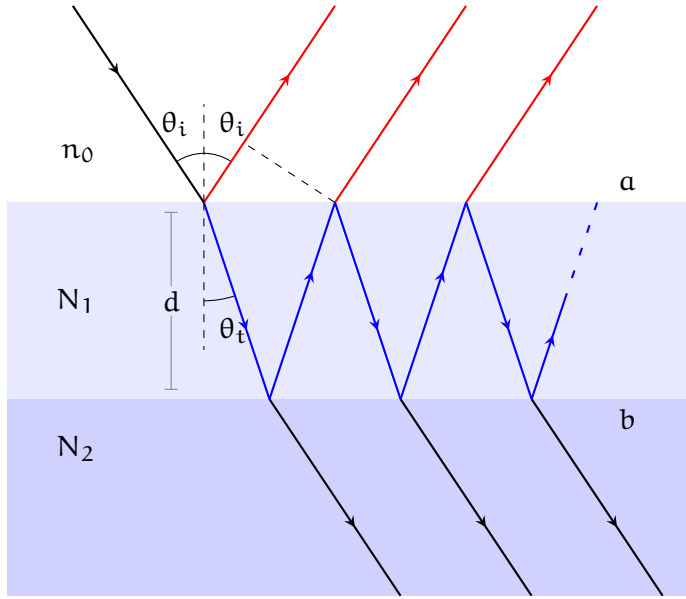


Figure 8: Thin film on a substrate.

$$\begin{aligned} E_{1b}^+ &= \frac{1}{2} \left(E_b + \frac{H_b}{\eta_1} \right) & H_{1b}^+ &= \frac{1}{2} (H_b + \eta_1 E_b) \\ E_{1b}^- &= \frac{1}{2} \left(E_b - \frac{H_b}{\eta_1} \right) & H_{1b}^- &= \frac{1}{2} (H_b - \eta_1 E_b) \end{aligned}$$

The fields at the first interface, a , at the same instant and at a point with identical x and y coordinates can be determined by applying a face shift δ in the z coordinate from 0 to $-d$, respectively:

$$\pm\delta = \pm K_1 \cdot \text{OPD} = \pm \frac{2\pi}{\lambda_0} N_1 \cdot (d \cos \theta_t) = \pm \frac{2\pi d N_1}{\lambda_0} \cos \theta_t \quad (130)$$

where the sign is $+$ for a positive-going wave (a forward propagating field accumulates a negative phase shift, thus we have to take a positive phase shift according to our reference system) and $-$ for a negative-going one. The values of E and H at the new interface are then:

$$\begin{aligned} E_{1a}^+ &= E_{1b}^+ e^{i\delta} = \frac{1}{2} \left(E_b + \frac{H_b}{\eta_1} \right) e^{i\delta} \\ E_{1a}^- &= E_{1b}^- e^{-i\delta} = \frac{1}{2} \left(E_b - \frac{H_b}{\eta_1} \right) e^{-i\delta} \\ H_{1a}^+ &= H_{1b}^+ e^{i\delta} = \frac{1}{2} (H_b + \eta_1 E_b) e^{i\delta} \\ H_{1a}^- &= H_{1b}^- e^{-i\delta} = \frac{1}{2} (H_b - \eta_1 E_b) e^{-i\delta} \end{aligned}$$

We can now compute the tangential components of E and H as:

$$\begin{aligned} E_a &= E_{1a}^+ + E_{1a}^- = E_b \left(\frac{e^{i\delta} + e^{-i\delta}}{2} \right) + \frac{H_b}{\eta_1} \left(\frac{e^{i\delta} - e^{-i\delta}}{2} \right) \\ &= E_b \cos \delta + H_b \frac{i \sin \delta}{\eta_1} \\ H_a &= H_{1a}^+ + H_{1a}^- = E_b \eta_1 \left(\frac{e^{i\delta} - e^{-i\delta}}{2} \right) + H_b \left(\frac{e^{i\delta} + e^{-i\delta}}{2} \right) \\ &= E_b i \eta_1 \sin \delta + H_b \cos \delta \end{aligned}$$

Using matrix notation we obtain:

$$\begin{bmatrix} E_a \\ H_a \end{bmatrix} = \begin{bmatrix} \cos \delta & \frac{i \sin \delta}{\eta_1} \\ i \eta_1 \sin \delta & \cos \delta \end{bmatrix} \begin{bmatrix} E_b \\ H_b \end{bmatrix} = M_1 \begin{bmatrix} E_b \\ H_b \end{bmatrix} \quad (131)$$

where $M_1^{2 \times 2}$ is the *characteristic matrix of the film*.

Since the tangential components of E and H must be continuous across the boundary, and since there is only a positive-going wave in the substrate, this relationship connects the tangential components of the fields at the incident interface (a) with those which are transmitted through the thin films until the final interface (b).

The normalized expression of (131) is obtained by dividing by E_b :

$$\begin{bmatrix} E_a/E_b \\ H_a/E_b \end{bmatrix} = \begin{bmatrix} \tilde{E} \\ \tilde{H} \end{bmatrix} = \begin{bmatrix} \cos \delta & \frac{i \sin \delta}{\eta_1} \\ i \eta_1 \sin \delta & \cos \delta \end{bmatrix} \begin{bmatrix} 1 \\ \eta_1 \end{bmatrix} \quad (132)$$

where \tilde{E} and \tilde{H} are the normalized electric and magnetic fields at the front of the interface. The matrix $[\tilde{E} \ \tilde{H}]^T$ is known as the *characteristic matrix of the assembly*.

3.4 ASSEMBLY OF THIN FILMS ON A SUBSTRATE

Let another film (N_2) to be added to the single film of the previous section so that the final interface is now denoted by c. The characteristic matrix of the film near the substrate is:

$$M_2 = \begin{bmatrix} \cos \delta_2 & \frac{i \sin \delta_2}{\eta_2} \\ i \eta_2 \sin \delta_2 & \cos \delta_2 \end{bmatrix}$$

and from equation (131):

$$\begin{bmatrix} E_b \\ H_b \end{bmatrix} = M_2 \begin{bmatrix} E_c \\ H_c \end{bmatrix} \quad (133)$$

We can then apply the same procedure recursively to give the parameters at the initial interface:

$$\begin{bmatrix} E_a \\ H_a \end{bmatrix} = M_1 \begin{bmatrix} E_b \\ H_b \end{bmatrix} = M_1 M_2 \begin{bmatrix} E_c \\ H_c \end{bmatrix}$$

It is now straightforward to see that this result can be extended to the general case of an assembly of q layers, where the characteristic matrix of the assembly M is simply the product of the individual matrices:

$$M = \prod_{k=1}^q \begin{bmatrix} \cos \delta_k & \frac{i \sin \delta_k}{\eta_k} \\ i\eta_k \sin \delta_k & \cos \delta_k \end{bmatrix} \quad (134)$$

and where the tilted optical admittance is that computed in the previous sections:

$$\eta_k = \begin{cases} y_0 N_k \cos \theta_k & \text{for s-polarization} \\ y_0 N_k / \cos \theta_k & \text{for p-polarization} \end{cases}$$

In case of δ_k , it avoids difficulties over signs and quadrants if, in the case of absorbing media, the arrangement used for computing phase thicknesses and admittance is:

$$\delta_k = \frac{2\pi}{\lambda_0} d_k \sqrt{n_k^2 - \beta_k^2 - n_0^2 \sin^2 \theta_i - 2in_k \beta_k} \quad (135)$$

the correct solution being in the fourth quadrant. Then we obtain:

$$\eta_{k,s} = y_0 \sqrt{n_k^2 - \beta_k^2 - n_0^2 \sin^2 \theta_i - 2in_k \beta_k} \quad (136)$$

and, consequently:

$$\eta_{k,p} = \frac{y_k^2}{\eta_{k,s}} = \frac{y_0^2 N_k^2}{\eta_{k,s}} \quad (137)$$

The normalized electric and magnetic fields follows:

$$\begin{bmatrix} \tilde{E} \\ \tilde{H} \end{bmatrix} = M \begin{bmatrix} 1 \\ \eta_m \end{bmatrix} \quad (138)$$

where we have now used the suffix m to denote the substrate. A useful property of the characteristic matrix of thin film is that the determinant is unity. As a consequence, also the determinant of a product of any number of this matrices must also be unity.

3.5 REFLECTANCE, TRANSMITTANCE AND ABSORBANCE

We define the *input optical admittance* of the assembly in analogy with equation (115), that is $Y = \frac{H_a}{E_a}$. Taking advantage of the characteristic matrix of an assembly of films we can write:

$$Y = \frac{H_a/E_b}{E_a/E_b} = \frac{\tilde{H}}{\tilde{E}} \quad (139)$$

In this way, using previous results, we can compute the reflection coefficient and the reflectance of the multilayer as:

$$\rho = \frac{\eta_0 - Y}{\eta_0 + Y} \quad (140)$$

$$R = \left(\frac{\eta_0 - Y}{\eta_0 + Y} \right) \left(\frac{\eta_0 - Y}{\eta_0 + Y} \right)^* \quad (141)$$

In addition, enough information is included in equation (138) to allow the transmittance and absorbance of a thin-film assembly to be calculated. For this to have a physical meaning we require the incident medium to be transparent, that is, η_0 to be real.

First of all, we calculate the net irradiance at the exit side of the assembly, which we take as the k -th interface: This is given by:

$$I_k = \frac{1}{2} \Re[E_k H_k^*] = \frac{1}{2} \Re[E_k \eta_m^* E_k^*] = \frac{1}{2} \Re[\eta_m] |E_k|^2 \quad (142)$$

where, once again, we consider the component of irradiance normal to the interfaces. Given the normalized fields \tilde{E} and \tilde{H} , the net irradiance at the input of the assembly is:

$$I_a = \frac{1}{2} \Re[\tilde{E} \tilde{H}^*] |E_k|^2 \quad (143)$$

Let the incident irradiance be denoted by I_i , then equation (143) represents the irradiance actually entering the assembly, which is $(1 - R)I_i$:

$$(1 - R)I_i = \frac{1}{2} \Re[\tilde{E} \tilde{H}^*] |E_k|^2$$

$$I_i = \frac{\Re[\tilde{E} \tilde{H}^*] |E_k|^2}{2(1 - R)}$$

Equation (142) represents the irradiance leaving the assembly and entering the substrate, which is by definition the transmittance (of the assembly itself):

$$T = \frac{I_k}{I_i} = \frac{\Re[\eta_m](1 - R)}{\Re[\tilde{E} \tilde{H}^*]} \quad (144)$$

The absorbance A in the multilayer is connected with R and T by the relationship:

$$R + T + A = 1 \quad (145)$$

so that

$$A = 1 - R - T = (1 - R) \left(1 - \frac{\Re[\eta_m]}{\Re[\tilde{E}\tilde{H}^*]} \right) \quad (146)$$

In absence of absorption in any of the layers it can readily be shown that the above expressions are consistent with $A = 0$ and $T + R = 1$. Since the individual film matrices will have determinants of unity, indeed, the characteristic matrix of the assembly will also have the determinant of unity with:

$$|M| = \begin{vmatrix} M_{11} & iM_{12} \\ iM_{21} & M_{22} \end{vmatrix} = M_{11}M_{22} + M_{12}M_{21} = 1$$

where M_{11}, M_{12}, M_{21} and M_{22} are all real quantities. Then we can use equation (138) to obtain:

$$\begin{bmatrix} \tilde{E} \\ \tilde{H} \end{bmatrix} = \begin{bmatrix} M_{11} & iM_{12} \\ iM_{21} & M_{22} \end{bmatrix} \begin{bmatrix} 1 \\ \eta_m \end{bmatrix} = \begin{bmatrix} M_{11} + iM_{12}\eta_m \\ M_{22}\eta_m + iM_{21} \end{bmatrix}$$

and finally compute:

$$\begin{aligned} \Re[\tilde{E}\tilde{H}^*] &= \Re[(M_{11} + iM_{12}\eta_m)(M_{22}\eta_m - iM_{21})] \\ &= (M_{11}M_{22} + M_{12}M_{21})\Re[\eta_m] \\ &= \Re[\eta_m] \end{aligned} \quad (147)$$

Substituting (147) in (146) we find $R + T = 1$ as expected.

In conclusion, we can manipulate equations (141), (144) and (146) into slightly better forms. From (139) and (141):

$$R = \left(\frac{\eta_0 \tilde{E} - \tilde{H}}{\eta_0 \tilde{E} + \tilde{H}} \right) \left(\frac{\eta_0 \tilde{E} - \tilde{H}}{\eta_0 \tilde{E} + \tilde{H}} \right)^* \quad (148)$$

so that

$$1 - R = \frac{2\eta_0(\tilde{E}\tilde{H}^* + \tilde{E}^*\tilde{H})}{(\eta_0\tilde{E} + \tilde{H})(\eta_0\tilde{E} + \tilde{H})^*} \quad (149)$$

Substituting this result into equation (144) we obtain:

$$T = \frac{4\eta_0 \Re[\eta_m]}{(\eta_0 \tilde{E} + \tilde{H})(\eta_0 \tilde{E} + \tilde{H})^*} \quad (150)$$

and

$$A = \frac{4\eta_0 \Re[\tilde{E} \tilde{H}^* - \eta_m]}{(\eta_0 \tilde{E} + \tilde{H})(\eta_0 \tilde{E} + \tilde{H})^*} \quad (151)$$

Equations (148), (150) and (151) are the most useful forms for the expression of R, T and A.

3.6 POTENTIAL TRANSMITTANCE

The last parameter we must take into consideration in this chapter is the *potential transmittance*. Given a multilayer structure, the potential transmittance is defined as the ratio of the irradiance leaving the exit interface to that entering by the front interface:

$$\psi = \frac{I_{\text{exit}}}{I_{\text{enter}}} = \frac{T}{1-R} \quad (152)$$

or, equivalently, the ratio between the irradiance leaving the assembly and the net irradiance actually entering. For the entire system, the net irradiance actually entering is the difference between the incident and reflected irradiances.

The potential transmittance of a series of sub-assemblies of layers is simply the product of the individual potential transmittances. For example, in the case of three sub-assemblies with interfaces a,b,c and d, we can write:

$$\psi = \frac{I_e}{I_i} = \frac{I_b}{I_a} \frac{I_c}{I_b} \frac{I_d}{I_c} \quad (153)$$

The potential transmittance is fixed by the parameters of the constituent layers and by the characteristics of the structure at the exit interface, and it represents the transmittance which this particular combination would give if there were no reflection losses. Because of that it provides a measure of the maximum transmittance which could be expected from the arrangement.

By definition, it is unaffected by any transparent structure deposited over the front surface - which can affect the transmittance as distinct from the potential transmittance - and to ensure that the transmittance is equal to the potential transmittance the layers added to the front surface must maximise the irradiance actually entering the assembly. This implies reducing the reflectance of the complete assembly to zero or, in other words, adding an antireflection coating. The

potential transmittance, however, is affected by any changes in the structure at the exit interface and it is possible to maximise the potential transmittance of a sub-assembly in this way.

We now show that the parameters of the layer, or sub-assembly of layers, together with the optical admittance at the rear surface, are sufficient to define the potential transmittance. Let the complete multilayer performance be given by:

$$\begin{bmatrix} \tilde{E} \\ \tilde{H} \end{bmatrix} = M_1 M_2 M_3 \cdots M_a M_b M_c \cdots M_n \begin{bmatrix} 1 \\ \eta_m \end{bmatrix}$$

where we want to calculate the potential transmittance of the sub-assembly $M_a M_b M_c$. Let the product of the matrices to the right of the sub-assembly be given by

$$\begin{bmatrix} \tilde{E}_e \\ \tilde{H}_e \end{bmatrix}$$

Now, if we denote:

$$\begin{bmatrix} \tilde{E}_i \\ \tilde{H}_i \end{bmatrix} = M_a M_b M_c \begin{bmatrix} \tilde{E}_e \\ \tilde{H}_e \end{bmatrix} \quad (154)$$

then:

$$\psi = \frac{\Re[\tilde{E}_e \tilde{H}_e^*]}{\Re[\tilde{E}_i \tilde{H}_i^*]} \quad (155)$$

By dividing equation (154) by \tilde{E}_e we obtain:

$$\begin{bmatrix} \tilde{E}'_i \\ \tilde{H}'_i \end{bmatrix} = M_a M_b M_c \begin{bmatrix} 1 \\ Y_e \end{bmatrix}$$

where $Y_e = \tilde{H}_e / \tilde{E}_e$, $\tilde{E}'_i = \tilde{E}_i / \tilde{E}_e$ and $\tilde{H}'_i = \tilde{H}_i / \tilde{E}_e$. The potential transmittance is:

$$\begin{aligned} \psi &= \frac{\Re[Y_e]}{\Re[\tilde{E}'_i \tilde{H}'_i^*]} = \frac{\Re[\tilde{H}_e / \tilde{E}_e]}{\Re[(\tilde{E}_i / \tilde{E}_e)(\tilde{H}_i^* / \tilde{E}_e^*)]} \\ &= \frac{\tilde{E}_e \tilde{E}_e^* \Re[\tilde{H}_e / \tilde{E}_e]}{\Re[\tilde{E}_i \tilde{H}_i^*]} = \frac{\Re[\tilde{E}_e^* \tilde{H}_e]}{\Re[\tilde{E}_i \tilde{H}_i^*]} \\ &= \frac{\Re[\tilde{E}_e \tilde{H}_e^*]}{\Re[\tilde{E}_i \tilde{H}_i^*]} \end{aligned} \quad (156)$$

which is identical to equation (155). Thus the potential transmittance of any sub-assembly is determined solely by the characteristics of the layer or layers of the sub-assembly together with the optical admittance of the structure at the exit interface.

MODELLING

Contents

4.1	Damage Model	42
4.1.1	Example 1: No degradation	42
4.1.2	Example 2: Drop in efficiency	42
4.1.3	Example 3: Delamination	43
4.2	Predictive Model	44
4.2.1	Optical properties of materials	45
4.2.2	Matrix model for R and T calculation	45
4.2.3	Implanted particles profile	46
4.2.4	Matrix model modification for R and T calculation (irradiated coating)	47
4.3	Software Architecture	48
4.3.1	Class objects description	48
4.4	Software User Manual	51

The damage effects on coatings and their substrates depend on the ion species, their energy, the flux and the total fluence (dose) [12]. Once these parameters are defined, laboratory tests can be used to qualify the components. In particular, particles accelerators are commonly used to irradiate such components. Although valuable experiments on the interaction of ions with glasses and coatings have been carried out, these last are not always systematic: in particular, studies on coatings are limited to specific values of energy and dose of selected ions species and they generally have the character of a qualification of a specific component with respect to its particular space operational environment. Some scientific information come from experiments carried out in other disciplines, such as plasma and matter physics [13]-[15], even though the ion irradiation parameters do not correspond to those in space. Therefore, a systematic study on the effects of ions in optical materials and coatings for space application is needed.

For this reason, in this project different types of simple coatings (monolayer and bi-layers) comprising different materials (Al, Au, SiO₂, TiO₂ etc.) will be experimentally irradiated with different ions species (proton, electrons, He+) at various energies and fluences (doses) in order to experimentally study the degradation on their optical, structural and morphological properties.

4.1 DAMAGE MODEL

When a coating of a given material and thickness is irradiated by an ion beam of a selected specie and energy, three situations can occur:

1. the sample is fully passed through and no ion is implanted;
2. the sample is fully implanted (i.e. all the ions stop inside the material);
3. A third situation foresees a partial implantation.

The implantation profile of the particles can be simulated using the TRIM/SRIM software [16]. As an example, in Figure. [9] the implantation profile of 1 keV and 40 keV protons in an Au film is reported. Notice that, depending on the energy of the implanted particles, the implantation profile distributes over different film depths.

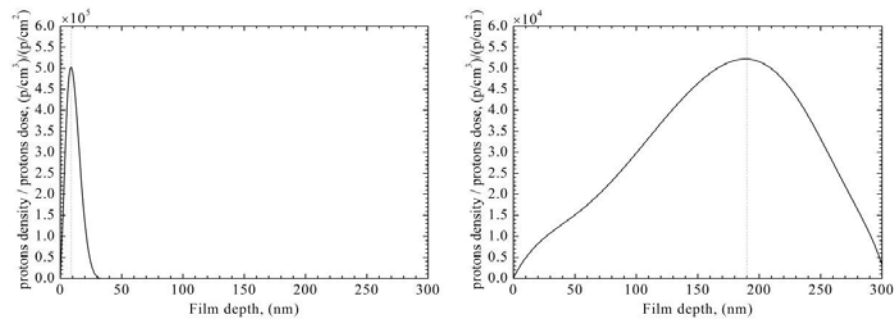


Figure 9: 1keV (left) and 40 keV (right) protons distribution inside 300 nm gold layer

Previous studies with protons having energies 1-100 keV range have demonstrated that implantation into materials for space application can cause refraction index changes [17], delamination [18], surface nanobubbles formation and blistering [6]. Regarding He irradiation to simulate space conditions, the literature is rather limited [19]. Examples are here reported.

4.1.1 Example 1: No degradation

A single layer of Au irradiated with 3 MeV protons of flux $6.5 \cdot 10^{11}$ [cm^2/s] and fluence 10^{14} [cm^{-2}] shows no variations in reflectance (Figure [10])

4.1.2 Example 2: Drop in efficiency

The same Au sample irradiated with different parameters (Table [1]) shows a drop in efficiency (reflectance). This drop depends on fluence

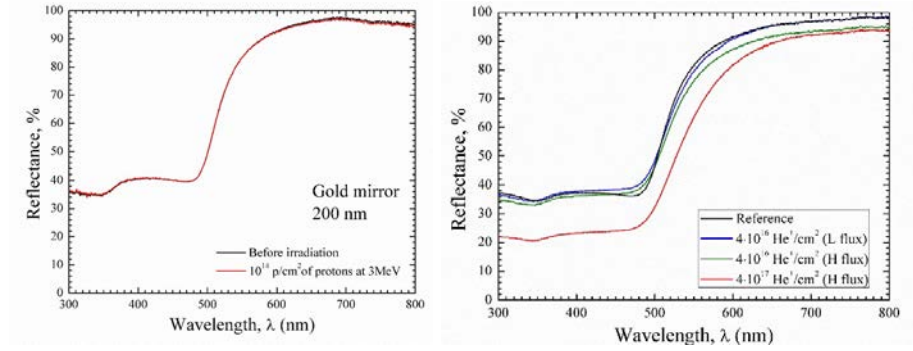


Figure 10: No degradation (left) and drop in efficiency (right) examples [12].

and flux values and is associated with a degradation of the surface morphology (Figure [10]).

	Flux [cm^2/s]	Fluence [cm^{-2}]
H	$1.6 \cdot 10^{13}$	$4 \cdot 10^{16}$
L	$1.6 \cdot 10^{12}$	$4 \cdot 10^{17}$

Table 1: Parameters of 4 KeV He⁺ irradiation for example 2.

4.1.3 Example 3: Delamination

Delamination of the coatings is observed (Figure [11]) at the interface corresponding to the peak of the implantation profile, probably due to bubbles accumulation. In general, inter-diffusion of atoms at interfaces must be expected due to scattering with incident particles. In case of electrons, the potential optical performance degradations occurring on coatings can be due to many physical processes, including local thermal release, surface micro-protrusions and activation of color centres, which correspond to changes in morphology and refraction index of materials. Based on the presented results we can define a first list of potential damages induced by protons, electrons and He⁺:

1. Surface morphology changes;
2. Refraction index changes;
3. Structural changes as:
 - a) Inter-diffusion at interfaces;
 - b) Delamination.

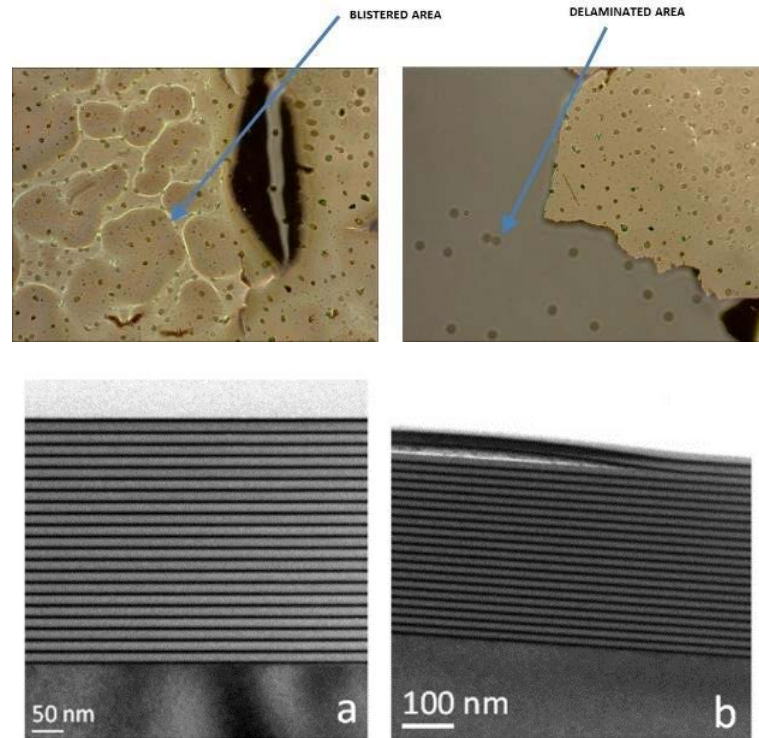


Figure 11: Degradation example. Irradiation with 50 keV He⁺ on Al/SiO₂ (Optical Microscope image, top) and with 1 keV protons on Mo/Si (Transmission Electron Microscope image, bottom). The images to the right shows the effects observed after irradiation.

4.2 PREDICTIVE MODEL

A mathematical model was developed to predict the coatings behaviour under different irradiation conditions. Such model takes into consideration all the damages listed by combining them using weighting factors which depend on experimental outcomes. Damages 1, 2 and 3-a) affect the efficiency of the coatings, while 3-b) is considered a fatal damage.

In case of ions, the Predictive Model is based on a combination of simulations and experimental outcomes, while in case of electrons it is based on experimental outcomes only. The Predictive Model logical flow is reported in Figure. [12]. Within the project, I had the opportunity to refine the code in terms of debug and optimization, and I was directly responsible for the design of the software interface.

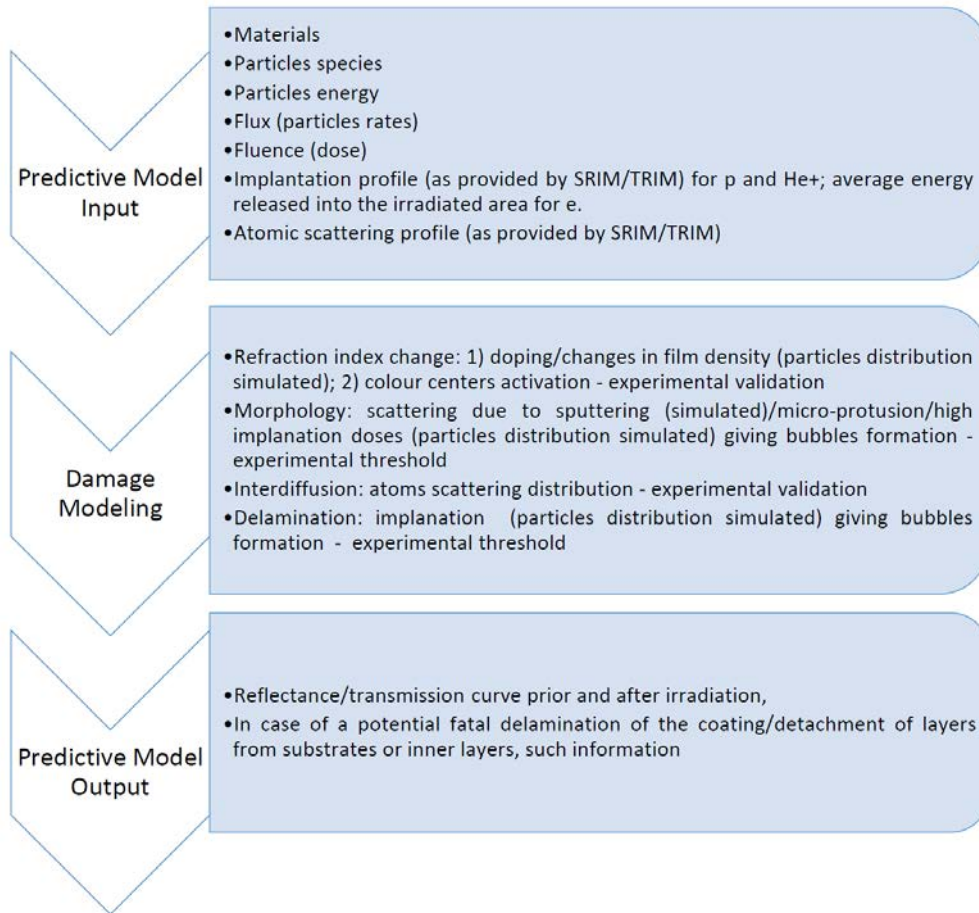


Figure 12: Logical workflow of the Predictive Model.

4.2.1 *Optical properties of materials*

Currently, the following materials are available in the software: SiO₂, TiO₂, ZrO₂, MgF₂, Au, Al, Pd, Pt, Ag, SiO₂ (fused silica). For each of these the software is provided with the optical constants (n and β) and with others useful parameters such as density (ρ) and molar mass (M).

4.2.2 *Matrix model for R and T calculation*

The optical behaviour of a coating deposited on a substrate (reflectance, transmittance) is calculated by using the transfer matrix method which is computationally fast and easy to implement. The mathematical details of this method are exhaustively described in previous chapters, so that only the most important results are here reported.

Given a coating of N layers deposited on a substrate, its optical prop-

erties can be computed by using the characteristic matrix of the structure:

$$M = \prod_{k=1}^N M_k = \prod_{k=1}^N \begin{bmatrix} \cos \delta_k & \frac{i \sin \delta_k}{\eta_k} \\ i\eta_k \sin \delta_k & \cos \delta_k \end{bmatrix} \quad (157)$$

where the two quantities δ_k and η_k depend on the angle of incidence of light with respect to the normal incidence (θ_i), the refractive index of the first medium (hereafter called environment, n_0 , and assumed to be lossless), the complex optical constant N_k and the thickness d_k of the layer. In particular, δ_k takes into account the phase delay induced by the layer and it is expressed as:

$$\delta_k = \frac{2\pi}{\lambda_0} d_k \sqrt{n_k^2 - \beta_k^2 - n_0^2 \sin^2 \theta_i - 2in_k \beta_k} \quad (158)$$

while η_k is linked to the electric field amplitude of the beam reflected/transmitted by the layer and it changes with the polarization orientation:

$$\eta_k = \begin{cases} y_0 \sqrt{n_k^2 - \beta_k^2 - n_0^2 \sin^2 \theta_i - 2in_k \beta_k} & \text{for s-polarization} \\ \frac{y_0^2 N_k^2}{\eta_{k,s}} & \text{for p-polarization} \end{cases} \quad (159)$$

Once the equivalent matrix of the whole coating is known, its reflectance R_{coat} and transmittance T_{coat} can be easily computed. Note that T_{coat} is the coating transmittance considering a semi-infinite substrate. In order to properly simulate the transmittance of a real component, the effect of the second interface of the substrate (which is considered uncoated) has to be taken into account. Calling R_{coat} the reflectance of a single surface of the uncoated substrate, the total transmittance is given by:

$$T = \frac{T_{\text{coat}}(1 - R_{\text{coat}})}{1 - (R_{\text{coat}}R_{\text{sub}}^2)} \quad (160)$$

4.2.3 Implanted particles profile

Simulations of the Stopping Range and collision dynamics of protons and He are performed with TRIM(TREnds & Indices for Monitoring data)/SRIM(Stopping and Range of Ions in Matter) software. The software performs Montecarlo simulations of elastic scattering interactions between the incident ions and the target atoms and provides the profile of the implanted atoms, the damage depth distributions, as well as the amount of surface sputtering. A typical output is shown in Figure [13], where the He ions distribution in a gold (Au) film is simulated for different energy values [12].

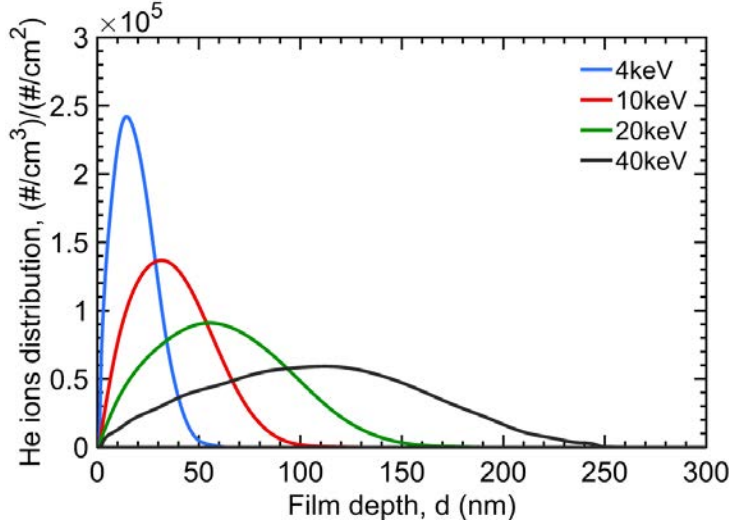


Figure 13: Distribution of He+ ions implanted in gold (density of 19.3 [g/cm³]) as simulated by TRIM [12].

4.2.4 Matrix model modification for R and T calculation (irradiated coating)

The irradiated coating is modelled by the *effective medium approximation* (EMA) [20][12]. The effects produced by the vacancies and inclusions can be suitably modelled considering that they induced a change of the complex dielectric function of the material medium which depends on the fractional volume v_f :

$$v_f = \frac{\rho_p}{\rho_m} \quad (161)$$

where ρ_p is the density of the vacancies and inclusions and ρ_m is the density of atoms in the considered film. In particular, if the v_f is sufficiently small (i.e. $v_f < 0.2$), the changes in the optical constants can be modelled by using the *Maxwell-Garnett* (MG) formula which allows the calculation of the effective dielectric function ϵ_f of the intermixed system corresponding to the implanted film volume. According to the MG formula, the effective dielectric function, ϵ_f , depends on the matrix medium, ϵ_m , the dielectric function of the inclusions, ϵ_p , and the volume fraction v_f of the inclusions with respect to the matrix medium:

$$\epsilon_f = \frac{2(1 - v_f)\epsilon_m + (1 + 2v_f)\epsilon_p}{(2 + v_f)\epsilon_m + (1 - v_f)\epsilon_p} \quad (162)$$

The fractional volume v_f changes with the depth of the film proportionally to the implantation profile; correspondingly, the irradiated region of the film is characterized by a complex dielectric function

which varies continually in depth. In this case, the reflectance/transmittance of the coating can be computed by using the standard transfer matrix formalism by discretizing into layers the irradiated area and assuming each one as characterized by its local average fractional volume $v_f(d) = W(d)\tilde{v}_f$, where $W(d)$ is the normalized depth profile and \tilde{v}_f is the maximum fraction volume of the distribution (Figure [14]).

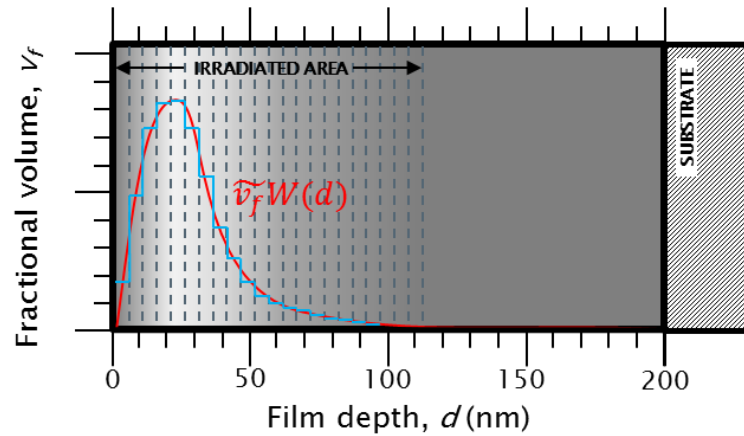


Figure 14: Sketch of the irradiated films area discretized in layers with the superimposition of the fractional volume distributions adopted for the reflectance computation [12].

4.3 SOFTWARE ARCHITECTURE

The architecture of the software is shown in Figure [15].

4.3.1 Class objects description

4.3.1.1 The class "layer"

The class "layer" describes the behavior of a single layer. It requires the following parameters:

1. *thickness*: it specifies the thickness in nm of the layer (positive real number);
2. *material*: it specifies the material constituting the layer (string indicating the name of the material file where the optical constants, the density and the molar mass are stored);

The object has only the method

```
1 function M=get_matrix(n_0, theta_0)
```

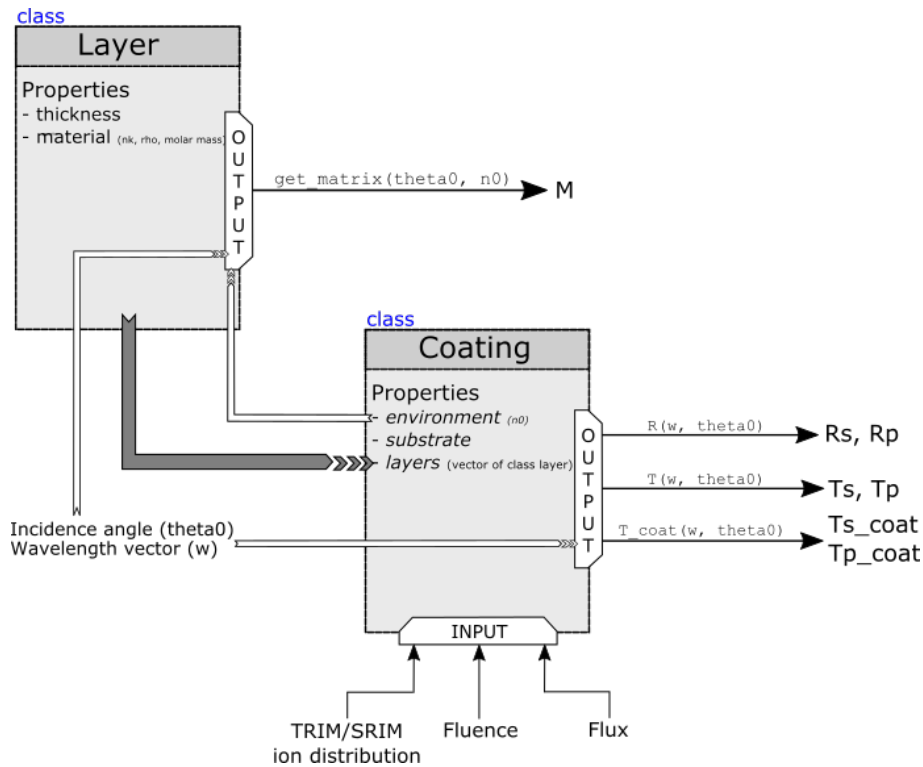


Figure 15: Predictive Model Software Architecture.

which returns the transfer matrix of the layer reported in equation (157); in addition to the parameters used to define the object, the method needs the optical constants of the environment n_0 and the incidence angle θ_0 .

4.3.1.2 The subclass of class "layer"

The object-oriented approach allows to define classes that implement the behaviour of a layer but with more properties (and methods) with respect to the simple class layer. Every layer subclass has to report in the material property the string "special". The subclass `layer_EMA` implements a *Maxwell-Garnet* effective medium approximation for modelling a layer in which inclusions of a different material have been added. The subclass has the constructor

```
1 function obj = layer_EMA (d, mat1, mat2, vf)
```

where d is the thickness, `mat1` is the principal material, `mat2` is the material of the inclusions and `vf` is the fractional volume of these inclusions.

4.3.1.3 The class "coating"

The class "coating" models the optical behaviour of the real coating. It requires the following parameters:

- *substrate*: it specifies the material of the substrate (SiO₂, Si, BK7, etc.); it is a string indicating the name of the material file where the optical constants, the density and the molar mass are stored;
- *environment*: it specifies the material of the environment (Vacuum, air, water, etc.); it is a string indicating the name of the material file where the optical constants, the density and the molar mass are stored;
- *layers*: it is a vector of objects “*layer*” which compose the multi-layer film.

With these properties, the coating is fully defined. The following list reports the methods of this class:

- *R*: compute the reflectance for the wavelength reported in the vector w considering the incidence angle θ_0 . Thus, this method retrieves the characteristic matrix of the structure and then computes the reflectance R_s and R_p .

```
1 function [Rs, Rp]=R(w, theta0)
```

- *T_coat*: compute the transmittance (considering a coating semi-infinite substrate) for the wavelength reported in the vector w considering the incidence angle θ_0 . Thus, this method retrieves the characteristic matrix of the structure then computes the reflectance T_s and T_p .

```
1 function [Ts, Tp]=T_coat(w, theta0)
```

- *T*: compute the transmittance (considering a coating semi-infinite substrate) for the wavelength reported in the vector w considering the incidence angle θ_0 . Thus, this method retrieves the characteristic matrix of the structure and then computes the reflectance T_s and T_p .

```
1 function [Ts, Tp]=T (w, theta0)
```

- *irradiate*: this method applies to the topmost layers of the coatings the Maxwell-Garnet approximation by following the input implanted ion distribution and discretizing such layers for the number given in input. The irradiated coating is defined as new object.

```
1 function [A, vf]=irradiate(dist, N, mat)
```

where *dist* (vector with 2 columns, the first is the depth, the second is the distribution) is the fractional volume distribution of the inclusions, *mat* (string) specifies the materials of the inclusions and *N* (positive integer) is the number of layers after the discretization.

4.4 SOFTWARE USER MANUAL

The software is designed to be as intuitive as possible. An overview on the App is given in Figure [16].

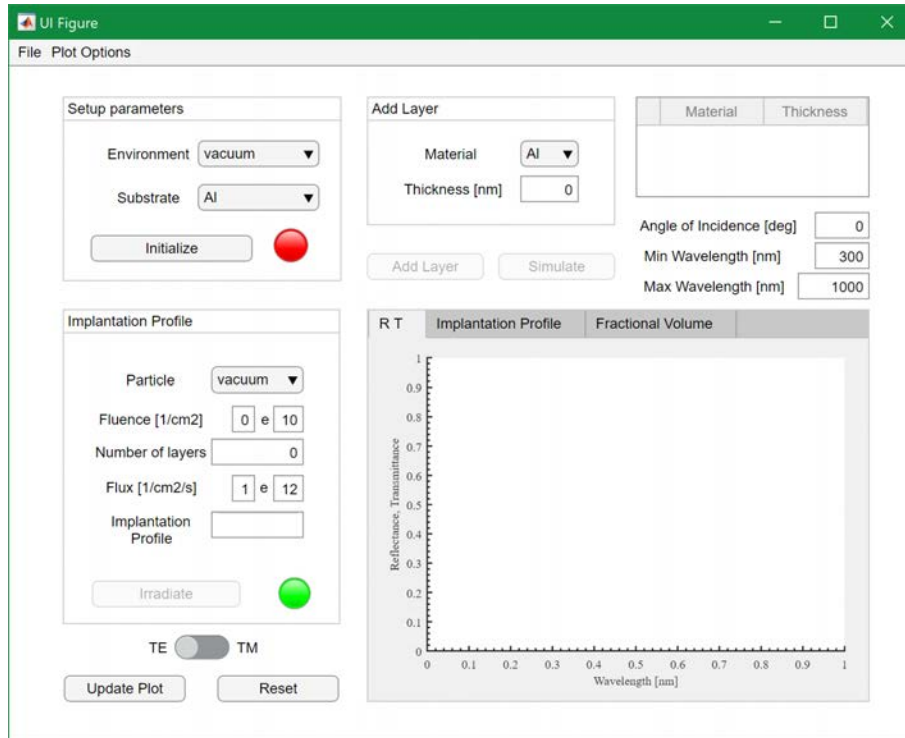
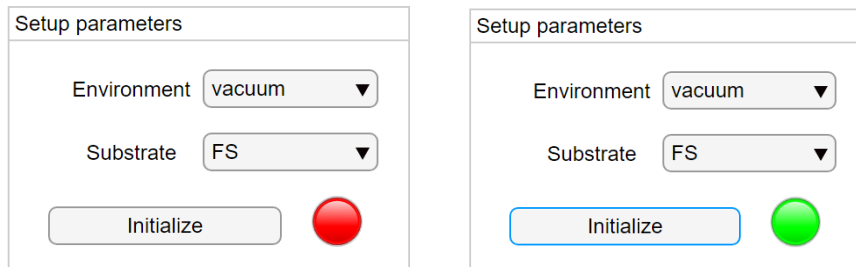


Figure 16: Predictive Model Software App.

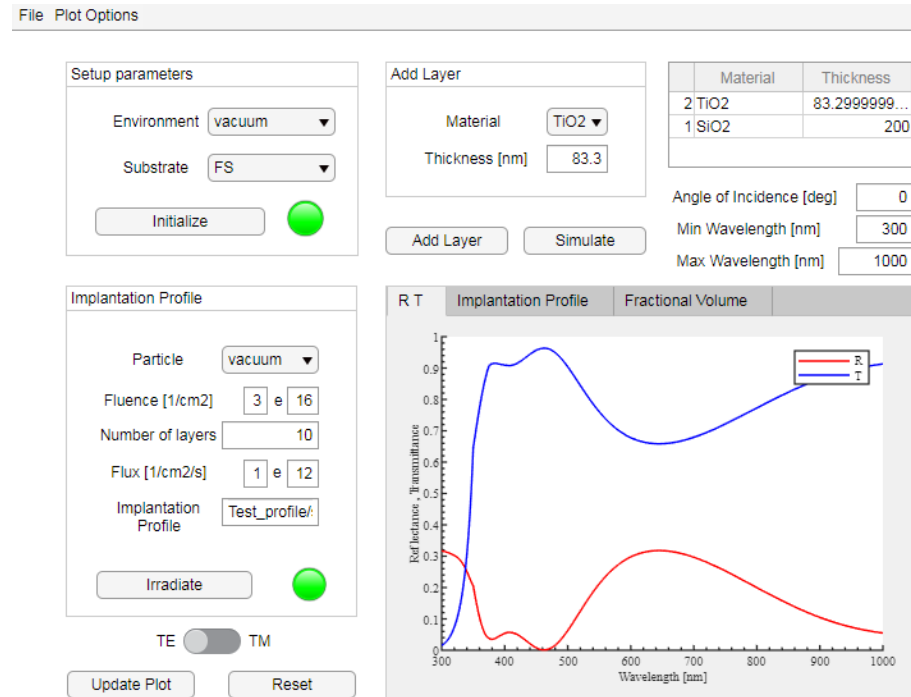
To start the simulation, the user is required to specify the *Environment* and the *Substrate material*. A list of materials is specified by the app. Before the initializations, the other three main functions *Add Layer*, *Simulate* and *Update Plot* are disabled. These unlocks when the *Initialize* button is pushed. Once the button is pushed, the red lamp on the right turns into green colour confirming the operation has completed correctly:



The user can specify the structure of the sample to be analysed by adding layers of different materials and thicknesses. These are reported in the right table where the bottom layer, the one on the top

of the substrate, is indicated as layer 1.

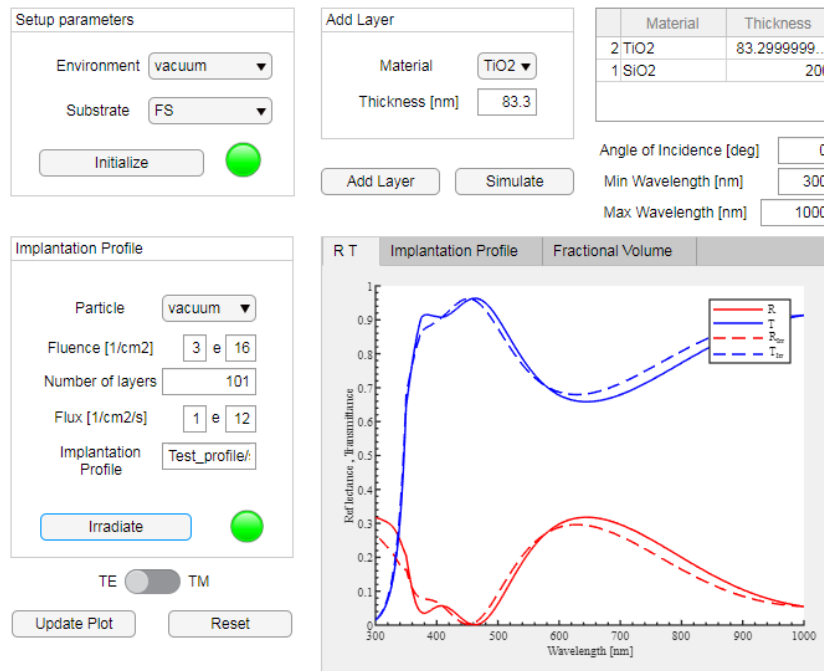
To start the simulation, the user is required to push the *Simulate* button. The program computes the Reflectance and Transmittance curves at the specified angle of incidence and plots them as function of the wavelength. The wavelength range can be modified in the corresponding fields:



To see the variations in Reflectance and Transmittance curves after the implantation profile, the software requires to specify five parameters:

1. the *type of particle* (incident ions): at the moment this function only allows to select vacuum, but it will be implemented soon to offer a wider choice;
2. the *Fluence*;
3. the *number of layers* in which the film has to be discretized (default value corresponds to the number of layers);
4. the *Flux*: this value must be lower than or equal to the default value $1 \cdot 10^{12}$ [$1/\text{cm}^2/\text{s}$] in order to guarantee reliable results. For this reason, if the input value is lower, the lamp next to the *Irradiate* button turns into red colour as a warning signal;
5. the *Implantation Profile*: this must be specified by copying the file's directory in the corresponding Edit Text Field.

After the *Irradiate* button is pushed, both curves are plotted in the corresponding area, as well as the Implantation profile and the fractional volume. These can be easily selected in the Menu Bar:



Other functions included are:

- *Update plot*: Update the plot;
- *Reset*: Bring the software to initial condition;
- *TE/TM*: Specify if plotted curves refers to p- or s- polarization;
- *Export*: is it possible to export a number of different results using the export functions from the File option in the Menu Bar. The selected data will appear in MATLAB's Workspace. NB: Reflectance and Transmittance curves are exported accordingly to the specified polarization (TE/TM).

EXPERIMENTAL

Contents

5.1	Spectrometers	57
5.1.1	Cary 5000	57
5.1.2	Cary 630 FTIR	60
5.2	Optical Coatings	61
5.3	Samples Characterization	62
5.4	Simulation and Fitting	78

All samples have been characterized using a double grating spectrophotometer Cary 5000 in transmittance or (absolute) reflectance respectively. In order to be able to repeat the measurements with the same conditions after the irradiation process, samples have been positioned taking notes on both the illuminated face and the orientation. The wavelength range is 200-2500 nm. In case of Au samples, the range has been extended up to 15000 nm using a Cary 630 FTIR spectrometer.

5.1 SPECTROMETERS

5.1.1 *Cary 5000*

Cary 5000 by Agilent [21] is a double grating spectrometer that is able to perform different spectroscopic measurements in the UV-VIS-NIR spectrum range. For our purpose, we used two different setup to characterize each sample either in transmittance or reflectance respectively. In particular, for the last one, measurements were performed by employing a VW-scheme which allows to obtain the absolute reflectance with an incidence angle of 7° and an accuracy better than 2%. A picture of the device is shown in Figure [17].

A schematic representation of the Cary 5000 spectrometer is given in Figure [18]. As previously mentioned, it performs measurements at different wavelengths by exploiting two different diffraction gratings.



Figure 17: Cary 5000 spectrometer.

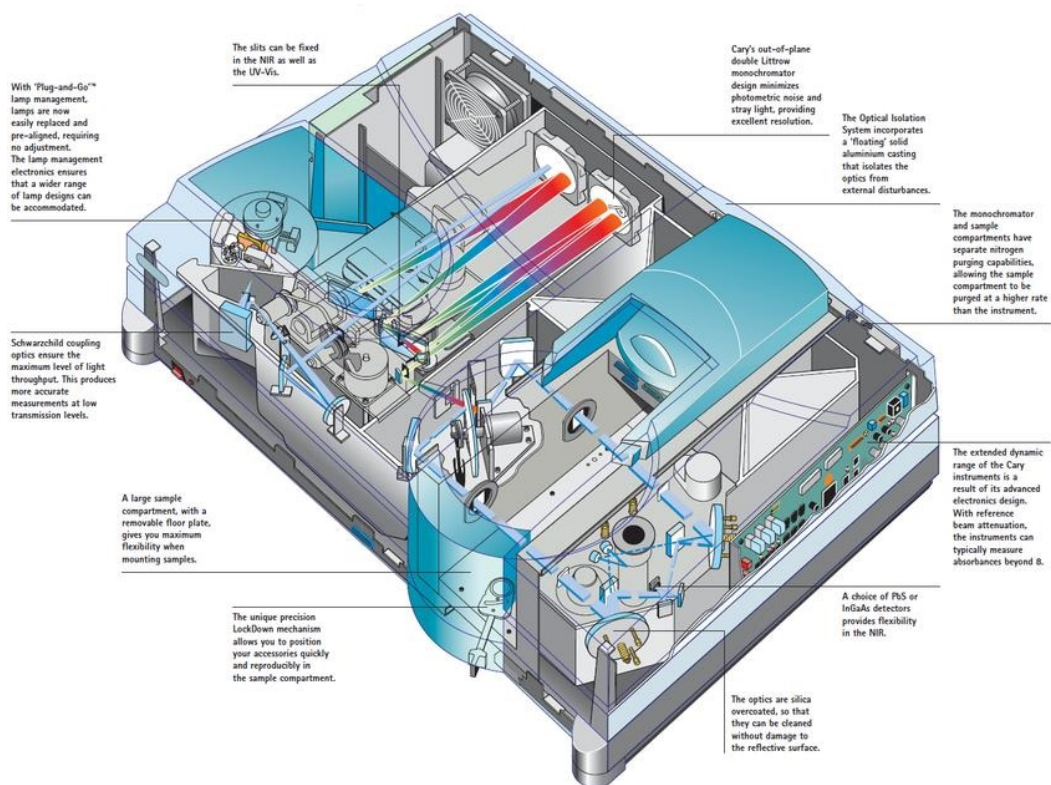


Figure 18: Schematic representation of Cary 5000 spectrometer.

The VW accessory

The VW SRA (specular reflectance accessory) is designed to measure the direct (specular) reflectance of light from smooth solid materials at near normal incidence. The term "VW" describes the light path through the accessory in the reference and measurement positions. The VW design features a kinematically mounted spherical mirror, which is used for both calibration and sample measurement. With the exception of the sample, the same optical elements are always in the light path, providing a truly absolute reflectance measurement. Absolute measurements remove any need to correct results against standard reference materials.

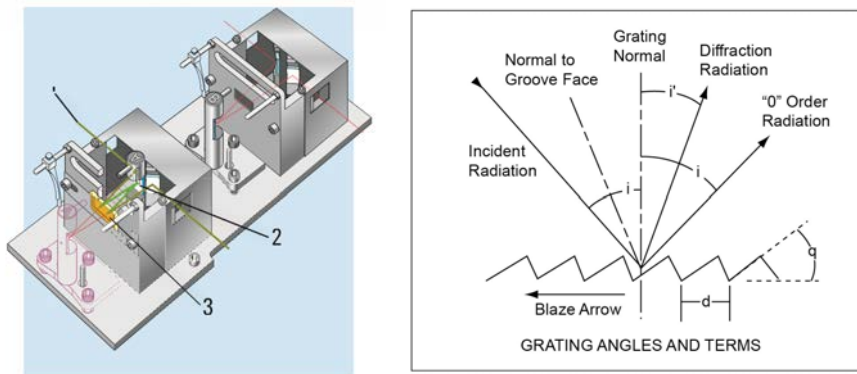


Figure 19: The VW SRA by Agilent (left) and a schematic representation of a (blazed) diffraction grating used in reflection.

Diffraction grating principle

In optics, a diffraction grating is an optical component with a periodic structure that splits and diffracts light into several beams travelling in different angular directions. It can reflect or transmit the light and is an essential part of a monochromator. Monochromators are, in turn, optical devices that work as narrowband wavelength filters with mechanically adjustable transmission wavelength.

5.1.2 Cary 630 FTIR

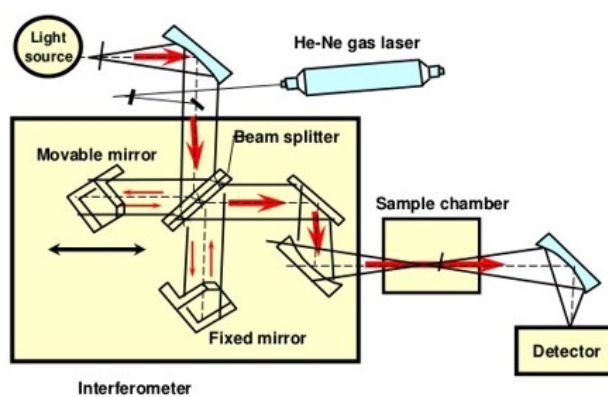
The second spectrometer is based on a total different technique, that is *Fourier-Transform infrared spectroscopy*.



Figure 20: Cary 630 FTIR spectrometer.

This technique is commonly used to obtain the (infrared) spectrum of absorption or emission of a solid, liquid or gas. A FTIR spectrometer simultaneously collects high-spectral-resolution data over a wide spectral range. This confers a significant advantage over a dispersive spectrometer (monochromator), which measures intensity over a narrow range of wavelengths at a time.

The term Fourier-transform infrared spectroscopy originates from the fact that a Fourier transform (FFT) is required to convert the collected interferogram into the actual spectrum.



22

Figure 21: Schematic representation of a FTIR spectrometer.

5.2 OPTICAL COATINGS

Table [2] contains the list of the samples to be characterized. The list was realized considering contributions from CNR and Leonardo, and agreed together. The list resumes also the parameters and the number of samples needed.

Table 2: Samples list, structure and number.

Simple coating samples									
Samples dimensions: 2.5 cm ² diameter									
N	Sample type	Structure	Parameters	Substrates	Ref	p	He+	e	Tot
1	S1W Au	single layer	240 nm	Si wafer	5	29	22	9	65
2	S1G Au	single layer	240 nm	Suprasil	5	5	2	9	21
3	S2W Al	single layer	200 nm	Si wafer	5	29	22	9	65
4	S2G Al	single layer	200 nm	Suprasil	5	7	4	9	25
5	S3GUV SiO ₂	single layer	520 nm	Sapphire	5	29	22	9	65
6	S3W SiO ₂	single layer	520 nm	Si wafer	5	13	10	9	37
7	S4G TiO ₂	single layer	360 nm	Suprasil	5	29	22	9	65
8	S4W TiO ₂	single layer	360 nm	Si wafer	5	13	10	9	37
9	S5G ZrO ₂	single layer	340 nm	Suprasil	5	27	20	9	61
10	S5W ZrO ₂	single layer	340 nm	Si wafer	5	10	7	9	31
11	S6W Al/SiO ₂	bi-layer	200/80 nm	Si wafer	5	15	13	9	42
12	S7W Al/SiO ₂	bi-layer	210/80 nm	Si wafer	5	15	13	9	42
13	S8G SiO ₂ /TiO ₂	bi-layer	230/83.4 nm	Suprasil	5	15	13	9	42
14	S8W SiO ₂ /TiO ₂	bi-layer	230/83.4 nm	Si wafer	5	17	14	9	45
15	S9G SiO ₂ /ZrO ₂	bi-layer	230/104.2 nm	Suprasil	5	15	13	9	42
16	S9W SiO ₂ /ZrO ₂	bi-layer	230/104.2 nm	Si wafer	5	12	10	9	36
17	S10G Au/MgF ₂	bi-layer	200/80 nm	Suprasil	5	16	13	9	43
18	S10W Au/MgF ₂	bi-layer	200/80 nm	Si wafer	5	17	14	9	48
19	S11W Pt	single layer	220 nm	Si wafer	5	29	22	9	
20	W			Si wafer	5	0	0	0	
21	G			Suprasil	5	18	11	9	40
22	GUV			Sapphire	5	12	5	9	33
23	G ₁			S-FPL ₅₁	5	8	5	9	
24	G ₂			N-KZFS ₁₁	5	8	5	9	
25	G ₃			S-FTM ₁₆	5	8	5	9	

5.3 SAMPLES CHARACTERIZATION

Sample 1: S1W Au

All the samples show similar performances.

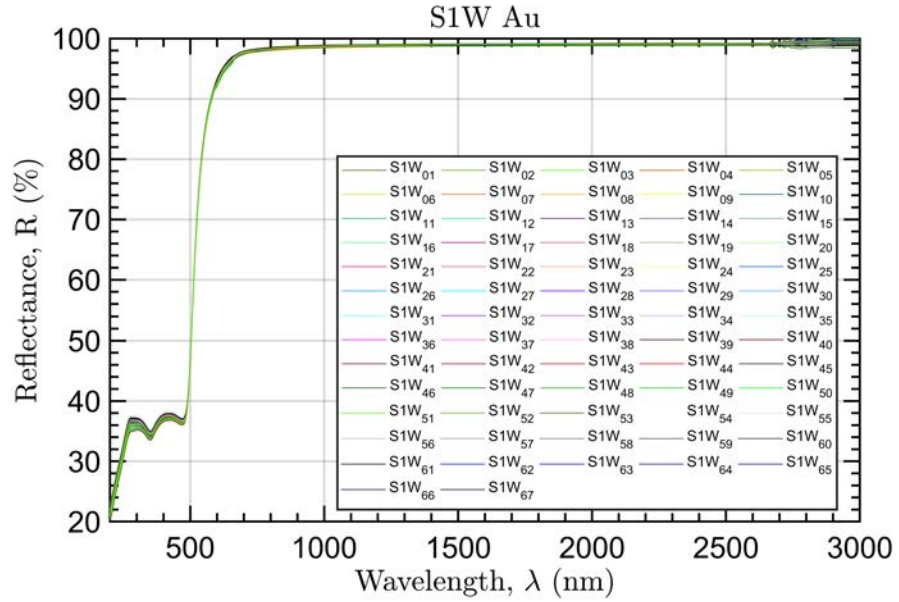


Figure 22: Reflectance of S1W Au samples.

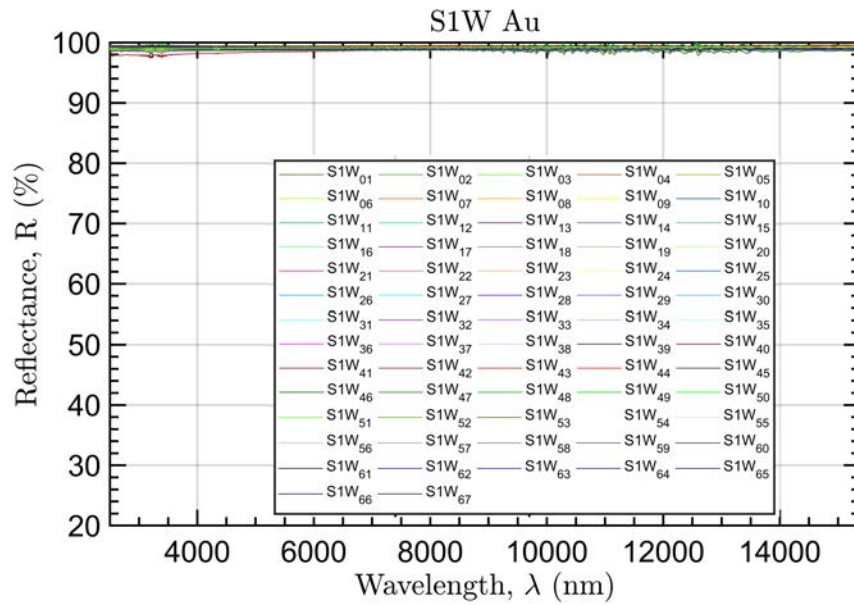


Figure 23: Reflectance of S1W Au samples.

Sample 2: S1G Au

All the samples show similar performances.

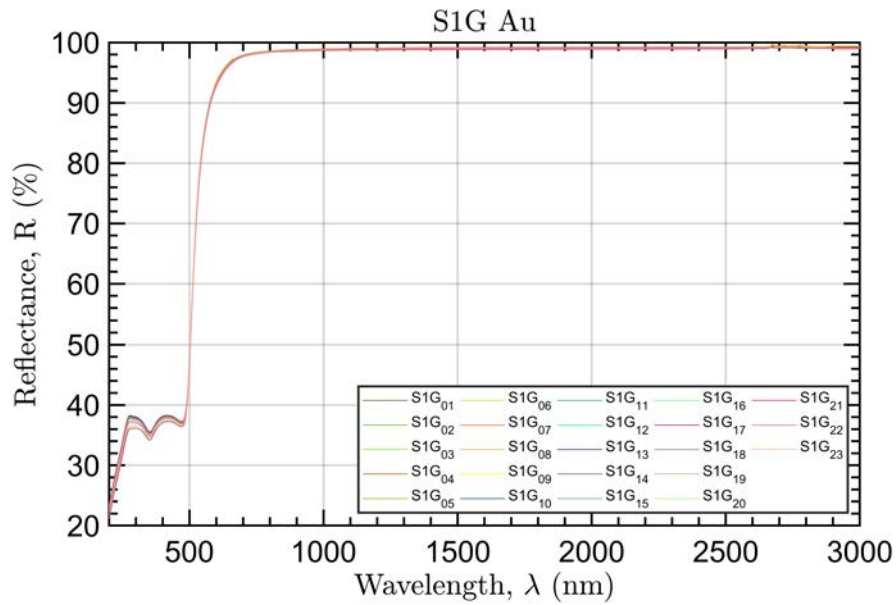


Figure 24: Reflectance of S1G Au samples.

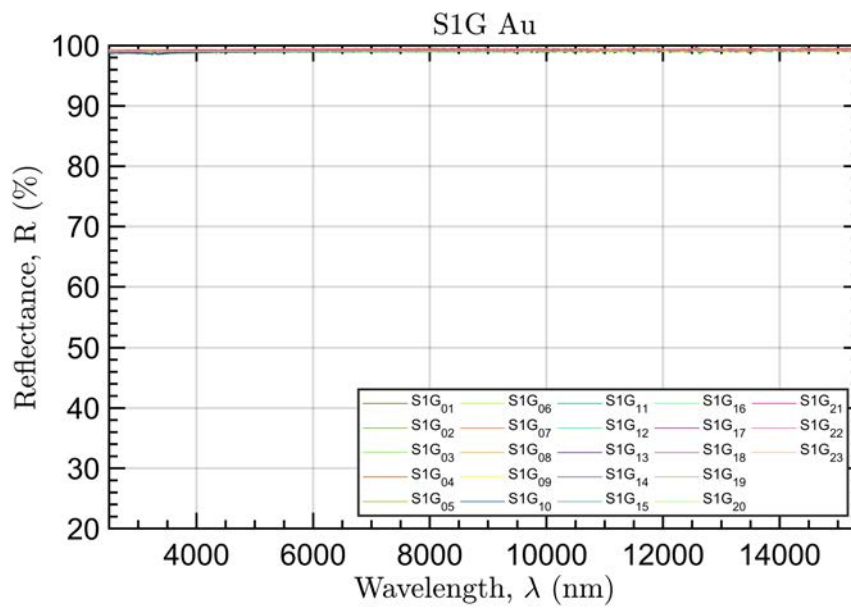


Figure 25: Reflectance of S1G Au samples.

Sample 3: S2W Al

All the samples show similar performances.

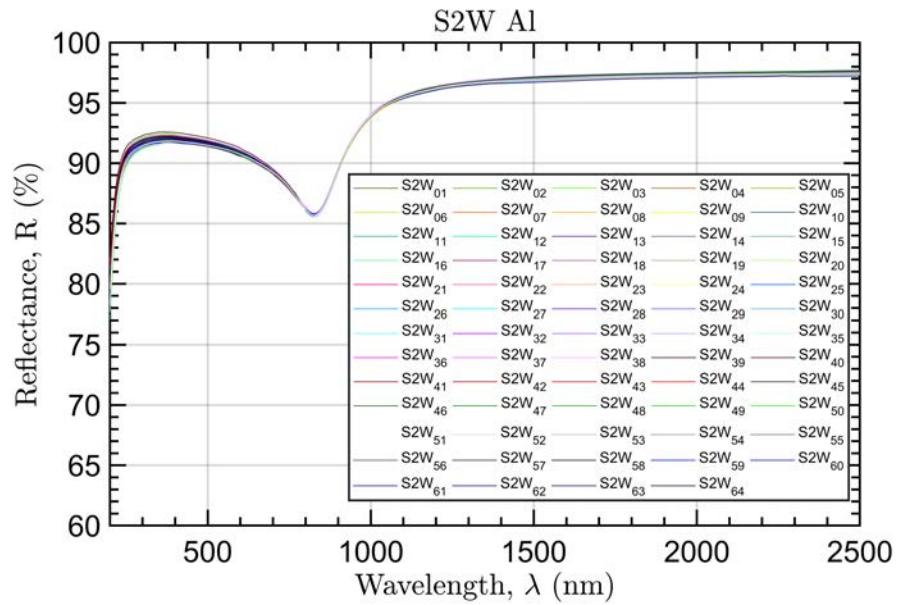


Figure 26: Reflectance of S2W Al samples.

Sample 4: S2G Al

All the samples show similar performances.

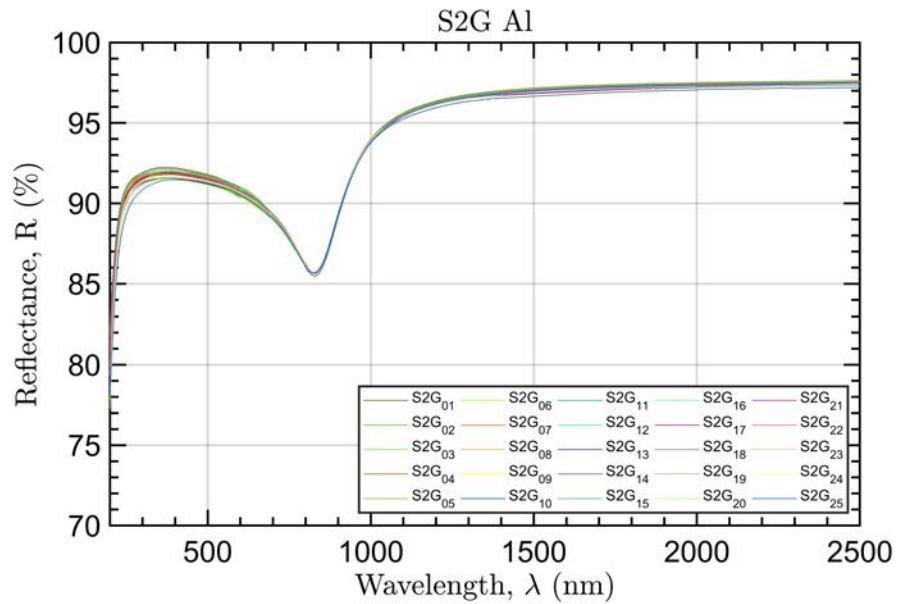


Figure 27: Reflectance of S2G Al samples.

Sample 5: S₃GUV SiO₂

The samples show different responses. This behaviour must be attributed to the performances of the GUV substrate, which varies a lot (see sample 22). We were able to distinguish three main classes which show some similarities in terms of amplitude and peak location (Figure [29])

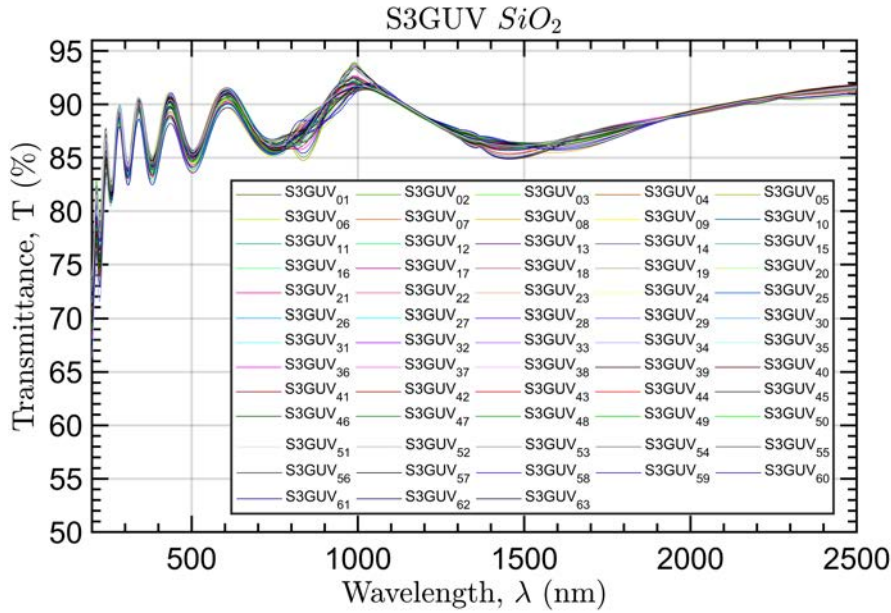


Figure 28: Transmittance of S₃GUV SiO₂ samples.

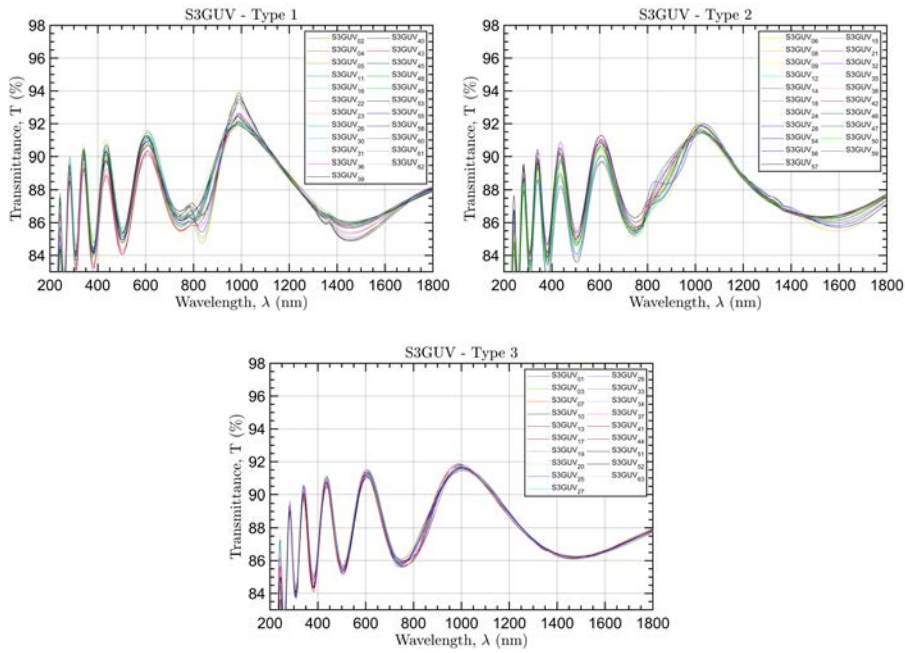


Figure 29: Different types of S₃GUV SiO₂ samples response.

Sample 6: S_3W SiO_2

All the samples show similar performances, with the only exceptions given by S_3W_{06} , S_3W_{15} , S_3W_{21} . The difference must be attributed to a poor satin finish on the back of the specimen that allows a diffusion of the incident radiation towards the first surface. This hypothesis is supported by the fact that at wavelengths lower than 1000 nm the performances are homogeneous, which can be related to the Si behaviour that is intrinsically absorbent and no contributions deriving from the reflection of the second surface are present in that spectral region.

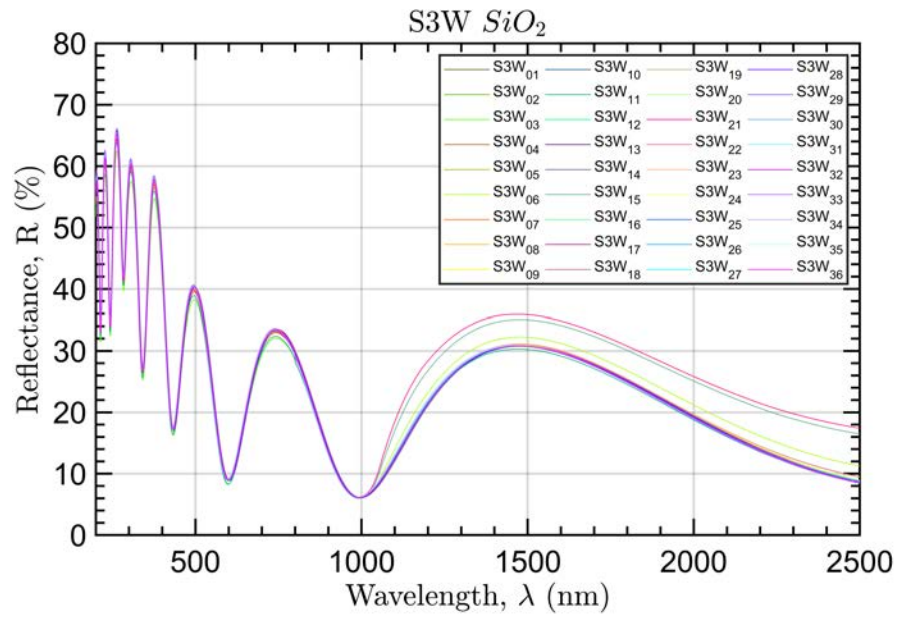


Figure 30: Reflectance of S_3W SiO_2 samples.

Sample 7: S₄G TiO₂

All the samples show similar performances.

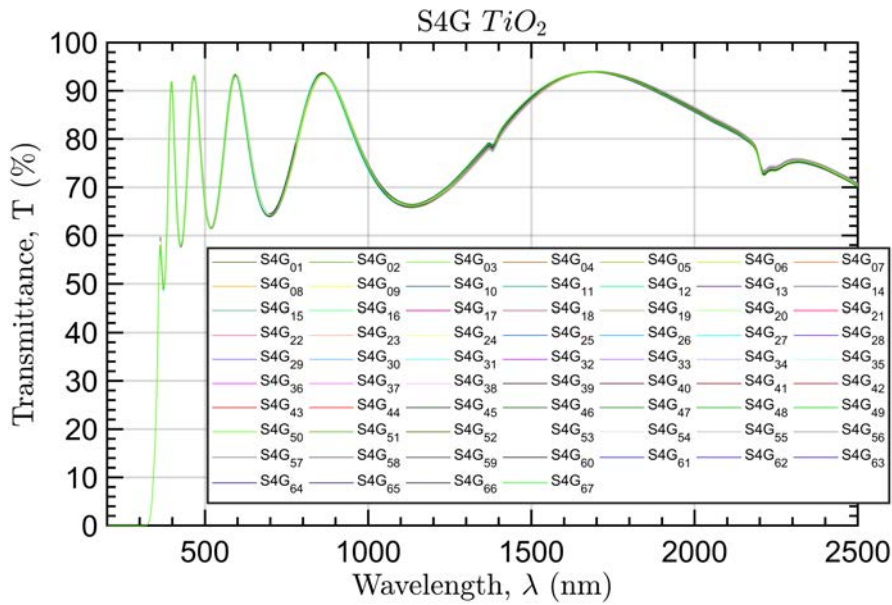


Figure 31: Transmittance of S₄G TiO₂ samples.

Sample 8: S₄W TiO₂

All the samples show similar performances. Sample S₄W₁₃ got broken so that the measure is not reported.

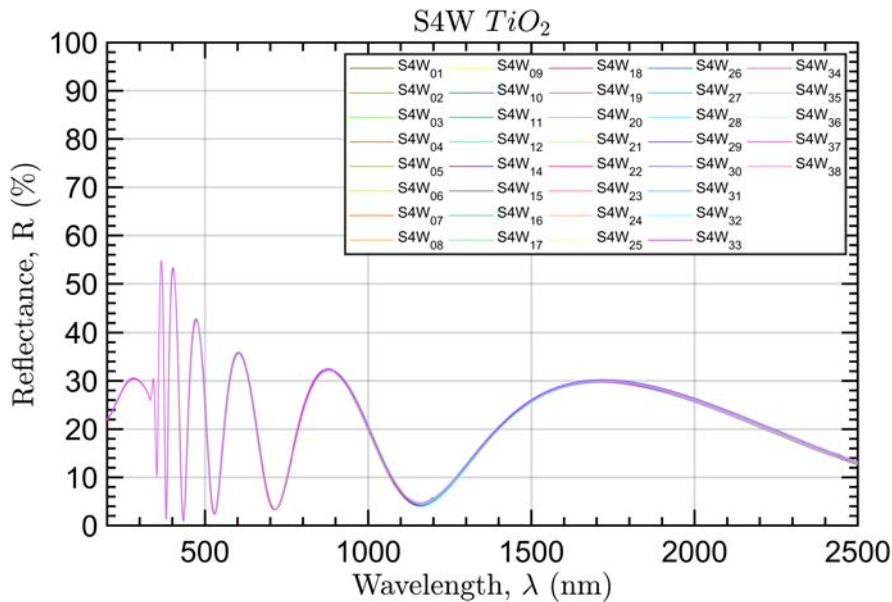


Figure 32: Reflectance of S₄W TiO₂ samples.

Sample 9: S₅G ZrO₂

All the samples show similar performances.

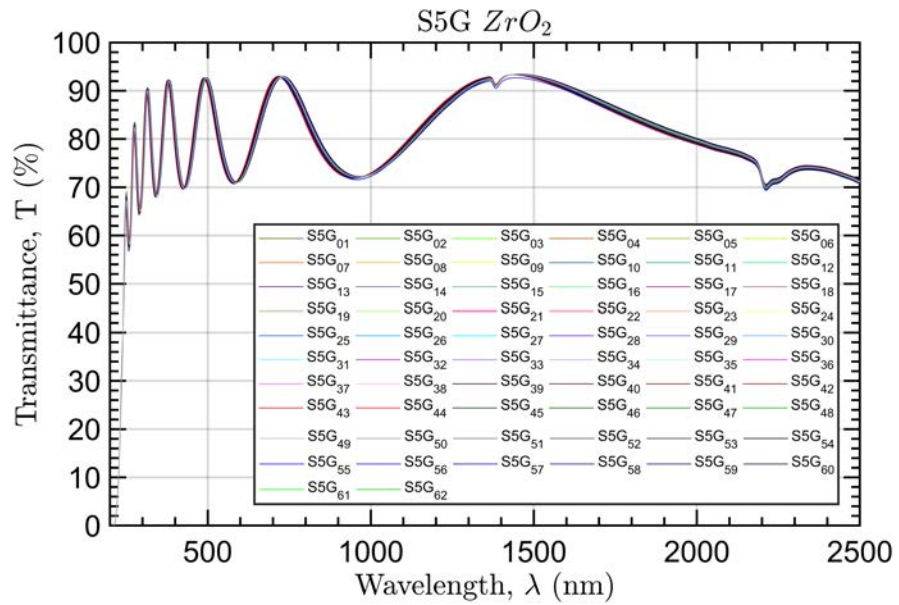


Figure 33: Transmittance of S₅G ZrO₂ samples.

Sample 10: S₅W ZrO₂

All the samples show similar performances.

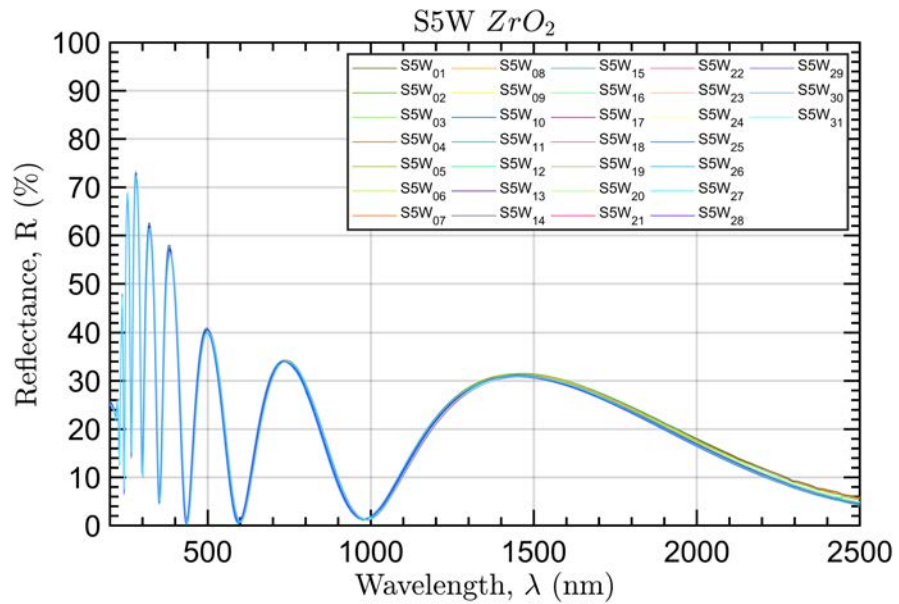


Figure 34: Reflectance of S₅W ZrO₂ samples.

Sample 11: S6W Al/SiO₂

All the samples show similar performances.

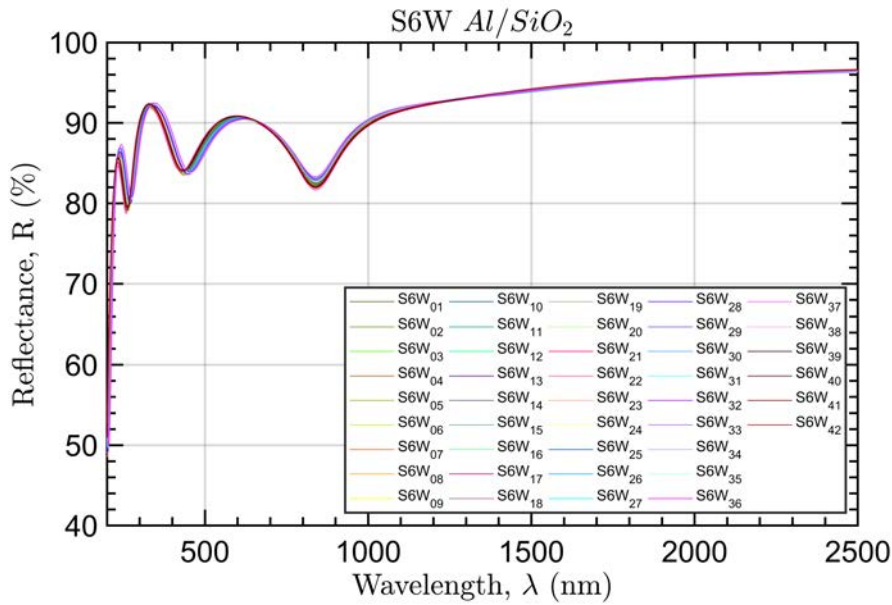


Figure 35: Reflectance of S6W Al/SiO₂ samples.

Sample 12: S7W Ag/SiO₂

All the samples show similar performances.

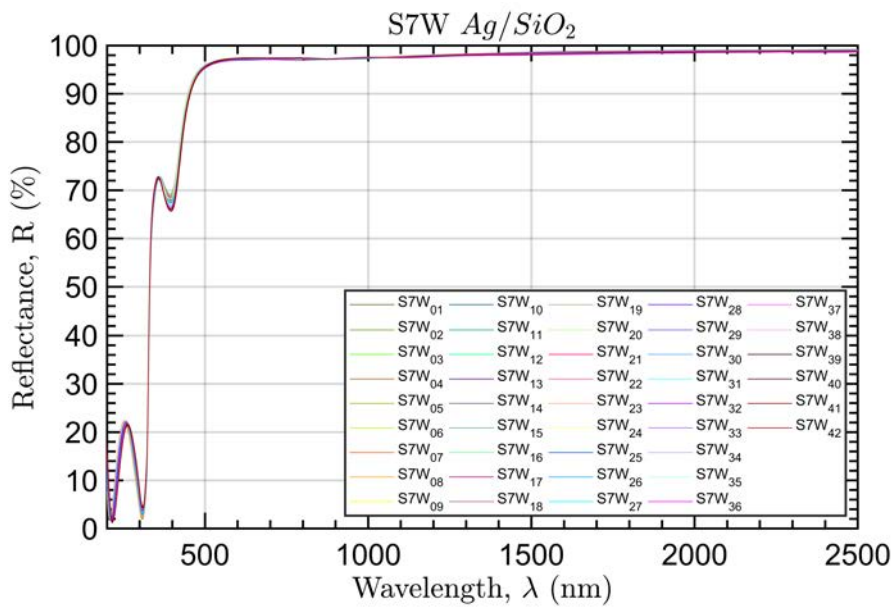


Figure 36: Reflectance of S7W Ag/SiO₂ samples.

Sample 13: S8G SiO₂/TiO₂

All the samples show similar performances.

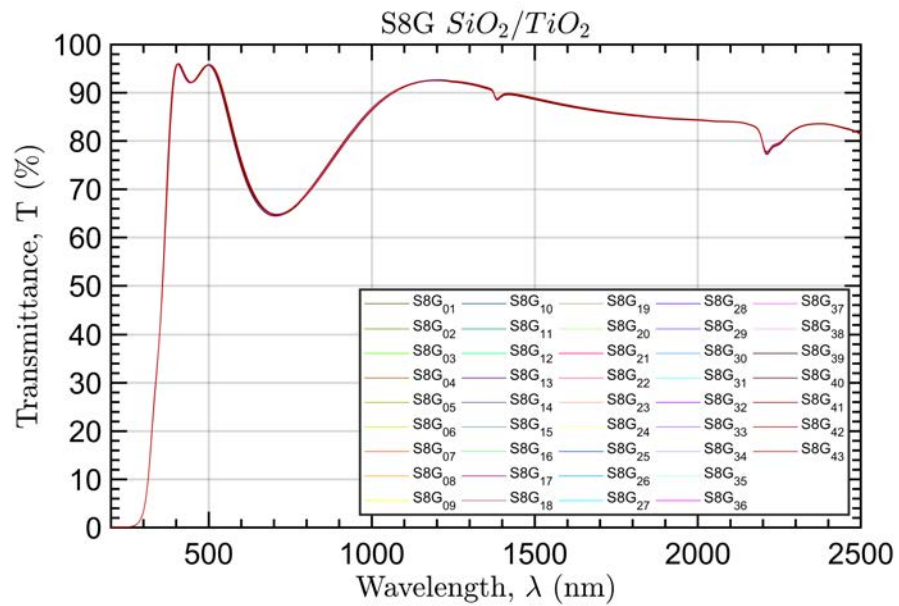


Figure 37: Transmittance of S8G SiO₂/TiO₂ samples.

Sample 14: S8W SiO₂/TiO₂

All the samples show similar performances, with the only exceptions given by S8W₂₀, S8W₂₉ and S8W₃₂.

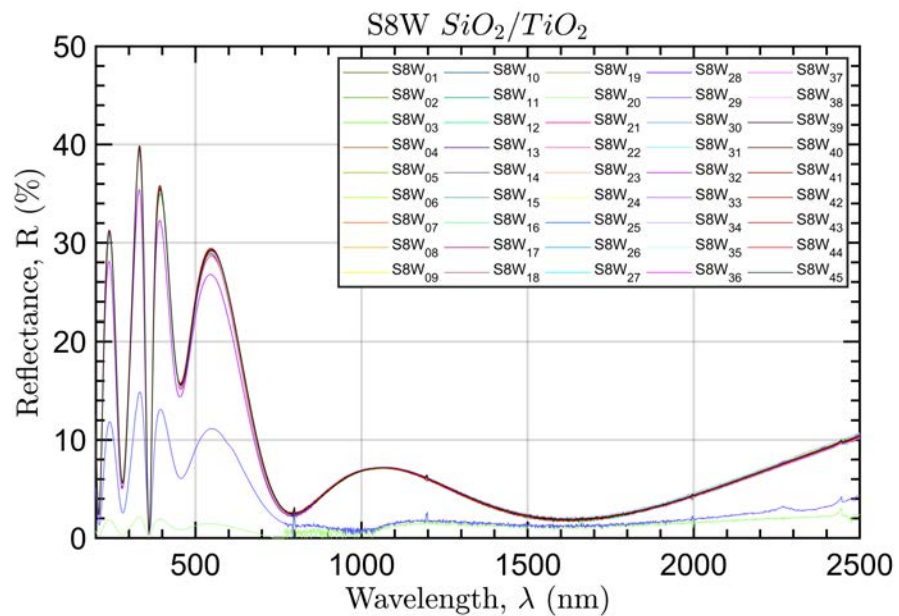


Figure 38: Reflectance of S8W SiO₂/TiO₂ samples.

Sample 15: S9G SiO₂/ZrO₂

All the samples show similar performances.

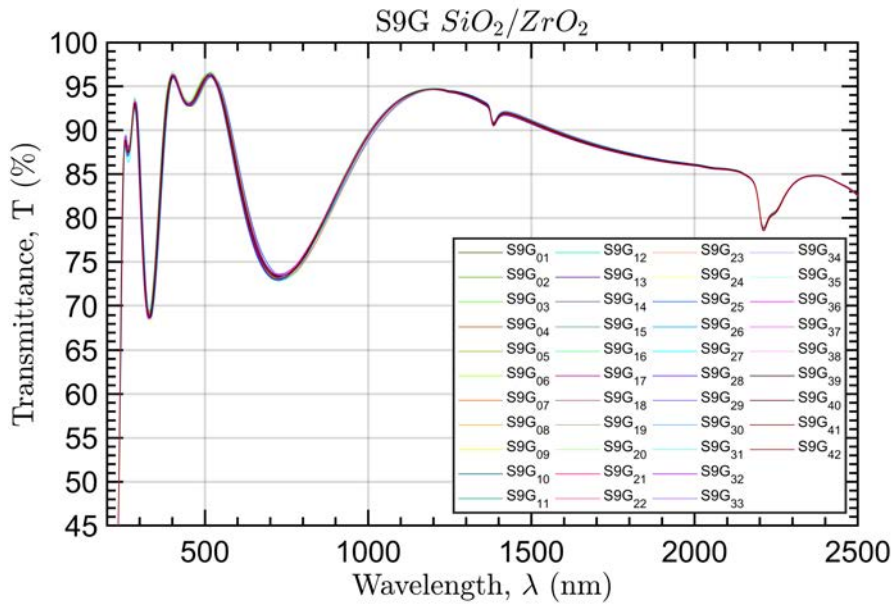


Figure 39: Transmittance of S9G SiO₂/ZrO₂ samples.

Sample 16: S9W SiO₂/ZrO₂

All the samples show similar performances.

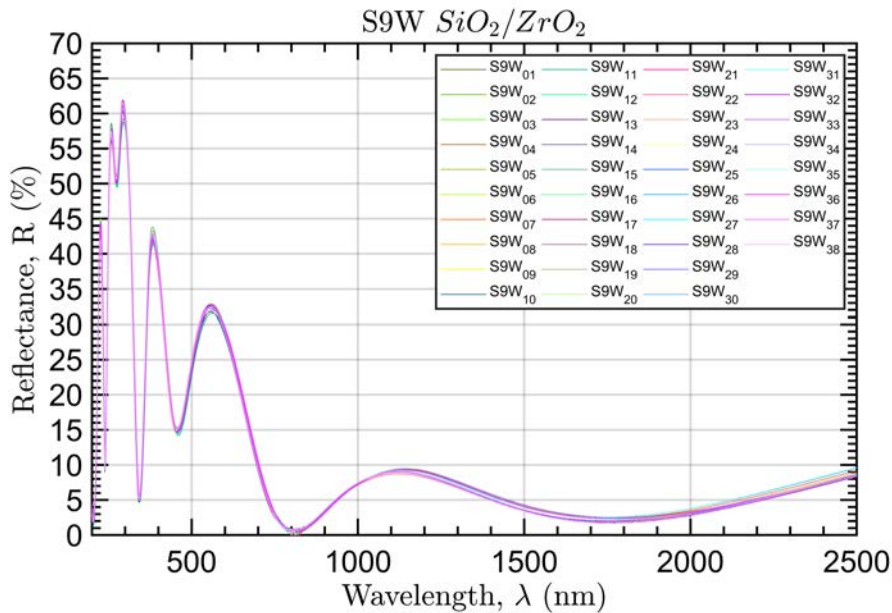


Figure 40: Reflectance of S9W SiO₂/ZrO₂ samples.

Sample 17: S10G Au/MgF₂

All the samples show similar performances.

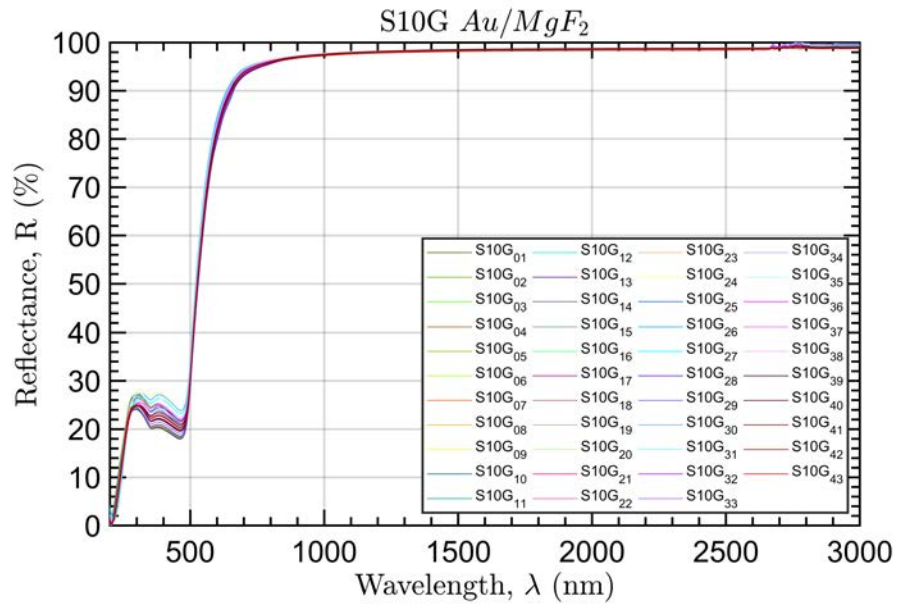


Figure 41: Reflectance of S10G Au/MgF₂ samples.

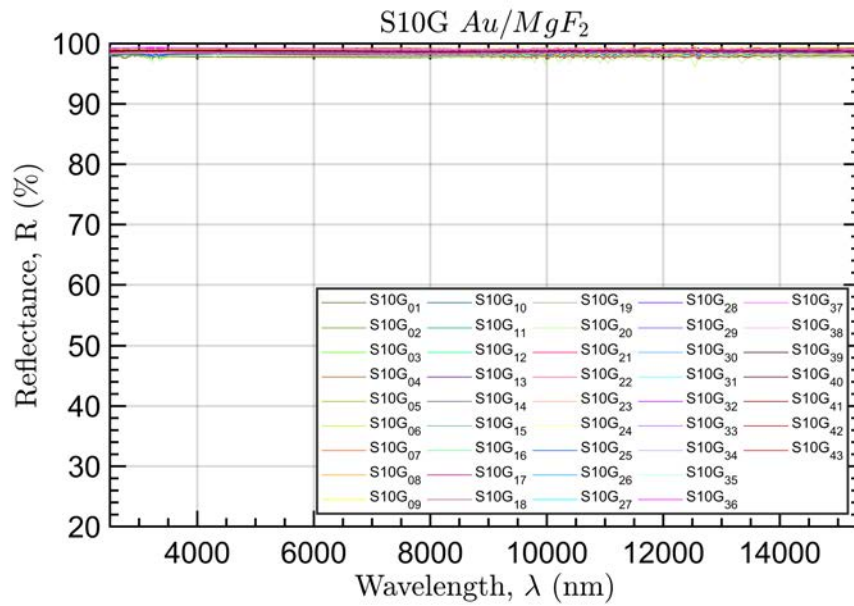


Figure 42: Reflectance of S10G Au/MgF₂ samples.

Sample 18: S10W Au/MgF₂

All the samples show similar performances.

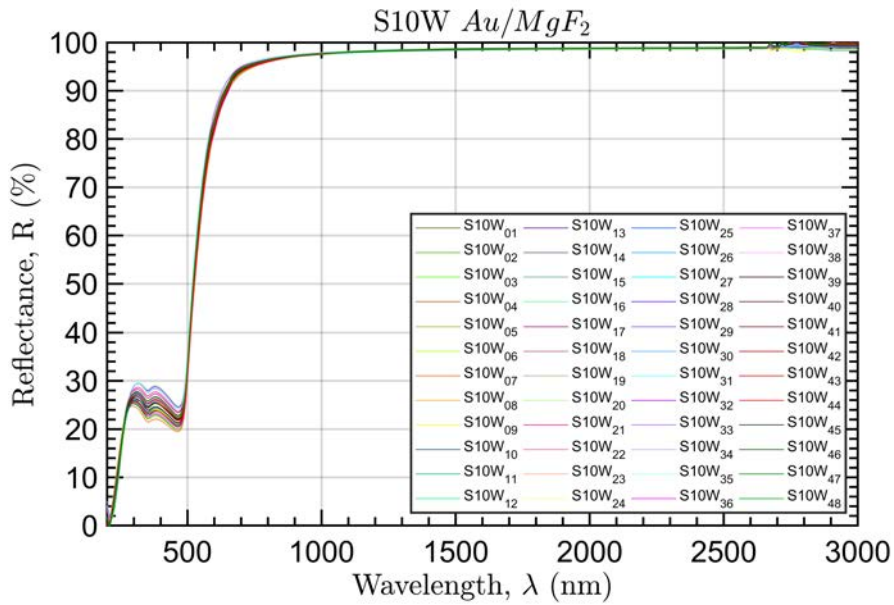


Figure 43: Reflectance of S10W Au/MgF₂ samples.

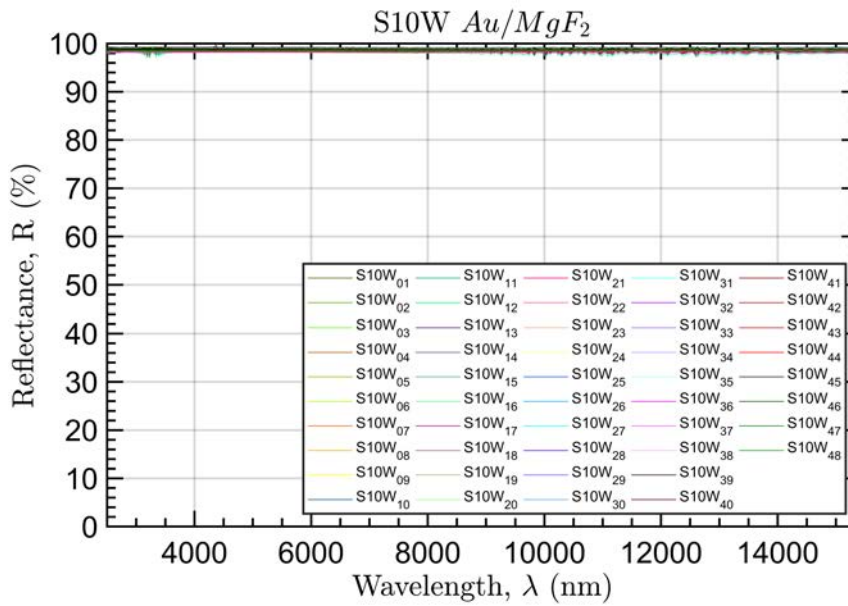


Figure 44: Reflectance of S10W Au/MgF₂ samples.

Sample 19: S11W Pt

All the samples show similar performances. Sample S11W₃₁ got broken so that the measure is not reported.

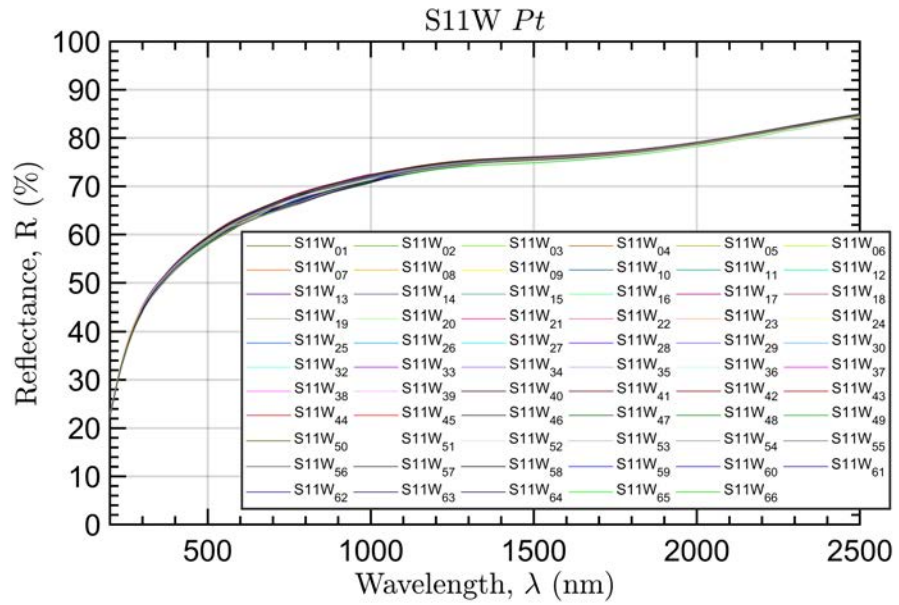


Figure 45: Reflectance of S11W Pt samples.

Sample 20: W

All the samples show similar performances.

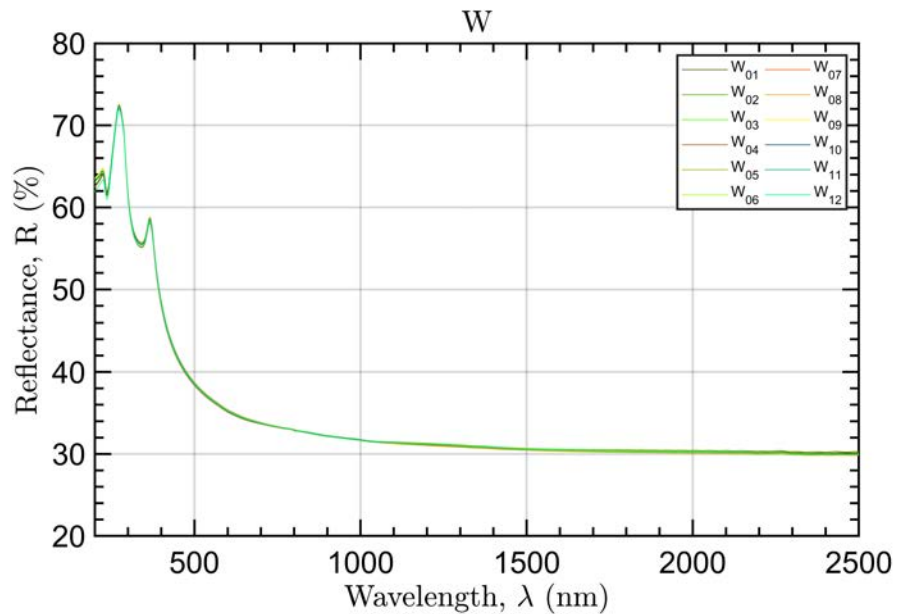


Figure 46: Reflectance of W samples.

Sample 21: G

All the samples show similar performances.

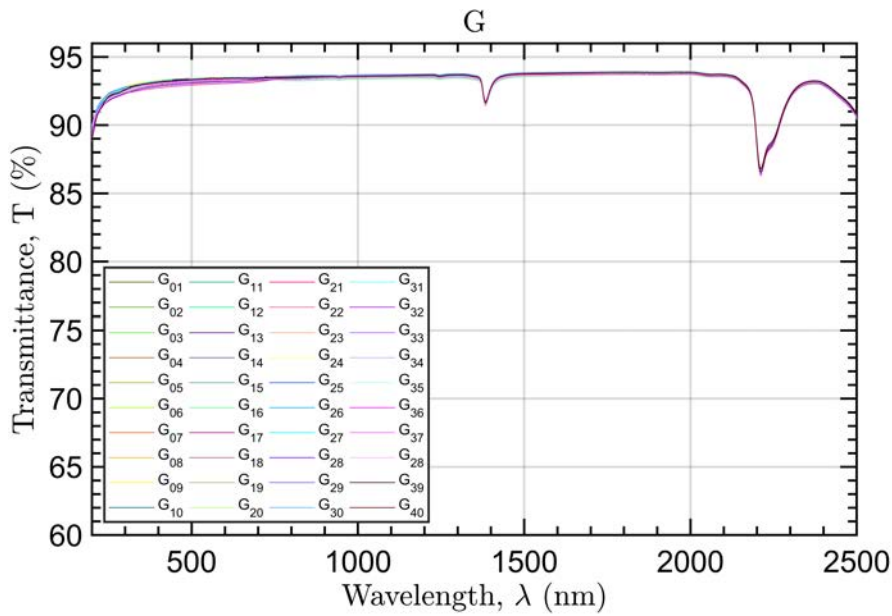


Figure 47: Transmittance of G samples.

Sample 22: GUV

In this case we obtained very different results in terms of reflectance shape, with local maxima and minima varying in a wide range.

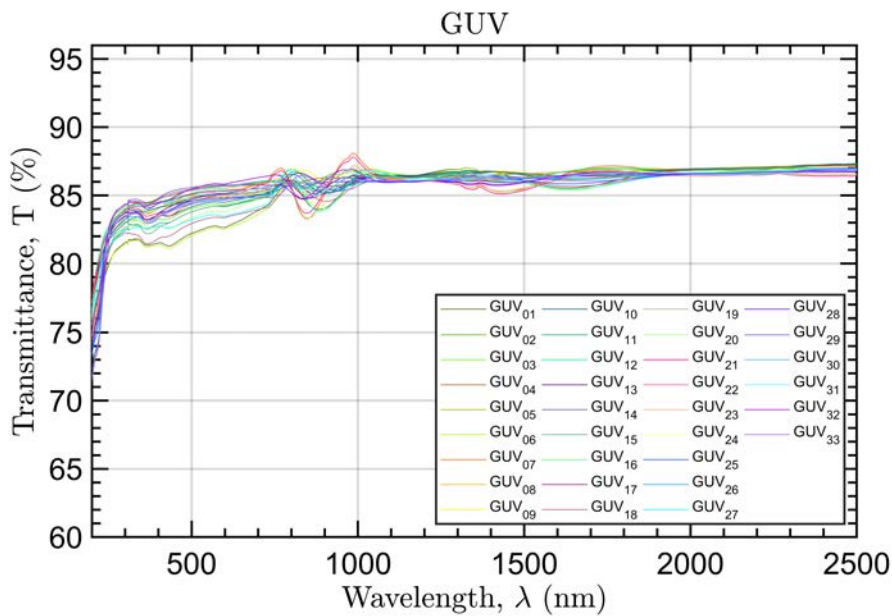


Figure 48: Transmittance of GUV samples.

As for S3GUV, we were able to distinguish three different types of samples which show similar characteristics (Figure [49]).

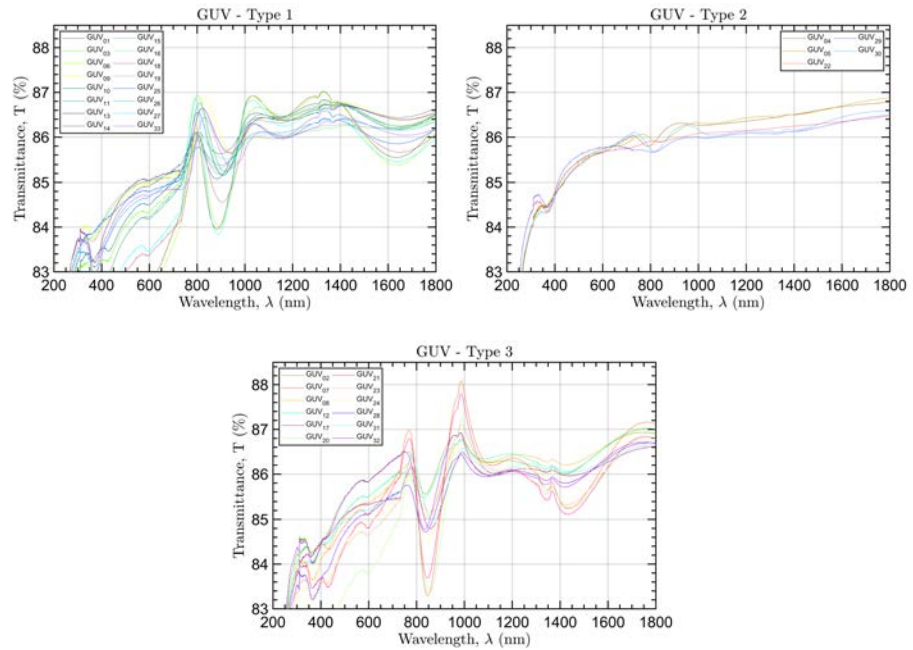


Figure 49: Different types of GUV samples response.

Sample 23: G1

All the samples show similar performances.

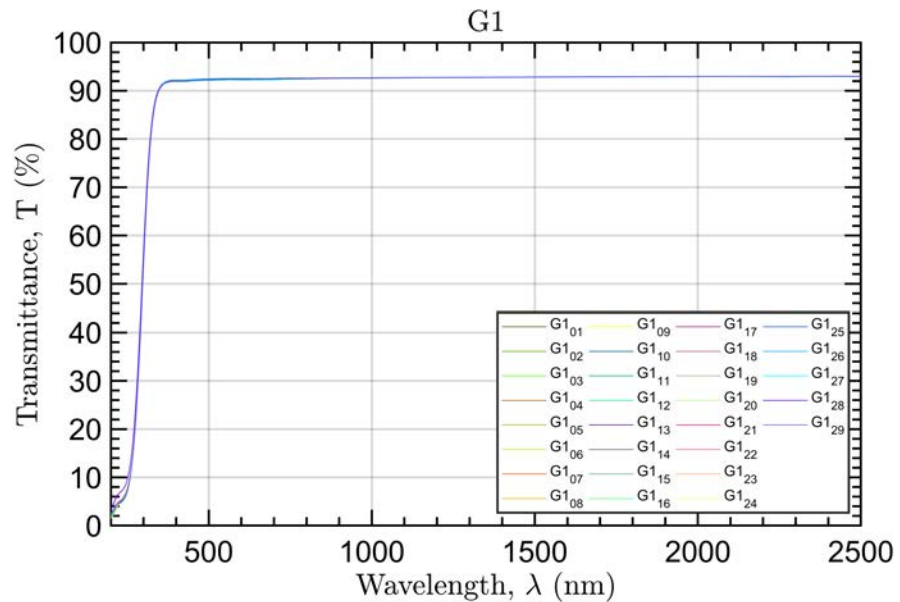


Figure 50: Transmittance of G1 samples.

Sample 24: G2

All the samples show similar performances. Sample G2₂₉ has been discarded because it got damaged.

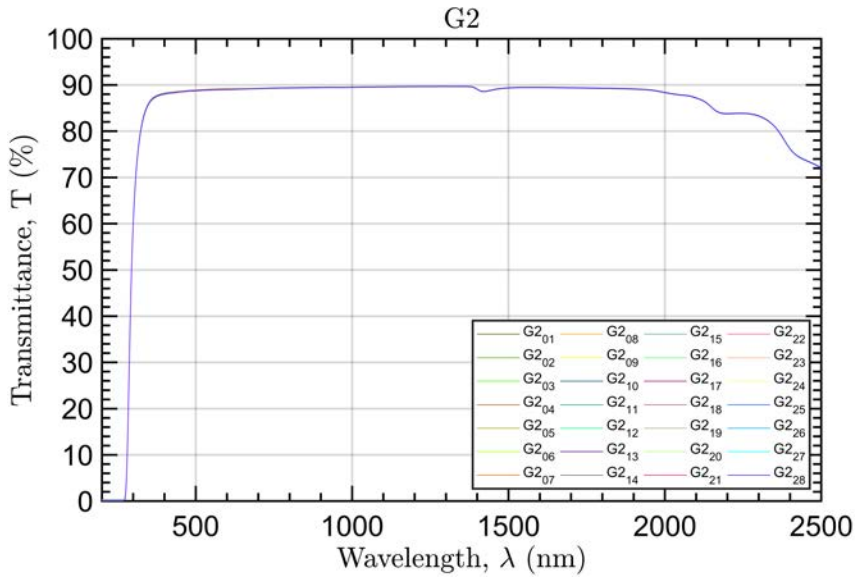


Figure 51: Transmittance of G2 samples.

Sample 25: G3

All the samples show similar performances. Sample G3₀₁ has been discarded because it got damaged.

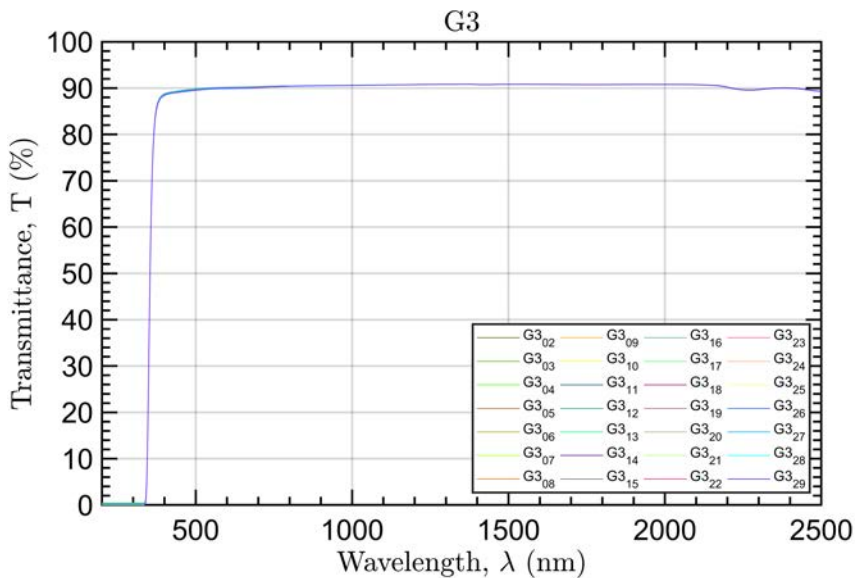


Figure 52: Transmittance of G3 samples.

5.4 SIMULATION AND FITTING

In addition to the optical characterization reported in previous pages, some simulations were performed to verify whether the samples structure was that of Table [2]. When possible, measurement data were fitted using the layer thicknesses as free parameters in order to retrieve the real structure to be compared with the nominal one.

In case of single layers, fittings were performed by initializing a new structure with the nominal thickness and iteratively computing a function of merit given by the *least-square difference* between the simulated curve and the average of the measured ones. The thickness increment was set to be always positive (increasing thickness) since, from a visual comparison, the simulated curve never appeared to be broader but rather compressed with respect to the measurements, which is associated to a thicker coating. In case of bi-layers, the Matlab function *nlinfit* was used.

In this analysis we had to exclude metal coatings since electromagnetic radiation do not penetrate into the layers, thus it was not possible to retrieve the real thicknesses from fitting. As a consequence, for metal single layers, fitting is not reported. Moreover, fittings with dielectric coatings were performed considering only data of samples with glass substrates (coatings on wafers have been deposited in the same run and are more difficult to simulate due to a insufficient knowledge of Si optical constants).

Samples 1 and 2: S1W Au & S1G Au

Nominal thicknesses seem to be coherent with the measurements. The discrepancy for wavelengths lower than 500 nm must be related to a difference between the optical constants used for the simulation and those of the real material.

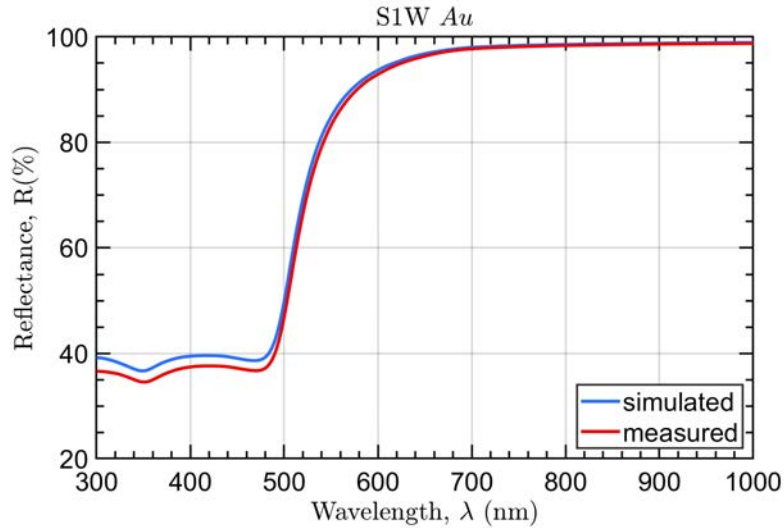


Figure 53: Simulation with nominal thickness (blue curve) and measured reflectance (red curve) of S1W Au samples.

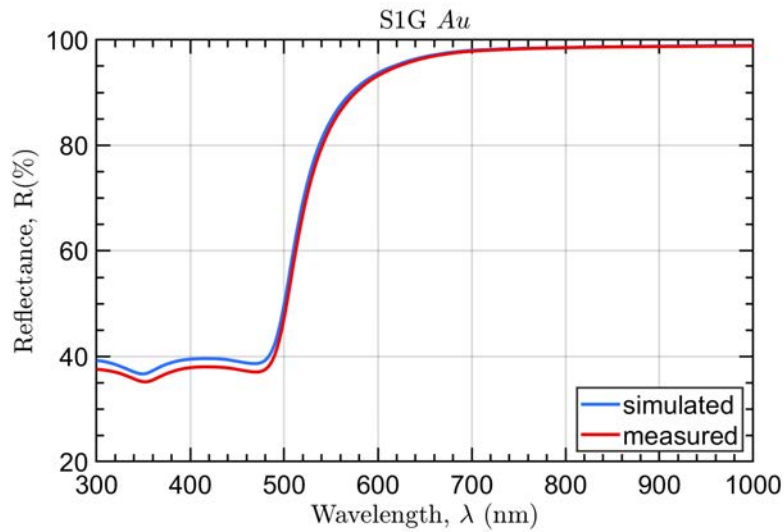


Figure 54: Simulation with nominal thickness (blue curve) and measured reflectance (red curve) of S1G Au samples.

Sample 3 and 4: S2W Al & S2G Al

Nominal thicknesses seem to be coherent with the measurements.

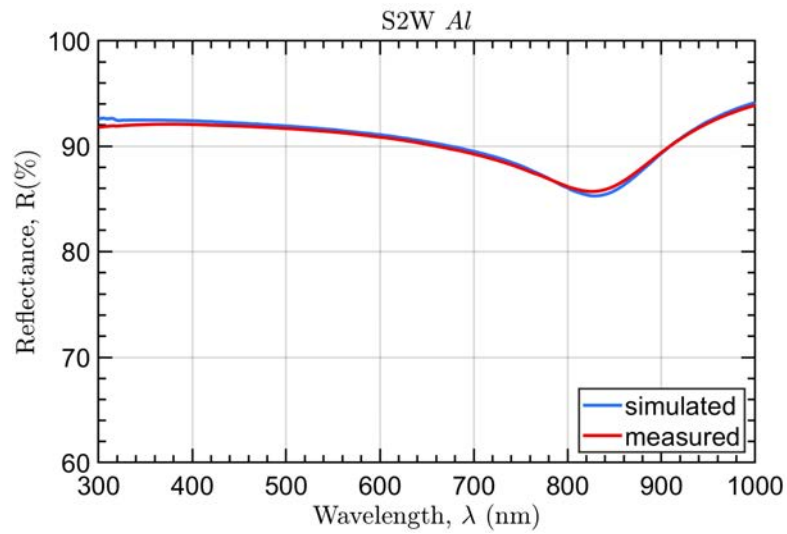


Figure 55: Simulation with nominal thickness (blue curve) and measured reflectance (red curve) of S2W Al samples.

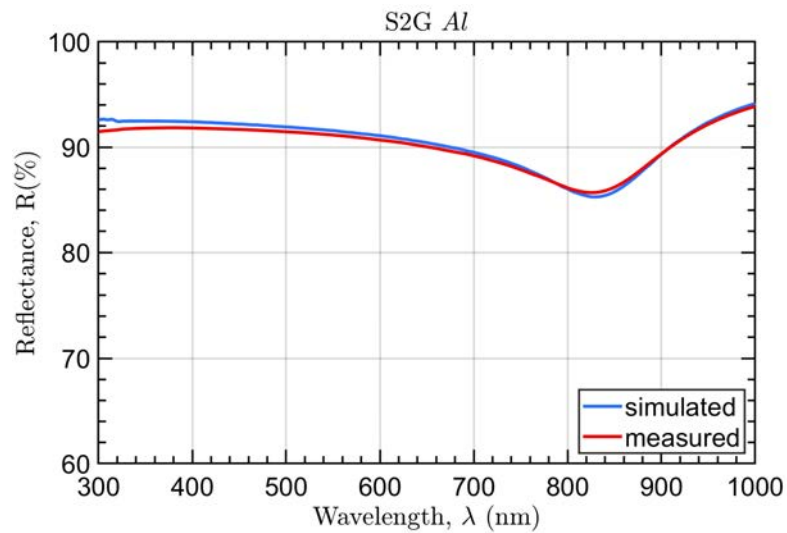


Figure 56: Simulation with nominal thickness (blue curve) and measured reflectance (red curve) of S2G Al samples.

Sample 5: $S_3\text{GUV SiO}_2$

The fitting analysis revealed a real thickness of 511.6 nm of SiO_2 . The differences must be related to optical constants of the GUV substrate.

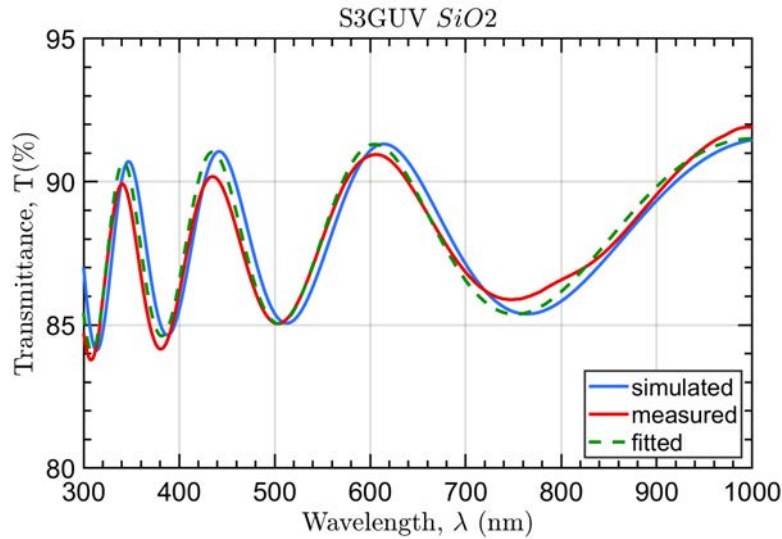


Figure 57: Simulation with nominal thickness (blue curve), estimated thickness (green curve) and measured reflectance (red curve) of $S_3\text{GUV SiO}_2$ samples.

Sample 7: $S_4\text{G TiO}_2$

The fitting analysis revealed a real thickness of 375.4 nm of TiO_2 .

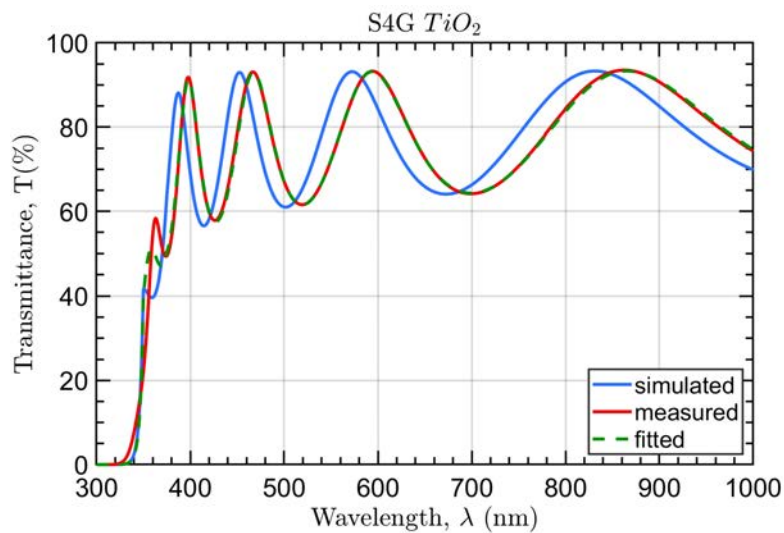


Figure 58: Simulation with nominal thickness (blue curve), estimated thickness (green curve) and measured reflectance (red curve) of $S_4\text{G TiO}_2$ samples.

Sample 9: S5G ZrO₂

The fitting analysis revealed a real thickness of 346 nm of ZrO₂.

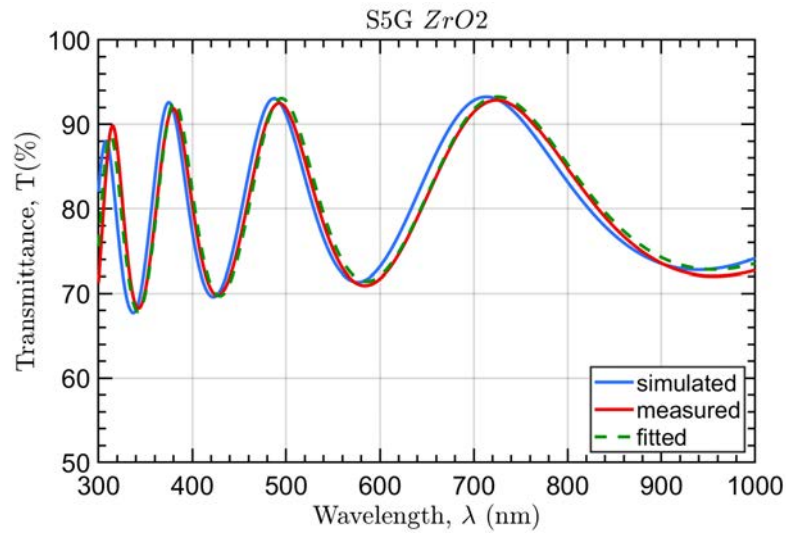


Figure 59: Simulation with nominal thickness (blue curve), estimated thickness (green curve) and measured reflectance (red curve) of S5G ZrO₂ samples.

Sample 11: S6W Al/SiO₂

The fitting analysis revealed a real thickness of 207.1 nm of the SiO₂ top layer. In this case the difference between the real and theoretical structure is not negligible.

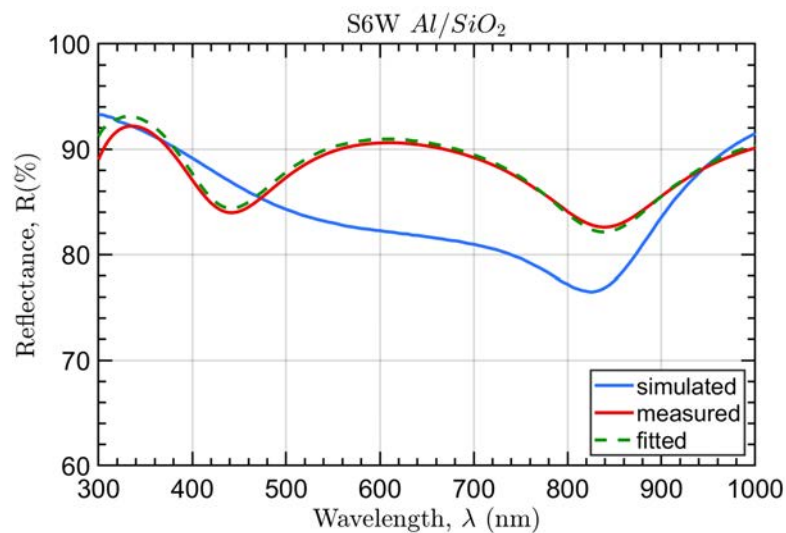


Figure 60: Simulation with nominal thickness (blue curve), estimated thickness (green curve) and measured reflectance (red curve) of S6W Al/SiO₂ samples.

Sample 12: S7W Ag/SiO₂

In this case, the fitting was not possible because the optical constants of Ag were unclear. Further investigation is programmed.

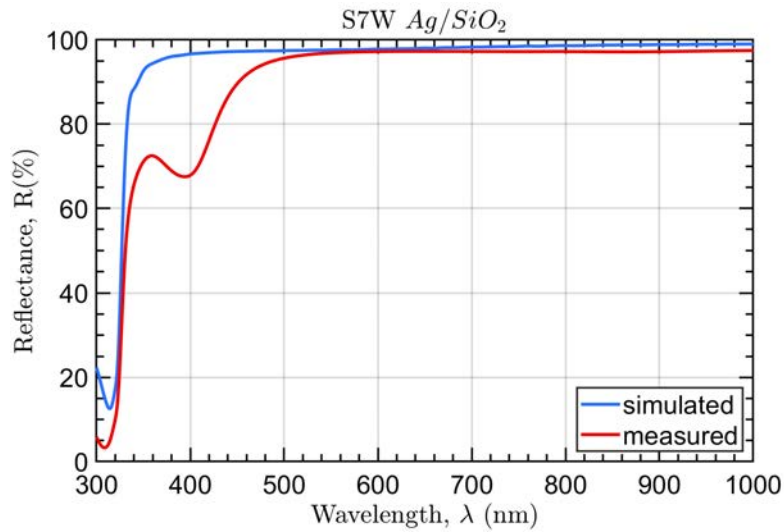


Figure 61: Simulation with nominal thickness (blue curve) and measured reflectance (red curve) of S7W Ag/SiO₂ samples.

Sample 13: S8G SiO₂/TiO₂

The fitting analysis revealed a real thickness of 232.7 nm of the SiO₂ top layer and 84.9 nm for the TiO₂ one.

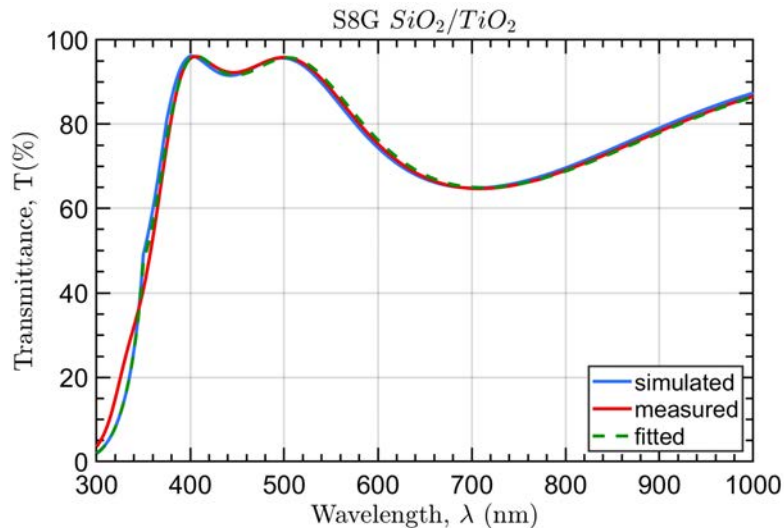


Figure 62: Simulation with nominal thickness (blue curve), estimated thickness (green curve) and measured reflectance (red curve) of S9G SiO₂/TiO₂ samples.

Sample 15: S9G SiO₂/ZrO₂

The fitting analysis revealed a real thickness of 232.7 nm of the SiO₂ top layer and 104.2 nm for the ZrO₂ one.

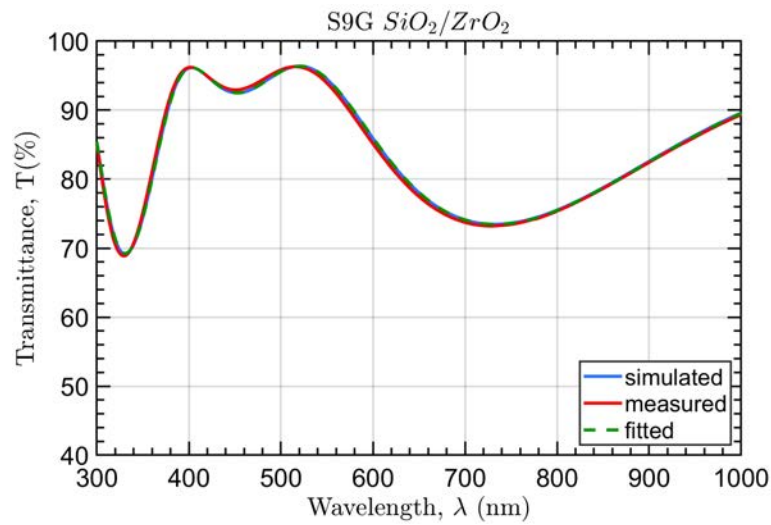


Figure 63: Simulation with nominal thickness (blue curve), estimated thickness (green curve) and measured reflectance (red curve) of S8G SiO₂/ZrO₂ samples.

Sample 18: S10W Au/MgF₂

The discrepancy must be related to a difference between the optical constants of Au and MgF₂ used for the simulation and those of the real material.

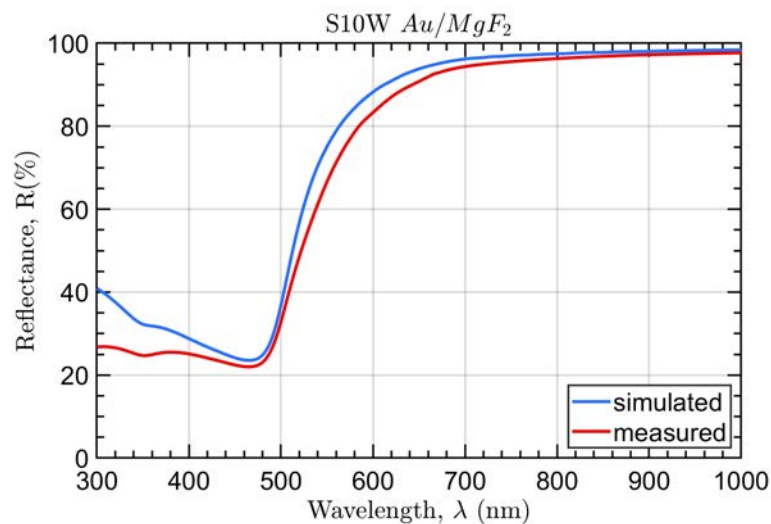


Figure 64: Simulation with nominal thickness (blue curve), estimated thickness (green curve) and measured reflectance (red curve) of S10W Au/MgF₂ samples.

Sample 19: S11W Pt

In this case, the two curves show a similar shapes. The difference between these must be related only to the optical constants of Pt used for the simulation and those of the real material.

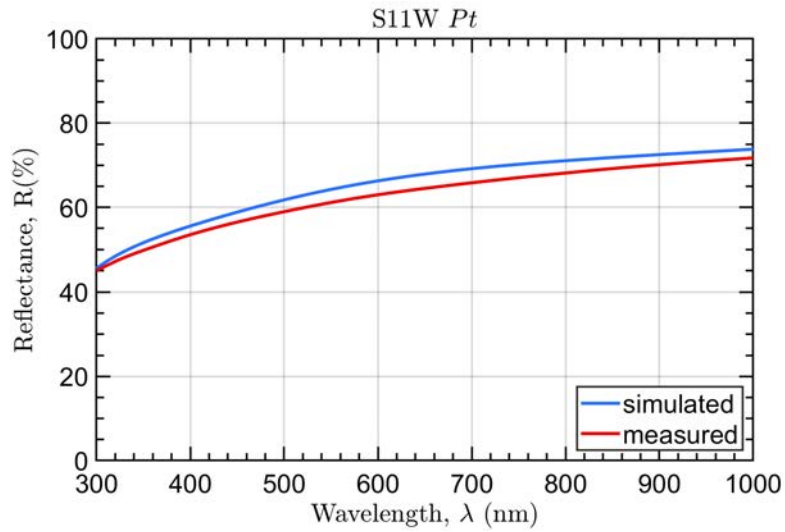


Figure 65: Simulation with nominal thickness (blue curve), estimated thickness (green curve) and measured reflectance (red curve) of S11W Pt samples.

CONCLUSIONS

In this master thesis we provided a mathematical model to simulate the optical response of a multilayer structure prior and after different particles implantation. This was implemented in Matlab to create a simple but effective software that will be used until the conclusion of the ESA project and definitely for other future works. The model provided a starting point to design the samples discussed and to study the variation in optical performance due to ions implantation.

In order to associate theoretical and experimental results, a huge number of samples were optically characterized in terms of (absolute) reflectance or transmittance. This process was needed since the totality of the samples will eventually be characterized for a second time after the irradiation process, and a comparison between the two curves will provide results for the damaging model. Moreover, to improve our knowledge of the samples, measured data were fitted (when possible) to retrieve informations about the real thicknesses.

This analysis pointed out a series of problems in terms of differences between ideal and real structures. This could be related either to the thicknesses or to the optical constants of different material, for which our knowledge is limited to the literature or to the samples provider. For this reason further investigations are planned, especially for the optical constants of gold (Au), titanium dioxide (TiO_2), silver (Ag), magnesium fluoride (MgF_2) and palladium (Pt).

The following step would be the irradiation itself. The protons and He ions irradiation will be performed at Helmholtz-Zentrum Dresden-Rossendorf, Institute of Ion Beam Physics and Materials Research Ion Beam Center, while the electrons irradiation at low energy will be performed at Technical University of Denmark, Center for Nuclear Technologies. The electron irradiation at high energy will be performed at Istituto Nazionale per la Fisica Nucleare – Laboratori Nazionali di Frascati (INFN-LNF, Italy) at the DAFNE Beam Test Facility (BTF).

The improved knowledge in understanding the effects of electrons, protons and ions on coatings and the definition of tests procedure will be applied to develop and test optical components in view of their potential application to the ESA JUICE mission. The ESA project results will then be useful in the development of the JUICE instrumentation. More in general, the skills acquired within the project will be useful in the development and qualification of optical coatings for future space mission instrumentation, even when materials, structures and experimental conditions are different from those considered in the present project.

APPENDIX

GENERAL PLANE WAVE SOLUTION

In this section, the general solution of the homogeneous Helmholtz is computed with the method of separation of variables. In free-space, this can be written as

$$\nabla^2 \bar{E} + k_0^2 \bar{E} = \frac{\partial^2 \bar{E}}{\partial x^2} + \frac{\partial^2 \bar{E}}{\partial y^2} + \frac{\partial^2 \bar{E}}{\partial z^2} + k_0^2 \bar{E} = 0$$

and this vector wave equation holds for each rectangular component of \bar{E} :

$$\frac{\partial^2 E_i}{\partial x^2} + \frac{\partial^2 E_i}{\partial y^2} + \frac{\partial^2 E_i}{\partial z^2} + k_0^2 E_i = 0 \quad (163)$$

where the index $i = x, y, \text{ or } z$. This equation can be solved by the method of *separation of variables*, a standard technique for treating such partial differential equations. The method begins by assuming that the solution to (163) for, say, E_x , can be written as a product of three functions for each of the three coordinates:

$$E_x(x, y, z) = f(x)g(y)h(z) \quad (164)$$

Substituting (164) into (163) and dividing by fgh gives

$$\frac{f''}{f} + \frac{g''}{g} + \frac{h''}{h} + k_0^2 = 0 \quad (165)$$

where the double primes denote the second derivative. The key step in the argument is to recognize that each of the terms in (165) must be equal to a constant because they are independent of each other. That is, $\frac{f''}{f}$ is only a function of x , and the remaining terms do not depend on x , so $\frac{f''}{f}$ must be a constant, and similarly for the other terms in (165). Thus, we define three separation constants, k_x, k_y , and k_z , such that

$$\frac{f''}{f} = -k_x^2 \quad \frac{g''}{g} = -k_y^2 \quad \frac{h''}{h} = -k_z^2$$

or equivalently

$$\frac{\partial^2 f}{\partial x^2} + k_x^2 f = 0 \quad \frac{\partial^2 g}{\partial y^2} + k_y^2 g = 0 \quad \frac{\partial^2 h}{\partial z^2} + k_z^2 h = 0 \quad (166)$$

Combining (164) and (166) shows that

$$k_x^2 + k_y^2 + k_z^2 = 0 \quad (167)$$

The partial differential equation of (165) has now been reduced to three separate ordinary differential equations in (166). These are found to be classical expression of harmonic oscillators, thus solutions are of the form:

$$\frac{\partial^2 f}{\partial x^2} + k_x^2 f = 0 \quad \Rightarrow \quad f(x) = F^- e^{-ik_x x} + F^+ e^{+ik_x x}$$

As we saw in the previous section, the terms with + signs result in waves travelling in the negative x , y , or z direction, while the terms with – signs result in waves travelling in the positive direction. Both solutions are possible and are valid; the amount to which these various terms are excited is dependent on the source of the fields and the boundary conditions. For our present discussion we will select a plane wave travelling in the positive direction for each coordinate and write the complete solution for E_x as

$$E_x(x, y, z) = F e^{-i(k_x x + k_y y + k_z z)} \quad (168)$$

where F is an arbitrary amplitude constant. Now define the wavevector \bar{k} as

$$\bar{k} = k_x \hat{x} + k_y \hat{y} + k_z \hat{z} = k_0 \hat{s} \quad (169)$$

where $|\bar{k}| = k_0$ is the wavenumber and

$$\hat{s} = \alpha \hat{x} + \beta \hat{y} + \gamma \hat{z} \quad (170)$$

is a unit vector in the direction of propagation. Moreover, by defining a position vector as

$$\hat{r} = x \hat{x} + y \hat{y} + z \hat{z} \quad (171)$$

equation (168) can be written as

$$E_x(x, y, z) = A e^{-i\bar{k} \cdot \hat{r}} \quad (172)$$

Solutions to (163) for E_y and E_z are, of course, similar in form to E_x of but with different amplitude constants:

$$E_y(x, y, z) = B e^{-i\vec{k}\cdot\vec{r}} \quad (173)$$

$$E_z(x, y, z) = C e^{-i\vec{k}\cdot\vec{r}} \quad (174)$$

The x , y , and z dependences of the three components of \vec{E} in (172)-(174) must be the same (same k_x , k_y , k_z), because the divergence condition

$$\nabla \cdot \vec{E} = \frac{\partial^2 E_x}{\partial x^2} + \frac{\partial^2 E_y}{\partial y^2} + \frac{\partial^2 E_z}{\partial z^2} = 0 \quad (175)$$

must also be applied in order to satisfy Maxwell's equations, and this implies that E_x , E_y , and E_z must each have the same variation in x , y , and z . This condition also imposes a constraint on the amplitudes A , B , and C because if

$$\vec{E}_0 = A\hat{x} + B\hat{y} + C\hat{z}$$

we have

$$\vec{E} = \vec{E}_0 e^{-i\vec{k}\cdot\vec{r}} \quad (176)$$

BIBLIOGRAPHY

- [1] D. Muller, R.G. Marsden, O.C. St. Cyr, H.R. Gilbert, *Solar Orbiter – exploring the sun-heliosphere connection*, *Solar Physics*, 285(1-2), 25-70, (2013).
- [2] V. D. Kuznetsov, *Solar and heliospheric space missions*, *Advances in Space Research*, 55(3), 879-885, (2015).
- [3] A.J. Coates, A. Wellbrock, M. Yamauchi, *Special issue editorial - Plasma interactions with Solar System Objects: Anticipating Rosetta, Maven and Mars Orbiter Mission*, *Planetary and Space Science* 119, 1-2, (2015)
- [4] G. Naletto, A. Boscolo, J. Wyss, A. Quaranta, *Effects of proton irradiation on glass filter substrates for the Rosetta mission*, *Applied Optics* 42(19), 3970-3980, (2003).
- [5] I. Di Sarcina, M.L. Grilli, F. Menchini, A. Piegari, S. Scaglione, A. Sytchkova, D. Zola, *Behavior of optical thin-film materials and coatings under proton and gamma irradiation*, *Applied Optics* 53(4), A314-A320 (2014).
- [6] M. Sznajder, U. Geppert, M. Dudek, *Degradation of metallic surfaces under space conditions, with particular emphasis on Hydrogen recombination processes*, *Advances in space research* 56(1), 71-84 (2015).
- [7] A.D. Rousseau, D.L. Windt, B. Winter, L. Harra, H. Lamoureux, F. Eriksson, *Stability of EUV multilayers to long-term heating, and to energetic protons and neutrons, for extreme solar missions*, *Proc. SPIE* 5900, 590004 (2005).
- [8] A.I. Gusarov, D. Doyle, A. Hermanne, F. Berghmans, M. Fruit, G. Ulbrich, M. Blondel, *Refractive-index changes caused by proton radiation in silicate optical glasses*, *Applied Optics* 41(4), 678-684, (2002).
- [9] M. Fernández-Rodríguez, C.G. Alvarado, A. Núñez, and A. Álvarez-Herrero, *Analysis of optical properties behavior of cleaceram, fused silica and CaF₂ glasses exposed to simulated space conditions*, *Proceeding of ICSO - International Conference on Space Optics*, Rhodes Island (2010).
- [10] David M. Pozar, *Microwave Engineering*, fourth edition, John Wiley & Sons, (2011)

- [11] H. Angus MacLeod, *Thin-Film Optical Filters (Series in optics and optoelectronics)*, fourth edition, 978-1-4200-7302-7, CRC Press, Taylor & Francis Group, (2010)
- [12] M.G. Pelizzo, A.J. Corso, E. Tessarolo, R. Boettger, R. Hübner, E. Napolitani, M. Bazzan, M. Rancan, L. Armelao, W. Jark and D. Eichert, *Morphological and Functional Modifications of Optical Thin Films for Space Applications Irradiated with Low-Energy Helium Ions*, ACS applied materials & interfaces, (2018).
- [13] A.S. Kuznetsov, M.A. Gleeson, F. Bijkerk, *Ion effects in hydrogen-induced blistering of Mo/Si multilayers*, Journal of Applied Physics, 114(11), 113507 (2013).
- [14] S. Kajita, W. Sakaguchi, N. Ohno, N. Yoshida, T. Saeki, *Formation process of tungsten nanostructure by the exposure to helium plasma under fusion relevant plasma conditions*, Nuclear Fusion 49, 9, (2009).
- [15] I. Tanyeli, L. Marot, D. Mathys, M.C.M. van de Sanden, G. De Temmerman, *Surface Modifications Induced by High Fluxes of Low Energy Helium Ions*, Scientific Reports 5, 9779 (2015).
- [16] J.F. Ziegler, J.P. Biersack, *SRIM - The Stopping and Range of Ions in Solids* (New York Pergamon Press., 1985).
- [17] Di Sarcina, I.; Grilli, M.L.; Menchini, F.; Piegari, A.; Scaglione, S.; Sytchkova, A.; Zola, D.; *Behavior of Optical Thin-Film Materials and Coatings under Proton and Gamma Irradiation*. Appl. Opt. 2014, 53(4), A314-A320.
- [18] Pelizzo, M.; Corso, A.J.; Zuppella, P.; Windt, D.L.; Mattei, G.; Nicolosi P., *Stability of Extreme Ultraviolet Multilayer Coatings to Low Energy Proton Bombardment*. Opt. Express 2011, 19, 14838-14844.
- [19] Nardello, M.; Zuppella, P.; Polito, V.; Corso, A.J.; Zuccon, S.; Pelizzo, M.G., *Stability of EUV Multilayer Coatings to Low Energy Alpha Particles Bombardment*. Opt. Express 2013, 21(23), 28334-28343.
- [20] Niklasson, G.A.; Granqvist, C.G.; Hunderi, O. *Effective Medium Models for the Optical Properties of Inhomogeneous Materials*. Appl. Opt. 1981, 20(1), 26-30.
- [21] Agilent, <https://www.agilent.com>